DESIGN OF AN EXPERIMENTAL FACILITY FOR BUILDING AIRFLOW AND HEAT TRANSFER MEASUREMENTS

By

MOHAMMAD AHMAD ELYYAN

Bachelor of Science in Mechanical Engineering

Jordan University of Science and Technology

Irbid, Jordan

2001

Submitted to the Faculty of the
Graduate College of the
Oklahoma State University
in partial fulfillment of
the requirements for
the Degree of
MASTER OF SCIENCE
May, 2005

DESIGN OF AN EXPERIMENTAL FACILITY

FOR BUILDING AIRFLOW AND HEAT

TRANSFER MEASUREMENTS

Thesis Approved:

Dr. Daniel Fisher

Thesis Advisor

Dr. David Lilley

Dr. Frank Chambers

Dr. A. Gordon Emslie

Dean of the Graduate College

Acknowledgements

First of all I thank God for His blessings and help that He bestowed on me throughout my entire life.

I would like also to thank my advisor, Dr. Dan Fisher, for his corporation and help throughout my graduate study. His encouragement and optimistic attitude were very helpful through this project. I would like also to express my deep appreciation to my advising committee members, Dr. Chambers and Dr. Lilley, whom I worked for as a TA for 3 semesters.

I would like also to thank my fellow research colleagues at the BETSRG for their help, ideas, and the nice times we spent together. I would like to give special thanks to Muhammad Haider Khan, who has been and still a great friend, his advises and encouragements were very helpful. Ben Alexander, who has the greatest manufacturing capabilities. Joseph Pruitt, Calvin Iu, Weixiu Kong, Bereket Nigusse, and Xiaowei Xu all their help is appreciated

I would like to say a special ‘ thank you’ to my mother and my late father, whose life was not long enough to see this day. Their love, encouragement, and understanding is what kept me going during this research after the blessings of God. I would like also to thank the people of the ISS (Islamic society of Stillwater) for their real friendship and caring, I would like to specially thank Saleh Ashagathrah, and Abdulaziz Bagabas.

Table of Contents

List of Tables

List of Figures

Nomenclature

a	Mean absorption coefficient, m^{-1}.
A_i	Area of wall i.
A_L	Aspect ratio (H/L).
A_W	Aspect ratio (H/W).
C_p	Specific Heat, kJ/kg.K.
e_i	Uncertainty of quantity i.
$f^{\#}$	Lens f-number.
g	Gravitational acceleration, m/s^2.
Gr	Grashof number ($g\beta\Delta TH^3/\nu^2$).
H	heat convection coefficient, $W/m^2.K$.
L, H, W	Enclosure dimensions, m.
M	Lens magnification.
Nu	Nusselt number (h L/k).
P	Pressure, Pa.
P*	Dimensionless pressure ($P/\rho V_{in}^2$).
Pr	Prandtl number (ν/α).
Ra	Rayleigh number ($g\beta\Delta TH^3/\nu\ \alpha$ = Gr.Pr).
T	Temperature, ^oC, K.
T_H, T_C	Hot and cold walls temperature, ^oC, K.

T_m	Mean air temperature ($0.5(T_H + T_C)$).
T_{out}, T_{in}	Outlet and Inlet temperature to cold wall, ^oC, K.
T_{ref}	Reference Temperature, ^oC, K.
u, v	Coordinate velocity components, m/s.
x, y, z	Coordinates, m.
α	Thermal Diffusivity, m^2/s.
β	Thermal Expansion $(-\frac{1}{\rho}\frac{\partial \rho}{\partial T})$, K^{-1}.
ε	Surface emissivity.
μ	Dynamic Viscosity, Pa.s.
ν	Kinematic Viscosity, m^2/s.
θ^*	Dimensionless temperature $((T-T_C)/(T_H-T_C))$.
ρ	Density, kg/m^3.
σ	Stefan-Boltzman constant, 5.67×10^{-8} $W/m^2.K^4$.

1. Introduction

Natural convection is a phenomenon that is relevant to many applications in our everyday life. It can be seen in passive heating of enclosures; it also plays an important role in cooling electronic chips. Researchers have studied this phenomenon extensively in the last decades due to its importance. Several methods are used to analyze natural convection in building enclosures. The first approach is to run the experiments under realistic conditions. This means building a full scale experiment and running the tests under realistic conditions to obtain results. This method duplicates the application's conditions, and thus its results are accurate and reliable. Unfortunately this approach is not always practical, especially if we want to study the flow field in large enclosures, such as theaters and atriums. Moreover, this approach is often not cost effective; the cost of equipment, controls and effort is all related to the size of the enclosure.

The second approach, to natural convection studies, is modeling the enclosure numerically. Many natural convection studies using this method are reported in the literature. Numerical modeling is much easier than the experimental methods. It is less expensive, facilitates obtaining the required data at any point in the domain, and allows the application of any boundary condition. Nevertheless, despite their attractiveness, computational methods are still limited to simple geometries, and as the geometry complexity increases, the modeling accuracy decreases and the computational cost increases. Also note limitations in predicting surface heat transfer due to the limitations in solving transport equations in the confined buoyancy driven flow.

The last method is an experimental approach using a scale model of the enclosure. This method, which has been in use for some time now, is practical, less expensive than building a full-scale experiment, and if scaled with care provides accurate results. Scale model enclosure experiments require careful scaling of geometry, operating and boundary conditions, and the working fluid. Correct scaling of any phenomenon requires matching the scaling parameters that phenomenon. The scaling parameters are obtained by conducting careful dimensional analysis of the governing equations of that phenomenon.

The heat transfer side of natural convection within enclosures has been deeply studied and analyzed. While, the flow field accompanying natural convection lacks such a deep quantitative study. The flow field was studied mainly using flow visualizaiton Most of the flow visualization techniques used to study the flow were done using smoke or dye, depending on the working fluid. The flow velocity was obtained using elementary techniques, i.e. video recording and regular photographing. The uncertainty associated with such measurements is high and the results are not really reliable. This high uncertainty drives the search for a new velocity measurement technique that gives an accurate measurement of the flow field velocity inside the enclosure.

Particle Image Velocimetry (PIV) is a relatively new technique that gives accurate measurement of fluid flow velocity. It has not been used for natural convection measurements, to the best knowledge of this author. This use of this technique for natural convection flow velocity measurement will be explored in this project.

Since the scaling method appears to be a good method for studying natural convection, a scaled model will be constructed to study natural convection in enclosures.

A detailed scaling analysis will be conducted for natural convection, and recommendations will be given for a suitable scaling fluid. In this project, air will be used as the working medium to show the capability of the PIV technique in flow visualization,

In this study, an extensive literature review of previous experimental work on scaling of natural convection will be provided, followed by a review of the numerical work in this field. Then a detailed scale analysis of the governing equations of natural convection will be presented, followed by a discussion of the scaling fluid and the parameters controlling its selection. The next chapter will present the experimental facility design, construction, instrumentation and uncertainty analysis. Heat transfer experimental results of natural convection within the experimental facility with air as the working fluid. Flow visualization of the flow field inside the enclosure using smoke and PIV will be conducted and the results will be presented. Detailed discussion of the PIV technique and its results will be also given. Finally, concluding remarks and recommendation for future work will be given.

2. Literature Review

Natural convection within enclosures is an important topic due to its application in many areas. Most of the experimental work related to natural convection within enclosures was conducted on scale models of enclosures; the main outputs of the research were the flow field and the heat transfer parameters of the enclosure. On the other hand, many researchers tried to solve the natural convection problem numerically. The numerical approach dealt with different natural convection surface configurations and with different enclosure scales ranging from small scale such as computer chips to large scale such as office size. The following paragraphs review pervious experimental and numerical studies on natural convection.

2.1 Natural Convection Experiments

The literature is rich with work done in the field of natural convection. One of the relevant works done on natural convection was by Weber (1980), where he constructed a scale model of a partitioned one room enclosure, with an opening in the partition. He used R12 as the scaling fluid, and configured his experiments with differentially heated walls on the opposite sides of the opening. Although no visualization was conducted, temperature measurement was reported. Weber (1980) was the first one, to the best knowledge of this author, to use a high density gas (R12) as the scaling fluid, in which he showed that refrigerants scale natural convection better than other fluids. In addition he reported that R114 would scale natural convection in enclosures better than R12.

Bejan et al. (1981) conducted natural convection experiments using water as the working fluid with Rayleigh number, $2x10^8 > Ra < 2x10^9$, in an enclosure with aspect ratio (H/L) of 0.0625. Temperature measurements and flow visualization were reported. They reported that the core flow structure is dominated by the presence of horizontal intrusion layers (jets) flowing along the two insulated walls. They also reported that the inner region bounded by the two jets is occupied by practically stagnant fluid. They found the fluid temperature in the inner region to vary linearly with depth and independent of longitudinal position. The presence of two secondary cells was reported and explained to be the result of the interaction of the two horizontal jets with stagnant inner fluid. Bejan et al. (1981) did not identify their flow to be turbulent or laminar, but the high Rayleigh number they reported suggests that their flow was turbulent.

Ferm (1985) built an office size rectangular room, Height (H) = 3 m, $A_L = H/L = 0.3$, $A_W = H/W = 0.6$. The working fluid in this full-scale room was air, and the Rayleigh number was of order $\sim 10^{10}$. Ferm (1985) conducted flow visualization tests in the room, and her results showed the existence of turbulent boundary layers along the vertical walls with horizontal flow near the ceiling and the floor. She also reported the existence of two secondary flow loops along the ceiling and the floor, as shown in figure 1.1. In the ceiling secondary loop, some of the flow reversed direction and flowed back to the hot wall directly beneath the top layer. The floor secondary loop was symmetric to the ceiling loop. The flow in the core was stratified with a temperature variation that was approximately linear from ceiling to floor. A large temperature variation occurred only inside the boundary layers, and was constant from the hot wall to the cold wall once outside the vertical boundary layers.

Olson (1986) scaled Ferm's (1985) experiment using high-density gas, R114, in a 1/5 scale model of Ferm's (1985) room. Olson (1986) used operating conditions similar to those used by Ferm (1985) and was able to achieve a Rayleigh number of order 10^{10}. Olson's (1986) experiments matched both the geometrical aspects and the operating conditions of the full-scale experiments by Ferm (1985). Olson (1986) conducted flow visualization for the flow field inside the enclosure using smoke, in addition to the regular temperature measurements. Olson results showed close agreement with Ferm's (1985) full-scale results for both temperature and velocity profiles and Nusselt numbers (within the uncertainty limits). Also, the flow visualization showed the existence of turbulent boundary layers along the vertical walls, and the existence of the secondary flow loops along the ceiling and the floor. Olson (1986) justified the use of R114 due to the fact that R114 models the radiation transfer in the enclosure better than water, which is opaque. Olson reports that perfect match of the scaling parameters was not obtained, but it was better than water scaling. Figure 1.1 shows the flow field viewed by Olson and Ferm (Olson et al., 1990).

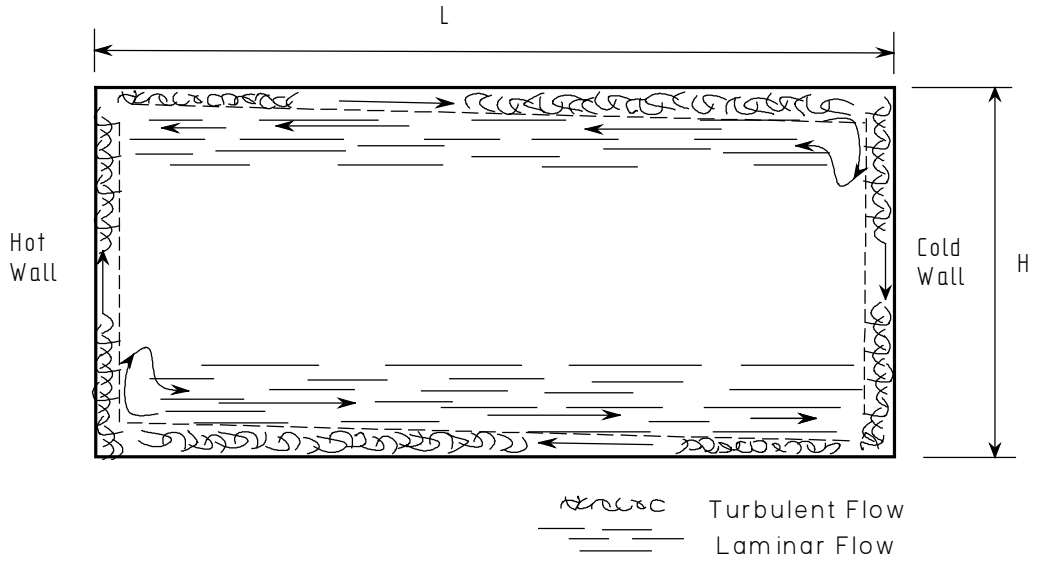

Figure 1.1: Flow Pattern in the empty enclosure for small-scale model and the full-scale room, (Olson et al., 1990)

Cheeswright and Zial (1986) studied the temperature distributions and local heat transfer rate in a large vertical rectangular cavity. Their air filled cavity had no internal obstructions and had a variable horizontal aspect ratio (W/L) of 2 to 1 and a vertical aspect ration (H/L) of 6 to 1. The Grashof number (Gr) was of the order 10^{10}. The temperature distribution across the enclosure and heat transfer convection coefficient correlation was reported. They reported the existence of a core region with a uniform vertical temperature gradient.

Bohn and Anderson (1986) studied natural convection in a three dimensional configuration. Their cubic enclosure with interior dimensions of 30.5 cm was filled with water. Their Rayleigh number was ~ 10^{10}. They tested two different configurations; the first was one heated wall and three cooled walls. The second was two contiguous heated walls and two contiguous cooled walls. In both cases the top and the bottom were adiabatic. They found that even for the three dimensional configurations the core exhibited stratification similar to the two dimensional case. No flow visualization was conducted.

Khalifa and Marshal (1990) conducted steady state natural convection experiments in an empty full scale enclosure filled with air. They tested nine different heating configurations in buildings. The test cell was a room sized enclosure with an aspect ratio (H/W) of 0.7. A total of 36 heat transfer coefficient correlations were reported for the different configurations. The heat transfer coefficient correlations reported were based on the temperature difference between the wall and the air next to the wall. No flow

visualization or temperature distribution within the enclosure measurements was reported.

Hsieh and Wang (1994) studied three dimensional natural convection within enclosures for different working fluids; air, water and silicon oil ($0.7 \leq Pr \leq 464$). The aspect ratio (H/L) of the enclosure ranged from 1 to 20, while Rayleigh number ranged from 8.7×10^2 to 2.0×10^9. They visualized the flow structure using photographic records of the motion of tracer particles (aluminum powder, 5-15 μm) illuminated by a white light sheet for the silicon oil case. For high Ra and an aspect ratio of 10, they reported the existence of a multi cellular motion in the center, surrounded by helical streamlines by which the fluid is transported from the core to the adjacent walls. When the flow reaches the top or bottom wall the main flow becomes two-dimensional. The flow field reported by the authors is shown in figure 1.2. The authors also observed transition to turbulent flow for higher Rayleigh numbers ($Ra > 1.4 \times 10^7$). In addition they noticed that three dimensional effects were significant at higher Rayleigh numbers and aspect ratios (≥ 5). Hsieh and Wang (1994) concluded that aspect ratio effects on heat transfer were not clearly indicated for their cases.

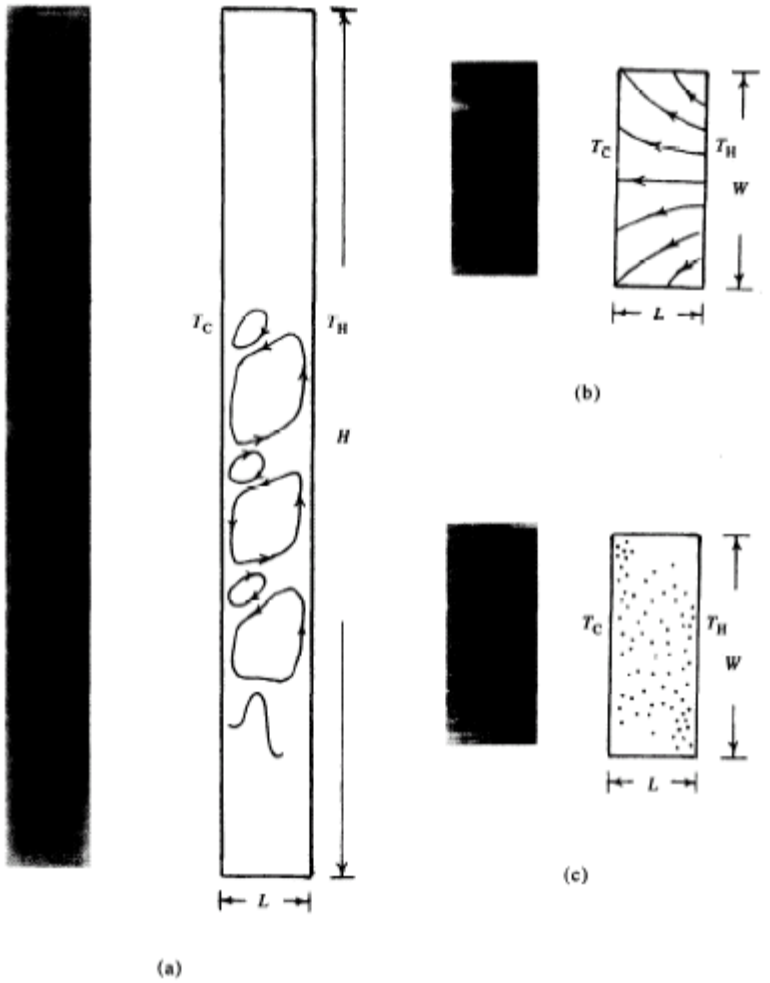

Figure 1.2: 4. Flow visualization (Pr = 464) for A = 10. Ra = 1.2 x l0^9 at different planes.

(a) .XY plane, z = W/2. (b) xz plane, y = H. (c) xz plane, y = H/2. (Hsieh et al., 1994)

Awbi and Hutton (1999) conducted natural convection experiments with air in a room sized enclosure with a 0.8 aspect ratio (H/L). Various Heating configurations were used with different temperature differences. They reported convective heat transfer coefficients for different heating scenarios and compared them to those available in the literature. No flow visualization or enclosure temperature distribution was reported.

Ampofo and Karayiannis (2003) conducted a benchmark turbulent natural convection experiment with an air filled square cavity. The cavity was 0.75 m x 0.75 x

1.5 m deep, which resulted in 2D flow. They conducted detailed measurements of local air temperature using micro thermocouples and measured local velocities using LDA. Mean and fluctuation quantities of temperature and velocity were presented. The local and average Nusselt numbers, and the wall shear stress as well as the turbulent kinetic energy and the dissipation rate of the temperature variance are also presented. The flow field was 2D and turbulent with a thin viscous boundary layer and stationary core. From comparison with CFD results, Ampofo et al. (2003) concluded that the LES and k-ε turbulence models can predict the mean quantities reasonably well, but cannot predict the fluctuation and turbulence quantities.

In summary, most of the scaling experiments for natural convection used water as the scaling fluid. This scaling did not match the full scale results, especially the secondary flow near the top and bottom of the enclosure reported by Ferm (1985). Better results were achieved when high density gases were used as the scaling fluid. As stated earlier, the suitability of the scaling depends on its ability to match the full size experimental parameters. Although using water in the scaled experiments matched the Rayleigh number in the full scale experiments, using water sacrificed Prandtl number and radiation matching, since water is opaque to walls radiation. This mismatch resulted in different velocity and temperature patterns from the full scale ones, as reported by Olson (1986). This triggered the search for new scaling fluids. Interest was driven toward high-density gases, i.e. refrigerants, which proved to be a suitable scaling fluid as demonstrated by Weber (1980) and Olson (1986). Nevertheless, perfect match of the scaling parameters of air was not reported, even with a refrigerant as the scaling fluid.

Table 1.1 shows a list of the literature review conducted here. From the previous literature review we saw that the velocity measurements conducted were crude ones with high uncertainty, except for Ampofo and Karayiannis (2003). This shows the need for a new technique for accurate velocity measurement.

Table 1.1: Summary of Natural Convection Previous Research

Investigator	Working Fluid	Flow Regime	Flow Visualization	Size
Weber et al. (1980)	R12 and Air	X	X	Small & Large
Bejan et al. (1981)	Water	Turbulent	Smoke	Small
Ferm (1985)	Air	Turbulent	Smoke	Large
Olson (1986)	R114	Turbulent	Smoke	Small
Bohn et al. (1986)	Water	X	X	Small
Cheesewright et al.(1986)	Air	Turbulent	X	Small
Khalifa et al. (1990)	Air	X	X	Large.
Hsieh et al. (1994)	Air, Water and Silicon Oil	Laminar – Turbulent	For Silicon Oil	Small
Awbi et al. (1999)	Air	X	X	Large
Ampofo et al. (2003)	Air	Turbulent	LDA	

2.2 Numerical Analysis of Natural Convection

Natural convection within enclosure has been studied extensively for different types of geometries using numerical methods. Numeral investigations fall into two main categories: those that consider the radiation interaction with the flow and those that do not.

2.2.1 No Radiation Model Included

Said et al. (1996) presented a numerical simulation for buoyancy driven flow in an inclined two-dimensional rectangular enclosure with partitions. The upper and lower

walls were insulated, and hot and cold sidewalls were isothermal. They assumed the flow to be steady, 2D, with negligible viscous dissipation. The low Reynolds number extension of the two equation k-ε turbulence model was used, with Pr of 0.71 and aspect ratio=1. Laminar and turbulent cases were studied at different inclination angles. The average Nusselt number was reduced by the insertion of partitions. An optimum angle was found for highest average Nusselt number. For the laminar case, Ra = 10^6, their results showed a zero temperature gradient along the x-direction in the core and higher gradients along the wall. Also they reported that the thickness of the thermal boundary layer grows with height along the hot wall and decreases along the cold wall. The second set of their results was for high Rayleigh numbers (>10^9), which resulted in turbulent flow. This turbulence was within a thin boundary layer along the hot and cold walls of the enclosure. The temperature and velocity gradients within this boundary layer were very large. They compared their results to other published numerical and experimental results. Said et al. attributed the differences with the experimental results to the conduction losses from the experiment.

Dol and Hanjalic (2000) did a computational study of turbulent convection in a side heated near cubic enclosure at high Rayleigh number (4.9×10^{10}). Their main concern was to characterize the flow in the corners of the enclosure and to find the best turbulence model for the flow field. They used two different boundary conditions for the ceiling and floor: adiabatic and isothermal. The vertical walls were adiabatic. Also, two turbulence models were tested: the low Reynolds number differential second moment stess/flux closure (SMC) model and the low Reynolds number k-ε model (KEM). A fully implicit first order transient integration was used to obtain the solution; the SIMPLE method was

used to solve the system of the equations. For the 2D case with the adiabatic ceiling and floor, after comparison with the Direct Numerical Simulation (DNS) and experimental published results, the authors showed that the SMC has better ability to capture the flow details, especially at the corners, than the KEM, while for the isothermal ceiling and floor walls the SMC and KEM gave almost the same results.

2.2.2 Radiation Model Included

Velusamy et al. (2001) studied the influence of surface to surface radiation on turbulent natural convection with a transparent medium in differentially heated square and tall vertical enclosures. They analyzed the effect of emissivity, mean temperature and temperature difference on the convective and radiative Nusselt numbers. The convective Nusselt number is defined as $Nu = qW/(K\Delta T)$, where $q = -K(\partial T/\partial n)_{wall}$. The radiative Nusselt number is defined using $q = -[\varepsilon/(1-\varepsilon)](\sigma T_w^4 - B)$ for a radiative flux; where ε is the hemispherical emissivity of the wall, B is the radiosity, σ is the Stephan Boltzman constant, and K is the thermal conductivity of the fluid. They simulated a 2D vertical rectangular enclosure with differentially heated sidewalls and adiabatic ceiling and floor. Their Rayleigh number ranged from 10^9 to 10^{12}; wall emissivity ranged from 0-0.9. The temperature difference ranged from 10-250 K and the aspect ratio from 1 to 200. Air was used as a transparent working fluid. The standard k-ε model was used for turbulent flow modeling with the Boussinesq approximation for buoyancy. The SIMPLE algorithm with a staggered grid was used to solve the governing equations. Velusamy et al. (2001) included the surface radiation in the generalized energy balance equation. Their study showed that the radiation interaction caused the magnitude of the circulation velocity to

increase which enhanced convection, and that there was unstable stratification close to the top and bottom walls. Also, they reported that the radiative heat transfer contribution was significant even at low temperatures. In addition, they reported that the temperature difference between the hot and cold walls should be treated as an independent parameter, for flow with radiation interaction. The radiation interaction is the effect of radiation on the flow velocity, which in turn changed the wall Nusselt number.

Kim, K. S. (1996) conducted a numerical analysis of turbulent natural convection coupled with radiation in a partially open enclosure. Kim (1996) studied a 2D partially opened enclosure with two isothermal vertical walls, and insulated floor and ceiling, with the opening in the cold wall. The wall opening allowed fluid flow and heat transfer. Kim (1996) used the standard k-ε model to simulate the turbulent flow, with the Boussinesq approximation for the buoyancy term. The working fluid within the enclosure was assumed to be a gray medium that absorbed, emitted and isotropically scattered the internal thermal radiation. All the walls were considered black and opaque to thermal radiation. The enclosure was covered with a non-uniform grid (40x60). The Rayleigh number ranged from $10^8 \sim 10^{10}$, with fluid Prandtl number = 0.71. Kim (1996) results show that thermal radiation increased flow velocity and affected the average Nusselt number.

From the above review of the numerical work done on natural convection we find that most of the researchers reported transition to turbulence at Rayleigh number of 10^7-10^8, in addition they have used low Reynolds number k-ε models to simulate turbulence, in order to account for the flow boundary layer. Finally, they concluded that the radiation heat transfer from the wall has an important effect on Nusselt number, and on the flow

field inside the enclosure. Thus, we can see the importance of considering fluid radiation properties in scaling experiments design. So this further proves the mismatch caused by using water for scaling natural convection within enclosures.

3. Scale Analysis

3.1: Scale Analysis:

In this section the dimensional analysis of the governing equations for natural convection will be presented. The objective is to identify the dimensionless scaling parameters required to design a scale model of a full sized experimental facility. Since the facility will be used for a range of experiment dimensional analysis of both natural and forced convection regimes will be discussed.

A brief description of the full-scale enclosure under consideration is necessary before starting the dimensional analysis, the facility under consideration consists of two enclosures one on top of the other with a stairwell connecting the rooms, as shown in figure 3.1. Both levels of the test chamber have suspended ceilings and raised floors. Each room is 8'4" from finished floor to suspended ceiling.

Since the building upper and lower zones are identical, the dimensional analysis will be applied to a single zone. Successfully matching the dimensionless parameters for single zone flow will give similarly valid results for the whole building.

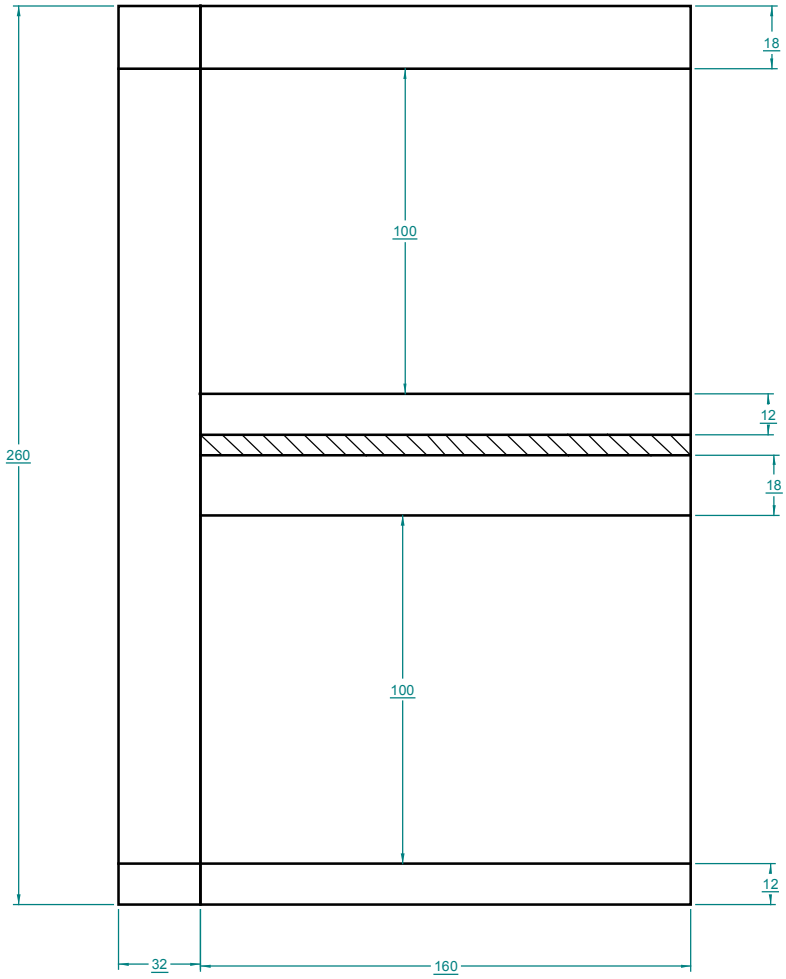

Figure 3.1: Schematic Drawing of the Full-Scale Enclosure

Figure 3.2 shows a two-dimensional schematic of a single zone. The zone under consideration has length L, height H, and depth W. It is differentially heated using isothermal end walls T_H and T_C. The ceiling and the floor along with the sidewalls are well insulated. For the forced convection case, air enters the zone from a diffuser at the ceiling with a velocity V_{in}.

The scale analysis will be done for the x and z directions and the y direction will not be considered in this analysis. This assumption seems reasonable when looking at the ideal boundary conditions considered here; isothermal vertical sidewalls and adiabatic floor and ceiling and front and back walls. Furthermore, the experimental results reported in the literature supports the two dimensional assumption used here, Olson (1986).

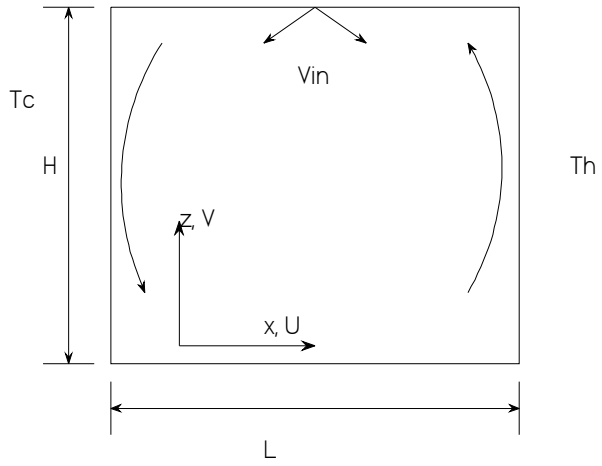

Figure 3.2: Schematic Diagram of Single Zone Geometry

3.1.1: Natural Convection:

The dimensional analysis closely follows Bejan (1984) and Olson (1986). The analysis assumes steady state natural convection with an incompressible, constant viscosity fluid. The governing equations are the mass, momentum and energy conservation equations.

Continuity:

$$\frac{\partial v}{\partial z} + \frac{\partial u}{\partial x} = 0 \tag{3.1}$$

Z - Momentum:

$$\rho\left(v\frac{\partial v}{\partial z}+u\frac{\partial v}{\partial x}\right)=-\frac{\partial P}{\partial z}+\mu\left(\frac{\partial^2 v}{\partial z^2}+\frac{\partial^2 v}{\partial x^2}\right)-\rho g \tag{3.2}$$

X – Momentum:

$$\rho\left(v\frac{\partial u}{\partial z}+u\frac{\partial u}{\partial x}\right)=-\frac{\partial P}{\partial x}+\mu\left(\frac{\partial^2 u}{\partial z^2}+\frac{\partial^2 u}{\partial x^2}\right) \tag{3.3}$$

Energy:

$$v\frac{\partial T}{\partial z}+u\frac{\partial T}{\partial x}=\alpha\left(\frac{\partial^2 T}{\partial z^2}+\frac{\partial^2 T}{\partial x^2}\right) \tag{3.4}$$

Consider the Z- momentum equation and apply Boussinesq approximation;

$$\rho=\rho_\infty\left[1-\beta(T-T_{ref})\right] \tag{3.5}$$

where, $\beta=-\frac{1}{\rho}\left[\frac{\partial\rho}{\partial T}\right]_p$

Then the Z – momentum equation will look like;

$$\rho\left(v\frac{\partial v}{\partial z}+u\frac{\partial v}{\partial x}\right)=-\frac{\partial P}{\partial z}+\mu\left(\frac{\partial^2 v}{\partial z^2}+\frac{\partial^2 v}{\partial x^2}\right)-\rho_\infty\left[1-\beta(T-T_{ref})\right] \tag{3.6}$$

In order to eliminate the pressure term from the momentum equations, cross differentiate the X and Z equations and subtract;

$$\frac{\partial}{\partial x}\left[v\frac{\partial v}{\partial z}+u\frac{\partial v}{\partial x}\right]-\frac{\partial}{\partial z}\left[v\frac{\partial u}{\partial z}+u\frac{\partial u}{\partial x}\right]= \upsilon\left[\frac{\partial}{\partial x}\left(\frac{\partial^2 v}{\partial z^2}+\frac{\partial^2 v}{\partial x^2}\right)+\frac{\partial}{\partial z}\left(\frac{\partial^2 u}{\partial z^2}+\frac{\partial^2 u}{\partial x^2}\right)\right]+g\beta\frac{\partial T}{\partial x} \tag{3.7}$$

Dimensionless variables will make it possible to non dimensionalize the geometry equations and compare the results of the model to the full-scale experiment. Since we are

interested in the average characteristics of the flow field and heat transfer, e.g. average Nusselt and Rayleigh numbers, in the enclosure, the dimensionless variables will be related to the enclosure's geometry, on the contrary with what is usually used of using the boundary layer terms when dimensionalizing the different parameters. Following is a list of the dimensionless variables that will be introduced:

For location:

$$X^* = X / L, \quad Z^* = Z / H \tag{3.8}$$

For temperature and velocity:

$$\theta^* = (T - T_C) / (T_H - T_C) \tag{3.9}$$

$$U^* = U / V_C, \qquad V^* = V / V_C \tag{3.10}$$

where V_C is the buoyancy driven air velocity

In buoyancy driven flow, there is no superimposed freestream velocity U_∞ . Thus the flow velocities must be scaled with the body force. Considering the region where the velocity reaches maximum, and ignoring the effects of diffusion and cross stream convection in this region, also assuming that T can be approximated by T_w; the adjacent wall temperature. The Z momentum equation reduces to

$$v\frac{\partial v}{\partial z} = g\beta(T - T_{ref})$$

but the driving force of the buoyant flow is the temperature difference between the isothermal walls. Scaling the above equation we find,

$$v^2 \sim g\beta(T_H - T_C)H$$

from there the characteristic buoyancy velocity can be estimated as,

$$V_C = \left[\frac{g\beta}{2}(T_H - T_C)H\right]^{0.5} \tag{3.11}$$

The ½ factor is introduced so that the characteristic velocity is the same as that of an isolated vertical wall exposed to a temperature difference of $(T_H - T_C)/2$, Olson (1986).

Applying those scaling parameters to the governing equations we get;

Continuity:

$$\frac{V_c}{H}\frac{\partial V^*}{\partial Z^*} + \frac{V_c}{L}\frac{\partial U^*}{\partial X^*} = 0 \Rightarrow \frac{\partial V^*}{\partial Z^*} + \frac{H}{L}\frac{\partial U^*}{\partial X^*} = 0 \tag{3.12}$$

Applying an order of magnitude analysis to the continuity equation we find;

$$\frac{V_c}{H} \sim \frac{V_c}{L} \tag{3.13}$$

Substituting the above scaling parameters into equation 3.7 above,

$$\frac{1}{L}\frac{\partial}{\partial X^*}\left[\frac{V_c^2}{H}V^*\frac{\partial V^*}{\partial Z^*} + \frac{V_c^2}{L}V^*\frac{\partial U^*}{\partial X^*}\right] - \frac{1}{H}\frac{\partial}{\partial Z^*}\left[\frac{V_c^2}{H}V^*\frac{\partial U^*}{\partial Z^*} + \frac{V_c^2}{L}U^*\frac{\partial U^*}{\partial X^*}\right] =$$
$$\left[\frac{1}{L}\frac{\partial}{\partial X^*}\left(\frac{V_c}{H^2}\frac{\partial^2 V^*}{\partial Z^{*2}} + \frac{V_c}{L^2}\frac{\partial^2 V^*}{\partial X^{*2}}\right) - \frac{1}{H}\frac{\partial}{\partial Z^*}\left(\frac{V_c}{H^2}\frac{\partial^2 U^*}{\partial Z^{*2}} + \frac{V_c}{L^2}\frac{\partial^2 U^*}{\partial X^{*2}}\right)\right] - \frac{g\beta(T_H - T_C)}{L}\frac{\partial \theta^*}{\partial X^*}$$

$$\Rightarrow \frac{V_c^2}{LH}\frac{\partial}{\partial X^*}\left[V^*\frac{\partial V^*}{\partial Z^*} + \frac{H}{L}V^*\frac{\partial U^*}{\partial X^*}\right] - \frac{V_c^2}{HL}\frac{\partial}{\partial Z^*}\left[\frac{L}{H}V^*\frac{\partial U^*}{\partial Z^*} + U^*\frac{\partial U^*}{\partial X^*}\right] =$$
$$\upsilon\left[\frac{1}{L}\frac{V_c}{H^2}\frac{\partial}{\partial X^*}\left(\frac{\partial^2 V^*}{\partial Z^{*2}} + \left(\frac{H}{L}\right)^2\frac{\partial^2 V^*}{\partial X^{*2}}\right) - \frac{1}{L}\frac{V_c}{H^2}\frac{\partial}{\partial Z^*}\left(\frac{L}{H}\frac{\partial^2 U^*}{\partial Z^{*2}} + \frac{H}{L}\frac{\partial^2 U^*}{\partial X^{*2}}\right)\right.$$
$$\left. - \frac{g\beta(T_H - T_C)}{L}\frac{\partial \theta^*}{\partial X^*}\right. \tag{3.14}$$

$$\text{but } V_c = \left[0.5g\beta(T_H - T_C)H\right]^{0.5} \Rightarrow \frac{V_C^2}{H} = g\beta(T_H - T_C)/2$$

Considering the order of magnitude only, we find;

$$\frac{V_C^2}{H} \sim g\beta(T_H - T_C),\ V_C \sim \left[g\beta(T_H - T_C)H\right]^{0.5}$$

By substitution, equation 3.14 becomes:

$$\frac{\partial}{\partial X^*}\left[V^*\frac{\partial V^*}{\partial Z^*} + \frac{H}{L}U^*\frac{\partial U^*}{\partial X^*}\right] - \frac{\partial}{\partial Z^*}\left[\frac{L}{H}V^*\frac{\partial U^*}{\partial Z^*} + U^*\frac{\partial U^*}{\partial X^*}\right] =$$
$$\frac{\upsilon\left[g\beta(T_H - T_C)H/2\right]^{0.5}}{g\beta(T_H - T_C)H^2/2}\left[\frac{\partial}{\partial X^*}\left(\frac{\partial^2 V^*}{\partial Z^{*2}} + \left(\frac{H}{L}\right)^2\frac{\partial^2 V^*}{\partial X^{*2}}\right) - \frac{\partial}{\partial Z^*}\left(\frac{L}{H}\frac{\partial^2 U^*}{\partial Z^{*2}} + \frac{H}{L}\frac{\partial^2 U^*}{\partial X^{*2}}\right)\right] - \frac{\partial\theta^*}{\partial X^*}$$

$$\Rightarrow \frac{\partial}{\partial X^*}\left[V^*\frac{\partial V^*}{\partial Z^*} + \frac{H}{L}U^*\frac{\partial U^*}{\partial X^*}\right] - \frac{\partial}{\partial Z^*}\left[\frac{L}{H}V^*\frac{\partial U^*}{\partial Z^*} + U^*\frac{\partial U^*}{\partial X^*}\right] =$$
$$\left(\frac{2\upsilon^2}{g\beta(T_H - T_C)H^3}\right)^{0.5}\left[\frac{\partial}{\partial X^*}\left(\frac{\partial^2 V^*}{\partial Z^{*2}} + \left(\frac{H}{L}\right)^2\frac{\partial^2 V^*}{\partial X^{*2}}\right) - \frac{\partial}{\partial Z^*}\left(\frac{L}{H}\frac{\partial^2 U^*}{\partial Z^{*2}} + \frac{H}{L}\frac{\partial^2 U^*}{\partial X^{*2}}\right)\right] - \frac{\partial\theta^*}{\partial X^*}$$

$$\Rightarrow \frac{\partial}{\partial X^*}\left[V^*\frac{\partial V^*}{\partial Z^*} + \frac{H}{L}U^*\frac{\partial U^*}{\partial X^*}\right] - \frac{\partial}{\partial Z^*}\left[\frac{L}{H}V^*\frac{\partial U^*}{\partial Z^*} + U^*\frac{\partial U^*}{\partial X^*}\right] =$$
$$\left(\frac{2}{Gr}\right)^{0.5}\left[\frac{\partial}{\partial X^*}\left(\frac{\partial^2 V^*}{\partial Z^{*2}} + \left(\frac{H}{L}\right)^2\frac{\partial^2 V^*}{\partial X^{*2}}\right) - \frac{\partial}{\partial Z^*}\left(\frac{L}{H}\frac{\partial^2 U^*}{\partial Z^{*2}} + \frac{H}{L}\frac{\partial^2 U^*}{\partial X^{*2}}\right)\right] - \frac{\partial\theta^*}{\partial X^*} \qquad (3.15)$$

where:

$$\text{Gr: Grashof number} = g\beta(T_H - T_C)H^3/\upsilon^2 \qquad (3.16)$$

For the energy equation;

$$\frac{V_c(T_H - T_C)}{H}V^*\frac{\partial\theta^*}{\partial Z^*} + \frac{V_c(T_H - T_C)}{L}U^*\frac{\partial\theta^*}{\partial X^*} = \alpha\left(\frac{(T_H - T_C)}{H^2}\frac{\partial^2\theta^*}{\partial Z^{*2}} + \frac{(T_H - T_C)}{L^2}\frac{\partial^2\theta^*}{\partial X^{*2}}\right)$$
$$\frac{V_c(T_H - T_C)}{H}\left[V^*\frac{\partial\theta^*}{\partial Z^*} + \frac{H}{L}U^*\frac{\partial\theta^*}{\partial X^*}\right] = \alpha\frac{(T_H - T_C)}{H^2}\left(\frac{\partial^2\theta^*}{\partial Z^{*2}} + \frac{H^2}{L^2}\frac{\partial^2\theta^*}{\partial X^{*2}}\right)$$
$$V^*\frac{\partial\theta^*}{\partial Z^*} + \frac{H}{L}U^*\frac{\partial\theta^*}{\partial X^*} = \alpha\frac{1}{H[g\beta(T_H - T_C)H/2]^{0.5}}\left(\frac{\partial^2\theta^*}{\partial Z^{*2}} + \frac{H^2}{L^2}\frac{\partial^2\theta^*}{\partial X^{*2}}\right)$$

$$\Rightarrow V^* \frac{\partial \theta^*}{\partial Z^*} + \frac{H}{L} U^* \frac{\partial \theta^*}{\partial X^*} = \left(\frac{2}{Gr}\right)^{0.5} \frac{1}{Pr}\left(\frac{\partial^2 \theta^*}{\partial Z^{*2}} + \frac{H^2}{L^2}\frac{\partial^2 \theta^*}{\partial X^{*2}}\right) \tag{3.17}$$

where;

$$Gr = \frac{g\beta(T_H - T_C)H^3}{\upsilon^2} \equiv \text{Grashof number}$$

$$Pr = \frac{\upsilon}{\alpha} \equiv \text{ Prandtl number} \tag{3.18}$$

Also equation 3.17 can be written as,

$$V^* \frac{\partial \theta^*}{\partial Z^*} + \frac{H}{L} U^* \frac{\partial \theta^*}{\partial X^*} = \frac{1}{(Ra_H Pr)^{0.5}}\left(\frac{\partial^2 \theta^*}{\partial Z^{*2}} + \frac{H^2}{L^2}\frac{\partial^2 \theta^*}{\partial X^{*2}}\right) \tag{3.19}$$

where;

$$Ra_H = \frac{g\beta(T_H - T_C)H^3}{\upsilon\alpha} \equiv \text{ Rayleigh number} \tag{3.20}$$

From the previous scale analysis, three dimensionless parameters appear to be important, these are;

$Gr^{0.5}$

$Gr^{0.5}$ Pr or $(Ra_H Pr)^{0.5}$

Aspect ratio; A_L=H/L

3.1.2: Forced Convection:

Scale analysis of forced convection in enclosures is similar to that of natural convection. Using the same scaling parameters introduced in equations 3.9 and 3.10 above and introducing new non dimensional variables for pressure and velocity:

$$P^* = P/\rho V_{in}^2 \tag{3.21}$$

$$U^* = U / V_{in}\ , \qquad V^* = V / V_{in} \tag{3.22}$$

where:

V_{in} = the inlet flow velocity.

Forced convection is governed by the same equations that control natural convection, i.e. equations 3.1, 3.2, 3.3, and 3.4.

Applying the dimensionless variables introduced above, simplifying and collecting the terms we will get;

Continuity:

$$\frac{\partial V^*}{\partial Z^*} + \frac{\partial U^*}{\partial X^*} = 0 \tag{3.23}$$

Z – Momentum:

$$V^* \frac{\partial V^*}{\partial Z^*} + U^* \frac{\partial V^*}{\partial X^*} = -\frac{\partial P^*}{\partial Z^*} + \frac{1}{Re}\left(\frac{\partial^2 V^*}{\partial Z^{*2}} + \frac{\partial^2 V^*}{\partial X^{*2}}\right) - \frac{Gr}{Re^2}\theta^* \tag{3.24}$$

X – Momentum:

$$V^* \frac{\partial U^*}{\partial Z^*} + U^* \frac{\partial U^*}{\partial X^*} = -\frac{\partial P^*}{\partial X^*} + \frac{1}{Re}\left(\frac{\partial^2 V^*}{\partial Z^{*2}} + \frac{\partial^2 V^*}{\partial X^{*2}}\right) \tag{3.25}$$

Energy:

$$V^* \frac{\partial \theta^*}{\partial Z^*} + U^* \frac{\partial \theta^*}{\partial X^*} = \frac{1}{Pe}\left(\frac{\partial^2 \theta^*}{\partial Z^{*2}} + \frac{\partial^2 \theta^*}{\partial X^{*2}}\right) \tag{3.26}$$

where;

Re = Reynolds number = $V_{in}H/\nu$
Pe = Peclet number = Re Pr

Thus, forced convection scales with the following dimensionless parameters;

Reynolds number: Re= $V_{in}H/\nu$

Peclet number: Pe = Re Pr

$$Gr/Re^2 = \frac{g\beta(T_H - T_C)H^3}{\upsilon^2} \Big/ \left(V_{in}H/\upsilon\right)^2$$

To summarize, the scaling parameters that need to be matched between the full and scaled models for mixed convection are; the geometric aspect ratios, Reynolds number, Grashof and Prandtl numbers or Rayleigh and Prandtl numbers.

3.2: Working Fluid:

The above scaling parameters depend on geometry, flow conditions and fluid properties. Geometry and flow conditions can be controlled to match the required scaling parameters, but fluid properties need to be given special care due to their importance and interaction with the flow field, the following section will consider this aspect in more detail.

3.2.1: Choice of Scaling Fluid:

As stated in the previous section, the working fluid for the scale model must be chosen to match the expected Rayleigh, Grashof, and Reynolds numbers of the full scale model under normal operation conditions. Although those factors are the only scaling parameters that appear in the governing equations, Olson (1986) reported two additional factors influencing the choice of the scaling fluid. These parameters preserve the ratio

between the magnitude of the horizontal and vertical wall heat fluxes. The first additional parameter suggested by Olson (1986) is the optical depth of the zone, which is defined as the product of the mean absorption coefficient of the fluid, a, and the characteristic dimension of the zone, where:

Optical depth of the enclosure = aH

The second parameter suggested by Olson (1986) is the ratio of the convective heat transfer from the vertical walls to the net radiant transfer from the top to the bottom of the enclosure.

The view factor was neglected since the geometry shape should be identical between full-scale and small-scale experiments and the assumption was made that the building materials for the full and scaled model have the same optical characteristics in the infrared spectrum. Also note that the radiation heat transfer has been linearized with the mean temperature.

Thus, the convection to radiation ratio parameter can be derived as follows,

$$\frac{\text{vertical wall convection}}{\text{ceiling / floor radiation}} = \frac{hA_v}{\varepsilon\sigma A_h}\frac{(T_H - T_C)}{(T_t^4 - T_f^4)} = \frac{h(HW)}{\varepsilon\sigma(WL)}\frac{(T_H - T_C)}{(T_t^4 - T_f^4)}$$

$$\frac{\text{vertical wall convection}}{\text{ceiling / floor radiation}} = = \frac{h}{\varepsilon\sigma}\frac{H}{L}\frac{(T_H - T_C)}{(T_t^4 - T_f^4)} \qquad (3.27)$$

where;
h = heat convection coefficient from the vertical wall
T_t = Ceiling temperature
T_f = Floor temperature
ε = Ceiling/floor emissivity
σ = Stefan Boltzman constant

To further simplify the equation, substitute for the heat convection coefficient, h, with Nusselt number for the vertical wall, $h = Nu\ k_f / H$, where k_f is the fluid conductivity. Thus;

$$\frac{\text{vertical wall convection}}{\text{ceiling / floor radiation}} = Nu \frac{k_f}{\varepsilon 4\sigma T_m^3 L} \frac{(T_H - T_C)}{(T_t - T_f)} \tag{3.28}$$

where:
Nu = Vertical wall Nusselt number

T_m = Enclosure mean temperature = $\frac{T_H + T_C}{2}$

Further, if we set the surface emissivity to 1, Equation 3.27 reduces to:

$$\frac{\text{vertical wall convection}}{\text{ceiling / floor radiation}} = Nu\ CR \frac{(T_H - T_C)}{(T_t - T_f)} \tag{3.29}$$

$$\text{where; } CR = \frac{k_f}{4\sigma T_m^3 L} \tag{3.30}$$

The convection to radiation ratio is a function of Nusselt number, temperature differences, fluid properties, mean temperature, and geometry. The geometry, temperature differences and the mean temperature of the geometry can be controlled; leaving the fluid properties as the determining factors in this ratio.

Thus the complete list of the scaling parameters for mixed convection within enclosures is:

- Ra
- Pr
- Re
- Gr/Re^2

- Geometric aspect ratios
- $\frac{\text{vertical wall convection}}{\text{ceiling / floor radiation}}$
- The optical depth of the enclosure (aH)

Application of the scaling parameters shows first of all, that air is not an acceptable working fluid for natural convection in the scale model. The Rayleigh number is an important parameter in this analysis. Rayleigh number in a full-scale enclosure with a temperature difference of about 15 ^{o}C will be on the order, Ra~10^{10}. To match this Rayleigh number while reducing the size of the enclosure, the temperature difference needs to be increased by a factor of, $(H_{full}/H_{model})^{3}$, thus for a ¼ scale model enclosure, the required temperature difference in the model, to match Ra in the full scale room is 64 times full scale room temperature difference. This would translate to a 960 ^{o}C temperature difference in the model. In addition, the optical depth of the scale model, H_o= aH, will be smaller than that of full size room by the scaling factor used.

Second, as pointed out by Olson (1986) water is not an acceptable scaling fluid because the water Prandtl number, (~7), is much higher than that of air, (~0.7), and its optical depth is much greater than that of air. In fact, water is opaque to infrared radiation, and will eliminate the radiant exchange in the enclosure.

Weber (1980) and Olson (1986) showed that using high-density gas as the scaling fluid is a good choice. Dense gases have several characteristics that enable them to meet most of the scaling parameters required to scale natural convection in enclosures. Weber (1980) used R12 as the scaling fluid while Olson (1986) used R114 as the scaling fluid. Both of them have showed that R114 was the best scaling fluid, and actually R114 was Weber's first choice.

Dense gases are expected to be good scaling fluids for several reasons. First, their high density enables scaling of the full size experiment to an acceptable size. Second, the Prandtl number of the dense gases (~0.7) is the same order of magnitude as of air. Also, dense gases are transparent, i.e. optically thin, which will give much better scaling of the radiation interaction inside the zone. Thus, it is expected that dense gases better match the scaling parameters of natural convection than water and thus provide accurate scaling results. Although refrigerants are better than water for scaling natural convection within enclosures, especially in the optical properties part, they do not act the same as air, i.e. refrigerants are participating mediums. Refrigerants absorb and emit energy in contrary to air, which is a non-participating medium. Still they have proved to give good results when they were used as scaling fluids (Olson et al., 1990).

The scaling parameters required for forced convection are, in general, similar to those of natural convection. Looking at the scaling parameters required for forced convection, we can see that the only extra parameter is Reynolds number. Thus, by matching the natural convection parameters, one needs only to match the Reynolds number to ensure proper scaling of forced convection flows. Although forced Convection is more prevalent in engineering applications, scaling for natural convection is the first step in scaling forced convection flows. We need to report that no one was able to get a perfect scaling of natural convection within enclosures.

4. Experimental Facility Design

4.1 Objectives:

Our objective in this project is to build an experimental facility that will allow us to measure the natural convection heat transfer and flow field. The experimental facility will be designed to achieve our goal being able to conduct accurate scaling natural convection experiments, and at the same time be able to get accurate velocity measurements of the flow field. Since we have already specified that PIV is our candidate technique for flow visualization, the facility will be designed to facilitate the used of this system.

4.1.1 Heat Transfer and Transport Experiments:

The natural convection validation experiments conducted will use air as the working fluid to reduce the cost of the experiments. The Rayliegh number obtained will be of order 10^8. The heat transfer experiments will be single zone experiments, but the experimental facility will be designed to accommodate two zone experiments.

4.1.2 PIV Flow Measurements Capabilities:

Flow visualization reported in the literature, in most of the cases, used smoke or dye to visualize the flow. These techniques do not give accurate velocity measurements of the flow field, as stated earlier. PIV, on the other hand, is an accurate technique to conduct velocity measurements of the flow field. Unfortunately, PIV is not easy to use, it needs

some skills in its preparation and operation. Experimental facility design must take into consideration those difficulties.

The PIV system used works by illuminating the flow field twice using a laser sheet, the image reflected from seeding particles, which are introduced into the flow, is captured using CCD camera at each laser pulse. The two images are then analyzed using statistical based programs.

This means that the usage of PIV system requires transparent walls, and way to introduce the seeding particles. The type of the seeding particles used will decide which technique to use for its introduction. The PIV system, as will be explained later, needs to be aligned to make sure that we have a good laser sheet. Then the CCD camera needs to be calibrated to the laser sheet, so that we get a clear image of the flow field. Once those steps are done, the seeding particles are then introduced into the flow field; they need to be introduced in a way that will have a minimum effect on the flow field inside the enclosure. After the seeding particles start to follow the flow field inside the enclosure we can start taking pictures of the flow field. In order to cover the entire flow field we need to be able to move the camera vertically in a fixed horizontal distance from the laser sheet, this required building a traversing system to move the camera while obtaining fixed coordinates of the system.

Using PIV for natural convection poses further difficulties due to the nature of the flow field inside the enclosure. Natural convection flow field is a delicate one, which needs care when introducing any seeding particles into the system. The seeding particle has to be neutrally buoyant, has a high refractive index to reflect laser, and small enough

to follow the flow field. Detailed discussion about the seeding particles will be given in chapter 6.

4.2 Scale Model Overall Design

The experimental facility is a 1/5 scale model of the full size building shown in figure 3.1. The scaled model dimensions are

- Height: $H_m = 0.2*H_f = 0.2*$ 2.54 m = 0.508 m = 1.67 ft
- Length: $L_m = 0.2*L_f = 0.2 *$ 3.914 m = 0.782 m = 2.567 ft
- Width: $W_m = 0.2*W_f = 0.2 *$ 4.067 m = 0.813 m = 2.67 ft
- Volume: $V_m = 0.323\ m^3 = 11.44\ ft^3$

The enclosure's aspect ratios are;

$$A_{:L} = \frac{H}{L} = 0.625,\ A_W = \frac{H}{W} = 0.649 \approx 0.65$$

In order to gain visual access to the inside of the enclosure the model was constructed of 0.5 inch thick clear Plexiglas. The mechanical properties of plexiglas are suitable for the application at hand. The thermal properties of Plexiglas are also suitable for this application, Plexiglas has a thermal conductivity is 3.7 ($W/m^2.K$) and a specific heat of 1.465 (kJ/kg.K). One disadvantage of using Plexiglas is the length of time required for the enclosure to reach steady state.

The experimental facility will contain two isothermal walls and opposing cold and hot walls. The ceiling, floor and side walls of the enclosure will be insulated. Figure 4.1 shows a 2D sketch of the scaled experimental facility, with the dimensions given in inches.

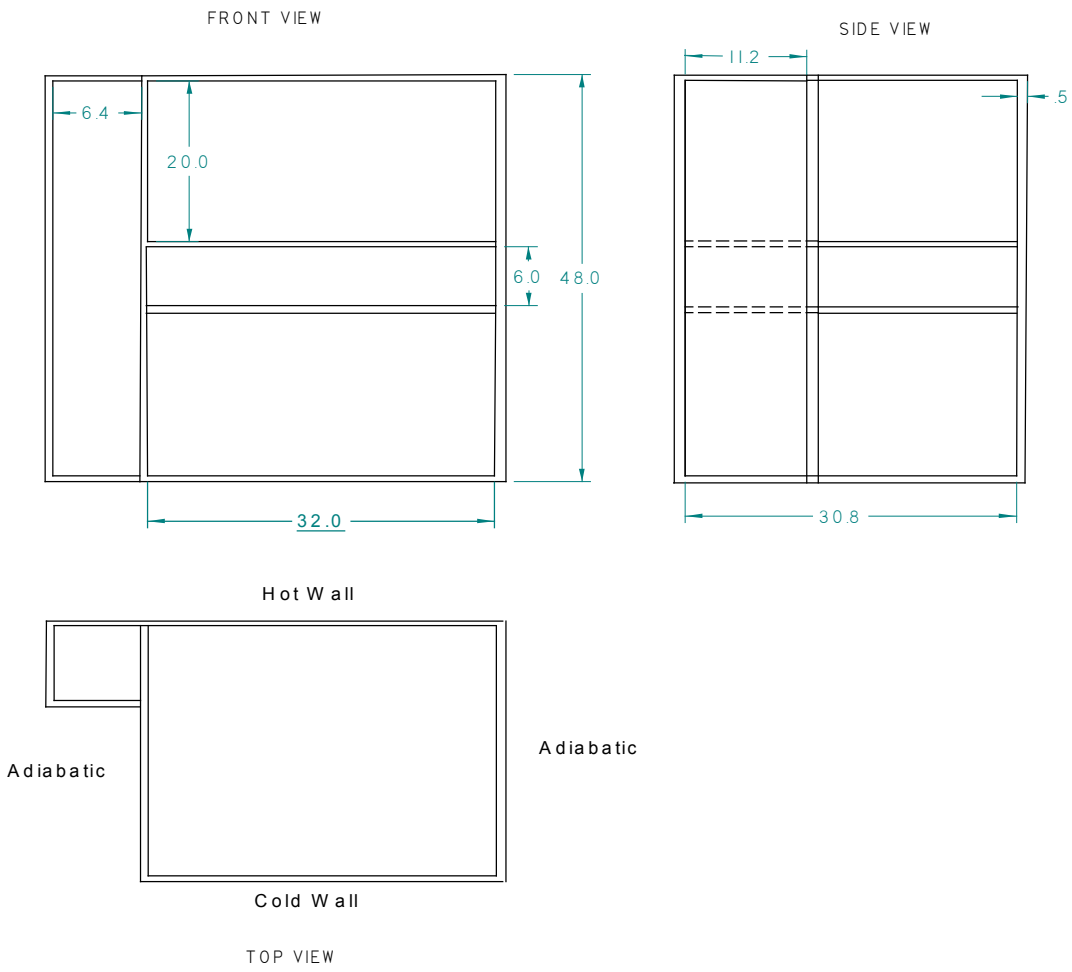

Figure 4.1: 2D views of the Scaled Experimental Facility

The Plexiglas walls were assembled using aluminum corners, the assembly is shown in figure 4.2. To ensure tight sealing of the enclosure, silicon caulk was applied at the edges of the Plexiglas.

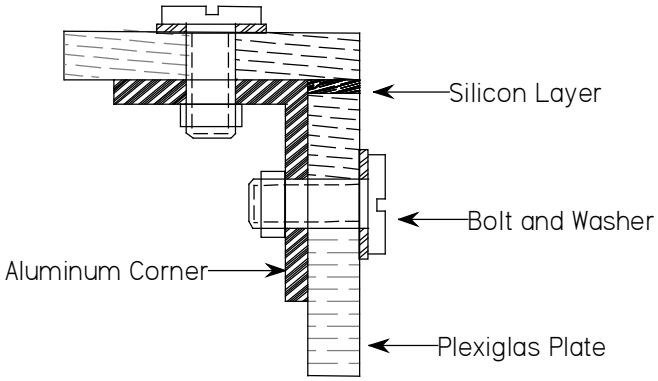

Figure 4.2: Plexiglas-Aluminum Corner Assembly

4.2.1 Hot and Cold Walls

Natural convection experiments required the existence of two isothermal walls, one at high temperature and the other at low temperature. In order to achieve this, heating and cooling panels were attached to the back of the Plexiglas walls. The heating panel was constructed using a nickel-chromium alloy resistance wire. The heating wire was attached to a sheet rock base and covered with a thick layer of plaster. The plaster served as an electrical insulator and increased the thermal mass of the panel. Figure 4.3 shows a cross sectional view of the heating panel. In order to obtain a uniform surface temperature a 0.125 in thick aluminum plate was attached to the outer surface of the heating panel using thermal paste.

The nickel-chromium heating wire diameter was 18 gage, and was arranged as shown in figure 4.4 with 4 inch spacing between the wires. The input power to heating panel was controlled using a variac. The variac had a control range of 0 – 140 volts. The electrical resistance of the heating panel was 45.6 ohms at 20 ^{o}C.

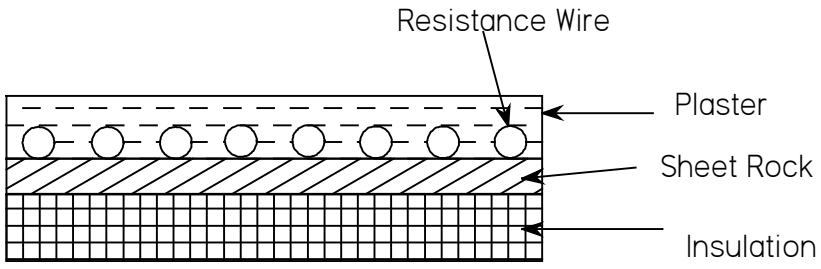

Figure 4.3 Sectional View of Heating Panel

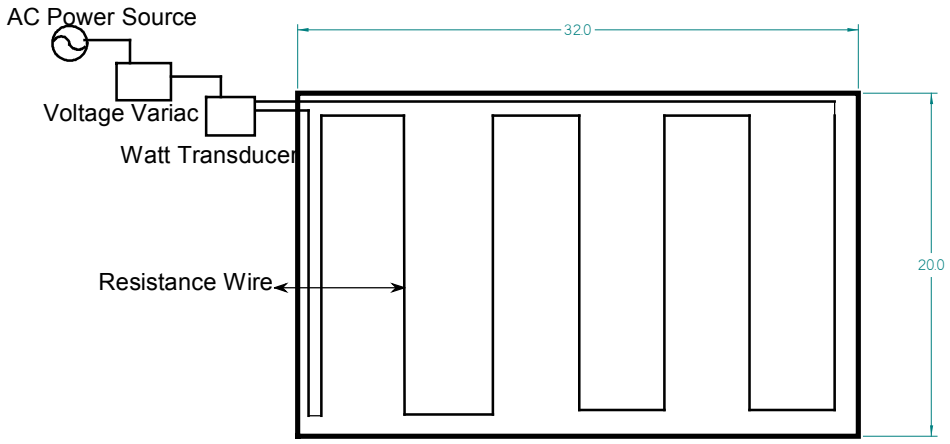

Figure 4.4: Heating Panel Schematic

The cold side of the experimental facility was obtained by attaching a cooling panel to the outside of the Plexiglas wall. The cooling panel is basically a 0.375 inch thick aluminum plate to which ½ in copper tubes are attached using an epoxy with high thermal conductivity. Figure 4.5 shows a sectional view of the cooling panel. The cooling panel is connected to a constant temperature bath/circulator, "RTE-710" from NESLAB. The constant temperature bath controls the fluid temperature with an accuracy of $\pm$ 0.1^{o}C. The chiller's pump is a constant speed circulation pump. The working fluid used in the bath is a 50/50 mix of Ethylene Glycol and tap water by volume. The flow rate to the

bath was measured and calibrated using a precision scale and a stopwatch. Figure 4.6 shows a schematic of the cooling system used.

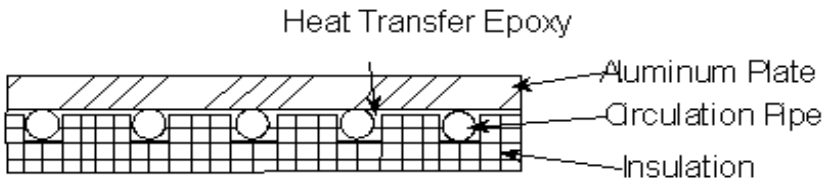

Figure 4.5: Cross Sectional View of Cooling Panel

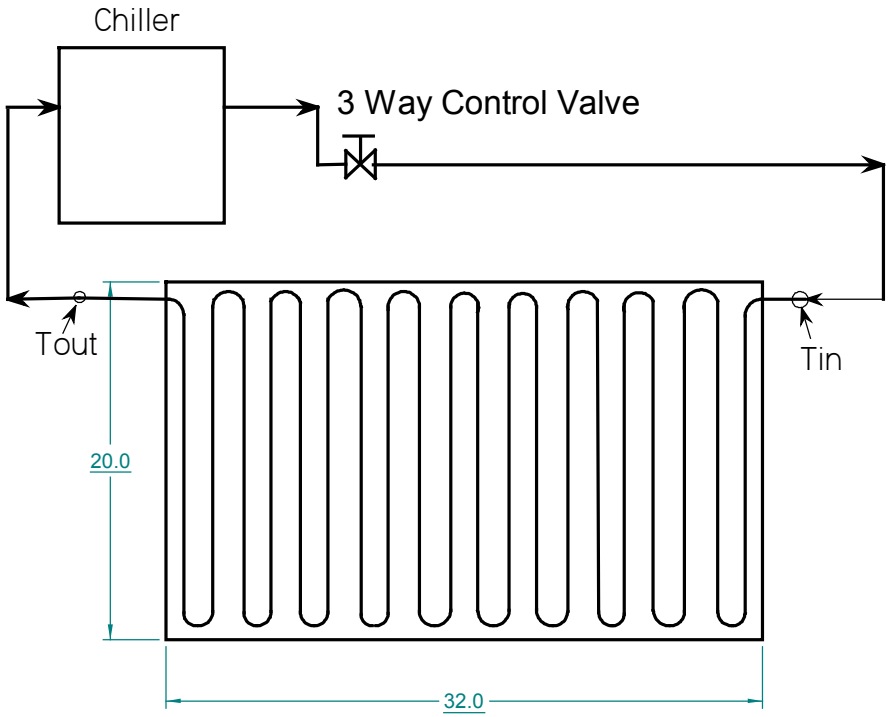

Figure 4.6: Schematic Diagram of Cooling System

4.2.2 Enclosure Insulation

The experimental facility was insulated using Square Edge Styrofoam manufactured by Dow chemical. The insulation is 3 inch thick with a thermal resistance factor (R = 15 ft^2.hr.F/Btu =2.642 m^2.K/W). To ensure that the experimental facility was well insulated, three insulation layers were used to insulate the isothermal walls (R_{iso} = 45 ft^2.hr.F/Btu),

and two layers were used for the other walls and the ceiling (R_{side} = 30ft^2.hr.F/Btu). One layer was used on the floor due to space restrictions.

4.3 Instrumentation

4.3.1 Temperature Measurement

Temperature measurement is the most important measurement of the heat transfer experiments. Temperature measurements in this experimental facility can be divided into four groups, gas temperature, enclosure surface temperature, insulation temperature, and chilled ethylene glycol mixture temperature difference. T type thermocouple wires and probes were used for all temperature measurements.

All of the thermocouple wires and probes were calibrated using a controller water bath with a precision of ± 0.1 ^{o}C. The calibration procedure is presented in details in section 4.6.1.1.

4.3.1.1 Gas Temperature Measurement

The temperature profile inside the enclosure is measured using thirty-three 30-gage T type thermocouples. Those 33 thermocouples measured air temperatures in a single plane and are attached to a movable frame. The frame is constructed from ¼ in. diameter rods and the grid was formed using thin wires. The frame was placed on two rods, reaching from the front to the back of the enclosure, using two linear bearings at its top corners. The frame was moved manually using two rods that are attached to it, and were extend outside the enclosure. The thermocouples were closely spaced near the isothermal walls and further spaced closer to the center. The thermocouples were extended 1 inch beyond the frame to make near wall measurements. This resulted in uncertainty in the

thermocouple locations due the difficulty in controlling the spatial location of the thermocouple wire accurately. The movable frame was located was two inches from the isothermal walls, which placed the near wall measurements outside the boundary layer. Nevertheless, these measurements should provide some indication of the temperature profile that exists inside the enclosure. Figure 4.7 shows a view of the temperature measurement plane with the dimensions shown in inches; no thermocouples are located on the top corners of the grid, where linear bearings are located.

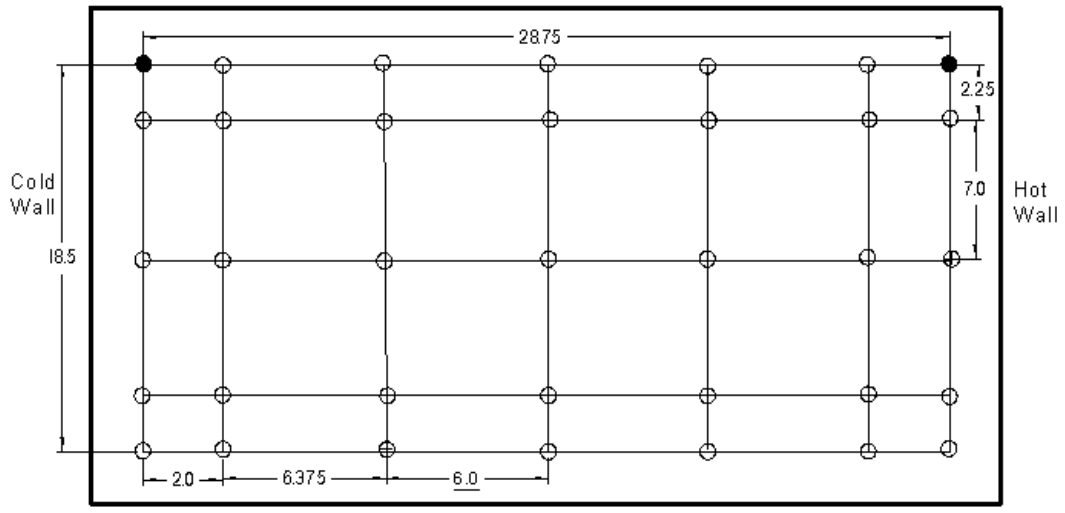

Figure 4.7: Thermocouple Frame Front View

4.3.1.2 Surface Temperature Measurement

The isothermal wall temperatures were measured by four 30 gage T-type thermocouples placed at the centers of each quadrants of the isothermal wall. The thermocouples were attached to the wall using a high conductivity epoxy. Temperatures was also measured for top, bottom and the back of the enclosure. The top and bottom

surface temperatures were measured using two thermocouples, and the sidewall surface temperature was measured with a single thermocouple. The front panel temperature was not measured because of the flow visualization requirement.

4.3.1.3 Ethylene Glycol Temperature Measurement

The Ethylene Glycol temperature difference across the cooling panel is an important measurement for heat balance calculations. This temperature difference is used to calculate the heat transfer from the cold wall. The temperature difference was not measured directly; rather it was calculated from direct measurements of the inlet and outlet fluid temperatures. The fluid temperature was measured using T-type thermocouple probes. The inlet and outlet temperatures were then used to calculate the temperature difference.

4.3.1.4 Insulation Temperature Difference Measurement

The heat transfer across the wall insulation was estimated by measuring the temperature difference across the insulation for the isothermal walls, roof, floor, and back wall of the enclosure. Symmetry is assumed for the insulated sidewalls. 24 gage T-type thermocouple were used for this measurement. Three thermocouples were placed on each face of the insulation for the isothermal walls, while two were placed on the top and sidewall. The thermocouples were placed at the centers of the halves for the sidewall and top, and diagonally aligned for the isothermal walls.

4.3.2 Heating Power Measurement

The only input power to the enclosure was the electrical power used in the heating panel; this was measured using a watt transducer. Since the heating wire resistance was 45.6 Ohm, as stated earlier, and the maximum voltage provided to the wire was 140 Volts, the maximum heating panel power was:

$$\text{Power} = VI = V^2/R = (140)^2/45.6 = 429.8 \text{ Watt}$$

where;
V = Input voltage, volt
I = Input current, amper

An Ohio Semitronics watt transducer; model AWG-001D, which is a single-phase two-wire AC watt transducer with a full-scale rating of 500 Watts was selected for this application. The watt transducer has an output voltage of ± 10 Volt DC (50 W/V) and an accuracy is ± 0.2% RDG ±0.04% F.S.

4.3.3 Data Logging System

Data was logged using a Fluke data logging system. Four 20 channel Fluke data loggers were used to measure temperature and DC voltage. Two types of data loggers were used; the Fluke Hydra and the Fluke NetDaq.

The data logging systems have dynamic data exchange capabilities, which will enable direct loading of the data into an excel sheet. This property was used to write a data logging program to read and process the data collected by the four data loggers. A scanning interval of 5 minutes was used to record the measured temperatures.

4.4 Working Fluid Selection

The scale analysis in the previous chapter showed that high density gases could be successful candidates for scaling natural convection in enclosures. In fact, high density gases have been used as scaling fluids successfully before. Olson (1986) used R114 as the scaling fluid for natural convection in enclosures. R114 proved to be a good scaling fluid, Olson (1986) proved this by comparing his results with the full-scale experimental results obtained by Ferm (1984). Weber (1980) has also used a refrigerant, R12, as the scaling fluid with good results.

Unfortunately, nowadays neither R114 nor R12 can be easily obtained at a reasonable cost due to environmental regulations. Thus, a new scaling fluid must be found. Since previous results showed that refrigerants are good scaling fluids, the new scaling fluid was selected from this group of fluids. Refrigerants have the required properties of the scaling fluids, i.e. high density, Prandtl number closer to air, and a low absorption coefficient.

Since the dimensions of the enclosure were predetermined, the analysis was based mainly on the refrigerant's ability to match the full-scale Rayleigh number. Comparison among scaling fluid candidates was made in terms of fluid properties, and the expected Rayleigh number under normal operating conditions ($T \sim 25^{o}C$, $\Delta T = 15\ ^{o}C$). Refrigerants will be used for scaling in the gaseous phase, and since they have similar thermo physical properties at normal operating conditions, as shown in table 4.1. In addition to the fact that they are transparent in visible, in the gaseous phase, and the good scaling properties reported for two different refrigerants, we can assume that their radiation properties are similar.

Any scaling fluid must be stable, non-toxic, non-combustible and chemically inert. Fortunately, most of the available refrigerants meet those requirements. Table 4.1 gives a short list of candidate refrigerants with their properties. Air properties are given in this table for comparison purposes.

Table 4.1: Scaling Fluids Properties

Fluid	Temp.	Pressure	Density	Quality	Thermal Expansion Coeff.	Prandtl number	Rayleigh number ($\Delta T = 15\ ^{\circ}C$)	ΔT (Ra=3.036 E 10)
	[C]	[kPa]	[kg/m^3]	[mol/mol]	[k^{-1}]			[C]
Air (full size)	20	101.3	1.20	Superheated	3.41E-03	0.722	3.04E+10	15..00
Air (scaled model)	20	101.3	1.20	Superheated	4.17E-03	0.722	2.97E+08	1534.79
R227ea	20	101.3	7.25	Superheated	3.73E-03	0.750	2.18E+10	20.84
R236fa	20	101.3	6.54	Superheated	3.98E-03	0.754	2.13E+10	21.38
R123	20	101.3	1477.00	Sub cooled	1.35E-03	5.763	1.68E+12	0.27
R124	20	101.3	5.83	Superheated	3.77E-03	0.749	1.43E+10	31.85
R114	20	101.3	7.34	Superheated	3.81E-03	0.745	2.59E+10	14.92

A quick look at Table 4.1 shows first that the refrigerants listed have comparable results, except of R123, which is still liquid at 20 ^{o}C. Row 2 of table 4.1 shows the results of using air in the scaled model. The temperature difference required for air to match the Rayleigh number of the full-size enclosure (~ 10^{10}) is 1534.79 ^{o}C, which is impossible to achieve. All of the other refrigerants shown in table 4.1 have a Rayleigh number of the same order of magnitude as air (~10^{10}). The temperature difference required to obtain the full enclosure Rayleigh number is acceptable for all of these refrigerant candidates, except R123. The required temperature difference ranged from 14.9 ^{o}C for R114 to 31.85 ^{o}C for R124.

The scaling fluid candidates are close in terms of their properties, and even in matching the required Rayleigh number and required temperature difference. Thus, the scaling fluid choice was based on availability and cost factors. As stated earlier R114 is the best scaling fluid for natural convection in enclosures, but it is hard to obtain and costs about $1000 for a 30 lb can.

Two other scaling fluids R227ea and R236fa are substitutes for R114. The temperature difference required for matching Rayleigh is reasonable also 20.84, and 21.38 ^{o}C respectively. Unfortunately both of these refrigerants are very expensive. R124 has acceptable scaling properties, high density, with a good Prandtl number and Rayleigh number match. In addition the temperature difference required is acceptable (31.85 ^{o}C). Also, R124 is safe, inflammable, colorless, odorless, and easy to get at a comparatively low price ($10/lb). Therefore, R124 was selected as the scaling fluid for the experimental facility.

4.5 Proposed Refrigerant Charging Method

The experimental facility was not charged with refrigerant in this project, and thus no experiments with refrigerant as the working fluid were conducted. This is due to the fact that our main objective in this project was to develop an accurate flow visualization technique to measure the flow velocity inside the enclosure. To achieve this goal we felt that it was sufficient to work with air as the working fluid. Nevertheless, a refrigerant charging system is proposed as future work with the suggested scaling fluid.

Since the scaling fluid chosen for this experiment has a density that is 4.86 times larger than the air density (ρ_{R124} = 5.83 kg/m3), it can be introduced into the enclosure using this density difference, i.e. the refrigerant will displace the air inside the enclosure.

The refrigerant can be introduced to the enclosure slowly at low pressure and speed. This is necessary to ensure minimal mixing between the air and the refrigerant.

Figure 4.8 shows the technique that can be used to fill the enclosure with refrigerant. The R124 tank is connected to a coil through a pressure regulator. The coil, which is made of ½" copper tubes, is used to reduces the refrigerant pressure and increase its temperature. The coil outlet is connected to a "control" tank. This tank has control valves on its inlet and outlet, and it also has a pressure gauge. The control tank can be used to control the refrigerant pressure and velocity as it enters the enclosure. An oxygen analyzer at the outlet air vent can be used to determine when the refrigerant concentration in the enclosure is at an acceptably high level.

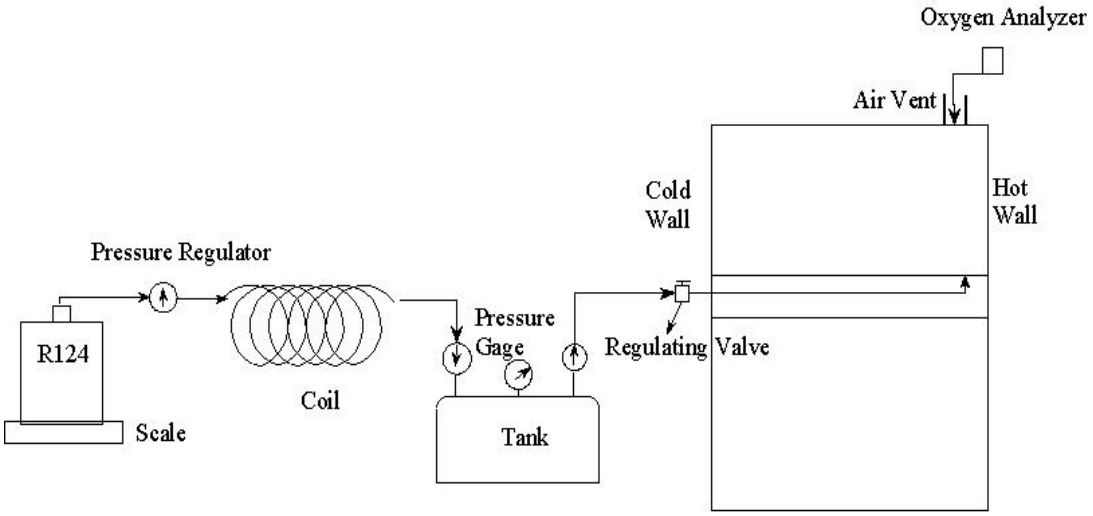

Figure 4.8 Schematic of R124 Charging Technique

4.6 Experimental Uncertainty Analysis

Uncertainty or error estimation of the experimental results is an important aspect of the project. Uncertainty estimation must be made for the measured and calculated

quantities. The measured data uncertainty is determined by the measurement technique, while the calculated quantities are estimated from that of the primary measurements using the method proposed by Kline and McClintock (1953). The uncertainty of the calculated result in terms of the primary uncertainties is given as,

$$e_R = \pm\sqrt{\left(\frac{\partial R}{\partial x_1}e_1\right)^2 + \left(\frac{\partial R}{\partial x_2}e_2\right)^2 + \ldots + \left(\frac{\partial R}{\partial x_n}e_n\right)^2} \qquad (4.1)$$

where:
R = the calculated results, $R = R(x_1, x_2, .. x_n)$
e_R = the uncertainty interval in the result
e_i = the uncertainty interval in the i^{th} variable
$\frac{\partial R}{\partial x_i}$ = the sensitivity of the result to a single variable, x_i

In the following sections the uncertainty in the primary and calculated quantities will be estimated.

4.6.1 Uncertainty in Primary Measurements

The uncertainty in the primary measured quantities is determined by the measurement devices and techniques used. This uncertainty propagates through the subsequent calculations to the final results.

4.6.1.1 Temperature Measurement Uncertainty

Type-T thermocouples and probes were used in conjunction with three data logging systems to measure both air and surface temperatures in the facility. Since the response time of the 30 (ga.) wires was considerably shorter than the response time of the heated panels, the wire was ideally suited for surface temperature measurements. The 24 ga.

wires used for measuring the insulation temperature difference were suitable for their purpose too since our goal was only to estimate heat losses through insulation at steady state. Ethylene Glycol temperature was measured using two T-type thermocouple probes.

Three different models of Fluke data logging systems were used: one Hydra data logger model 2625A, one Hydra Series II model 2635A and two NetDAQ model 2640A.

All the thermocouples used in temperature measurement for this experiment were calibrated using a constant temperature chiller with an operating range of -40 to 150°C and a temperature stability of ± 0.05°C. The user can set the temperature of the water bath to within ± 0.1°C. Each of the thermocouples was immersed in the bath fluid after the bath had stabilized at the set point. The temperature measurement of each thermocouple was scanned and recorded by the data logger over a period of time.

The stability of the thermocouple itself was tested for 4 of the 30 (ga.) thermocouples with lengths similar to the rest of the thermocouple wires. The test was conducted by setting the chiller at a reference temperature, leaving the chiller to stabilize at the required temperature for about 30 minutes and then recording the reading of the thermocouples at an interval of 1 second for 5 minutes. The readings of each thermocouple were used to find the average reading, which was used to find the calibration curve of the thermocouple. Deviation of the thermocouple readings from the average reading was used to estimate the scatter of the thermocouple readings. The readings of the thermocouples were within ± 0.07 ^{o}C, figure 4.9 shows the scatter of one of thermocouple wires readings.

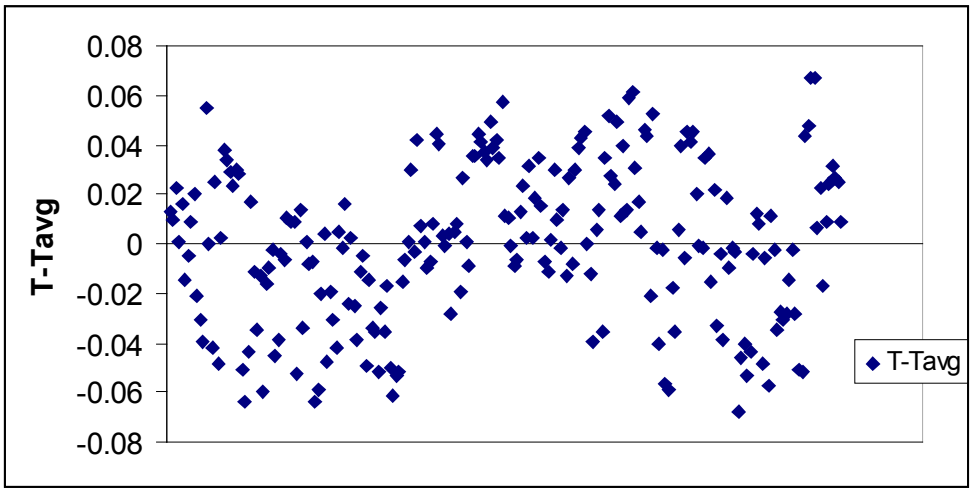

Figure 4.9: Thermocouple Stability Test

The uncertainty associated with the thermocouple wires is then calculated as

$$e_{TC} \approx \pm\sqrt{e_{Tref}^2 + e_{Tstab}^2} = \pm\sqrt{(0.1)^2 + (0.07)^2}$$

$$e_{TC} = \pm 0.122\ ^{o}C \qquad (4.2)$$

The same calibration procedure was conducted for the two T type thermocouple probes used to measure the ethylene glycol. The stability test conducted for the probes showed a stability of $\pm 0.12\ ^{o}C$. Thus, the uncertainty associated with measuring the water ethylene glycol mix using the probes is

$$e_{Probe} \approx \pm\sqrt{e_{Tref}^2 + e_{Tstab}^2} = \pm\sqrt{(0.1)^2 + (0.12)^2}$$

$$e_{Probe} = \pm 0.156\ ^{o}C \qquad (4.3)$$

4.6.1.2 Electrical Power Measurement Uncertainty

The power input to the heating panel is measured using a watt transducer. The watt transducer is manufactured by Ohio Semitronics. Inc.; model AWG-001D. This model is

a single-phase two-wire AC watt transducer with 500 Watt full scale. The output signal of the transducer is a DC voltage with ± 10 Volt range (50 Watt/Volt). The watt transducer accuracy is ± 0.2% RDG or ±0.04% F.S.

If the heating power used in this experiment is 100 Watt, the uncertainty associated with this power is the largest of the full scale or reading errors. The full-scale uncertainty for this limit is given as

$$\text{Full-scale uncertainty} = e_{full} = \pm 0.04\% * 500 = \pm 0.2 \text{ W}$$

While the percent reading uncertainty is

$$e_{reading} = \pm P * 0.002 = 100.(0.002) = \pm \frac{e_{full}}{0.002} = \frac{0.2}{0.002} = \pm 0.2 \text{ W}$$

Apparently 100 Watt is the limit at which the reading and full-scale uncertainties are equal. Thus the full-scale uncertainty will be used for the watt transducer reading as long the input power is less than 100 W.

$$e_{trns} = \pm 0.2 \text{ Watt} \quad \text{(Power < 100 Watt)}$$

$$e_{trns} = \pm 0.002 * \text{Power (Power>100 Watt)} \tag{4.4}$$

The watt transducer is connected to a NetDaq data logger; this data logger will add an uncertainty in its voltage reading,

$$e_{Fluke} = \pm 0.042\% + 3.9 \text{ mV}$$

The total uncertainty of the power reading due to the data logger's reading uncertainty can be estimated as

$$e_{Fluke} = \left(0.00042.V_{Fluke} + 0.0039\right)\frac{\Delta Range}{\Delta V} \tag{4.5}$$

where:
e_{Fluke} = Fluke data logger uncertainty, V
V_{Fluke} = voltage measurement by Fluke, Vdc
ΔRange = measurement range of transducer, W
ΔV = range of output signal of transducer, Vdc

The watt transducer used in this experiment has a range of 500 and output signal of 10 volts. Thus, the maximum uncertainty associated with the watt transducer used is

$$e_{Fluke} = (0.00042.10 + 0.0039)\frac{500}{10} = \pm 0.405 \text{ Watt} \tag{4.6}$$

The total uncertainty of the watt transducer reading is

$$e_{WG001} = \pm\sqrt{(0.2)^2 + (0.405)^2} = \pm 0.452 \text{ W (Power < 100 W)}$$

$$e_{WG001} = \pm\sqrt{(0.002.\text{ Power})^2 + (0.405)^2} \text{ W (Power >100 W)} \tag{4.7}$$

The power introduced to the heating panel was less than 100 W for all the experiments conducted here.

4.6.1.3 Flow Rate Uncertainty

The NESLAB RTE-140 refrigerated bath/circulator was used to circulate the chilled ethylene glycol-water mixture through the cold panel. The circulator pump is a constant speed pump that has a flow rate of 15 (lpm) at zero (m) head and zero (lpm) at 4.9 (m) head. The pump was able to circulate ethylene glycol-water through the panel.

No flow meter was used to measure the flow rate through the cold wall continuously. Rather, the flow rate through the cold panel was calibrated using a precision weight scale, a bucket, and a stopwatch. The calibration process was repeated several times and an average value was used for calculations. The calibration process was conducted in situ

after the chiller has stabilized at the set temperature. Before the calibration process started the bucket was placed at the precision scale and the scale was zeroed. An outlet valve to the piping system is then adjusted until the desired flow rate is reached. The stopwatch and water flow is started simultaneously and the bucket is filled to a predetermined point. Once this point is reached, the stopwatch and water flow is stopped and the bucket is weighed and the value recorded. The flow rate of the chiller was then calculated using

$$m^{o} = \frac{m_{EtGl}}{t} \tag{4.8}$$

where:
m^{o} = Ethylene Glycol water mixture mass flow rate, kg/sec.
m_{EtGl} = Ethylene Glycol mass, kg.
t = time, second.

The precision weight scale used is an AND electronic balance model, EP-20KA, with an accuracy up to ± 0.1g. Thus the precision scale has an error

$$e_{scale} = \pm 0.1 \text{ g} = \pm 0.0001 \text{ kg}$$

The stopwatch used has a precision of 0.01 second, but the human error is higher than the stopwatch accuracy. The human error is estimated to ± 0.2 second.

$$e_{human} = \pm 0.2 \text{ sec.}$$

The ethylene glycol-water density was estimated at the chiller's setting temperature. The total uncertainty of the flow rate can be estimated by

$$e_{m^{o}} = \pm \sqrt{\left(\frac{\partial m^{o}}{\partial t} e_{human}\right)^{2} + \left(\frac{\partial m^{o}}{\partial m} e_{scale}\right)^{2}} \tag{4.9}$$

The average flow rate was calibrated to be 0.02 kg/sec; an average of 575 gram of ethylene glycol-water mixture took an average time of 28.72 second. The flow measurement accuracy can then be estimated to,

$$e_{m^o} = \pm\sqrt{\left(-\frac{0.575}{(28.72)^2}.0.2\right)^2 + \left(\frac{1}{28.72}.0.0001\right)^2}$$

$$e_{m^o} = \pm\ 1.395\ e\ -5\ kg/sec.$$

4.6.2 Uncertainty in Intermediate Results

4.6.2.1 Cold Wall Temperature Difference Uncertainty

The temperature difference of the ethylene glycol across the cold wall is calculated by subtracting the temperatures measured by the thermocouple probes at the inlet and outlet of the cold wall panel. The temperature difference is calculated as

$$\Delta T = T_{out} - T_{in} \tag{4.10}$$

The uncertainty associated with this calculation can be found using equation 4.1;

$$e_{\Delta T} = \pm\sqrt{\left(\frac{\partial(\Delta T)}{\partial T_{out}}e_{Tprobe}\right)^2 + \left(\frac{\partial(\Delta T)}{\partial T_{in}}e_{Tprobe}\right)^2} \tag{4.11}$$

$$e_{\Delta T} = \pm\sqrt{\left(1.e_{Tprobe}\right)^2 + \left(1.e_{Tprobe}\right)^2} = \sqrt{(0.156)^2 + (0.156)^2}$$

$$e_{\Delta T} = \pm 0.22\ ^oC$$

where:

$$\frac{\partial(\Delta T)}{\partial T_{out}} = \frac{\partial(\Delta T)}{\partial T_{in}} = 1$$

4.6.2.2 Cold Wall Heat Transfer Uncertainty

The cold wall heat transfer can be calculated via

$$Q_{out} = m^{o}_{EtGl}.Cp.\Delta T \tag{4.12}$$

The uncertainty of the heat transfer can be estimated using equation 4.1;

$$e_{Qout} = \pm\sqrt{\left(\frac{\partial Q_{out}}{\partial m^{o}_{EtgL}} e_{m^{o}_{EtgL}}\right)^2 + \left(\frac{\partial Q_{out}}{\partial \Delta T} e_{\Delta T}\right)^2}$$

where:

$$\frac{\partial Q_{out}}{\partial m^{o}_{EtGl}} = Cp.\Delta T$$

$$\frac{\partial Q_{out}}{\partial \Delta T} = Cp.m^{o}_{EtGl}$$

Thus, the uncertainty in calculating the power extracted by the cold wall from the zone is:

$$e_{Qout} = \pm\sqrt{\left(Cp.\Delta T.e_{m^{o}_{EtgL}}\right)^2 + \left(Cp.m^{o}_{EtGl}e_{\Delta T}\right)^2} \tag{4.13}$$

The uncertainty of the heat extracted will be calculated on a case by case basis.

4.6.2.3 Heat Loss Uncertainty

Heat loss from the enclosure walls to the atmosphere is calculated via

$$Q_{loss} = A_w \frac{\Delta T}{R_{ins}} = A_w \frac{\left(T_i - T_o\right)}{R_{ins}} \tag{4.14}$$

where:

Q_{loss} = heat loss from the hot/cold walls, W

A_w = wall area, m^2

T_i , T_o = temperature on Styrofoam layer sides, ^oC

R_{ins} = Styrofoam insulation thermal resistance =2.6148 m^2.K/W

The temperature difference was measured using thermocouples attached to the opposite sides of the insulation layer. The uncertainty of the heat loss can be estimated as

$$e_{Qloss} = \pm\sqrt{\left(\frac{\partial Q_{loss}}{\partial T_1} e_{T1}\right)^2 + \left(\frac{\partial Q_{loss}}{\partial T_2} e_{T2}\right)^2}$$

$$e_{Qloss} = \pm\sqrt{\left(\frac{A_w}{R_{ins}} e_{T1}\right)^2 + \left(\frac{A_w}{R_{ins}} e_{T2}\right)^2} = \pm\frac{A_w}{R_{ins}} e_{TC}\sqrt{2} \qquad (4.15)$$

where, e_{TC} = Thermocouple wire uncertainty = 0.122 ^oC

The heat loss uncertainty for the different enclosure walls can be estimated by substituting the different wall areas into equation 4.15;

for the hot and cold walls, $e_{Qloss\_h/c,}$, ($A_{h/c}$ = 0.413 m^2)

$$e_{Qloss\_h/c} = \pm 0.027 \text{ W} \qquad (4.16)$$

for the side walls, $e_{Qloss\text{-}side}$, (A_{side} = 0.40 m^2)

$$e_{Qloss\_side} = 0.0264 \text{ W} \qquad (4.17)$$

Thus, the back loss uncertainty for the hot and cold walls is 0.027 Watt

and for the top and bottom of the enclosure, $e_{Qloss\text{-}t/b}$, ($A_{t/b}$ =0.636 m^2) is given by

$$e_{Qloss\_t/b} = 0.042 \text{ W} \qquad (4.18)$$

4.6.2.4 Surface to Surface Radiation

Surface to surface radiation estimation is necessary for convection heat transfer calculation from the hot and cold walls. Radiation heat transfer is calculated using the direct radiation method given in equation 4.19:

$$Q_{h/c-rad} = A_{h/c}\sigma\varepsilon\sum_{J=1}^{5} F_{ij}(T_i^4 - T_j^4) \tag{4.19}$$

where:
$Q_{h/c-rad}$ = radiation heat transfer from hot/cold walls, W
$A_{h/c}$ = hot/cold walls area = 0.41 m^2
σ = Stefan-Boltzman constant = 5.67 e –8 $W/m^2.K^4$
ε = surface emisssivity = 0.9 for Plexiglas
F_{ij} = view factor between surfaces i and j
T_i = surface i temperature (K)
T_j = surface j temperature (K)

The view factors between surfaces were determined using the relation offered for three-dimensional geometries in Incropera and Dewitt (1996). The view factor between the hot and cold walls was calculated using:

$$F_{ij} = \frac{2}{\pi\overline{X}\overline{Y}}\left\{\ln\left[\frac{\left(1+\overline{X}^2\right)\left(1+\overline{Y}^2\right)}{1+\overline{X}^2+\overline{Y}^2}\right]^{1/2} + \overline{X}\left(1+\overline{Y}^2\right)^{1/2}\tan^{-1}\frac{\overline{X}}{\left(1+\overline{Y}^2\right)^{1/2}} + \overline{Y}\left(1+\overline{X}^2\right)^{1/2}\tan^{-1}\frac{\overline{Y}}{\left(1+\overline{X}^2\right)^{1/2}} - \overline{X}\tan^{-1}\overline{X} - \overline{Y}\tan^{-1}\overline{Y}\right\} \tag{4.20}$$

where:
$\overline{X} = X/L$, $\overline{Y} = Y/L$

figure 4.10 shows the i and j references used in 4.20.

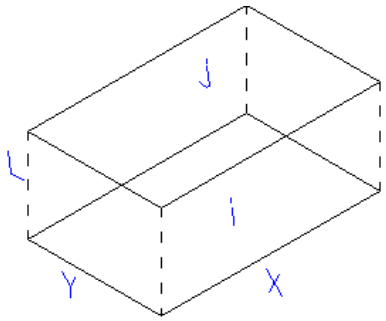

Figure 4.10: Hot-Cold View Factor Dimensions

On the other hand, the view factor between the hot/cold walls and the side/top walls was calculated using

$$F_{ij} = \frac{1}{\pi W}\left(\begin{array}{l} W\tan^{-1}\frac{1}{W} + H\tan^{-1}\frac{1}{H} - (H^2+W^2)^{1/2}\tan^{-1}\frac{1}{(H^2+W^2)^{1/2}} \\ \quad + \frac{1}{4}\ln\left\{ \frac{(1+W^2)(1+H^2)}{1+W^2+H^2}\left[\frac{W^2(1+H^2+W^2)}{(1+W^2)(W^2+H^2)}\right]^{W^2} \times \right. \\ \left. \left[\frac{H^2(1+H^2+W^2)}{(1+H^2)(W^2+H^2)}\right]^{H^2} \right\} \end{array} \right) \qquad (4.21)$$

where: H = Z/X, W = Y/X

Figure 4.11 shows the geometry required to apply 4.18.

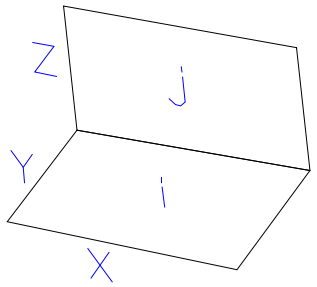

Figure 4.11: Hot/Cold-Side/Top View Factor Dimensions

The emissivity of the Plexiglas has the value of 0.9. The surface temperatures were measured as follows: the hot/cold temperatures were the average of four thermocouple wires mounted on each surface. The floor temperature is the average of two thermocouple wires mounted on the floor. The top and side temperatures are measured using thermocouple wires installed on the outer side of the Plexiglas for both walls. The thermocouple wires are placed in ¼" deep grooves and fixed with high conductivity thermal epoxy. The top temperature is the average of two thermocouple wires. While the side temperature is measured using one thermocouple wire placed at the center of the wall. The temperature measured by the thermocouple wires placed on the outside of the

Plexiglas is assumed to be representative to the wall temperature. This assumption seems reasonable, since measurements are taken after the enclosure reaches steady state. Also, the thermocouple wires are placed in a groove and fixed with high conductivity thermal paste. Similarity is assumed for determining the front side temperature, i.e. the temperature of the front side is assumed to be equal to the temperature measured for the back side of the enclosure.

The uncertainty associated with the radiation from the i^{th} surface to the j^{th} surface can be estimated by

$$e_{Qij} = \pm A_i \sigma \varepsilon F_{ij} \sqrt{\left(4T_i^3 . e_{Ti}\right)^2 + \left(4T_j^3 . e_{Tj}\right)^2} \tag{4.22}$$

The total radiation uncertainty of surface i is the summation of the uncertainty resultant from all surface radiation terms added in quadrature

$$e_{Qi-rad} = \pm \sqrt{\left(e_{Qi-1}\right)^2 + \left(e_{Qi-2}\right)^2 + \ldots + \left(e_{Qi-5}\right)^2} \tag{4.23}$$

4.6.3 Uncertainty in Convective Flux and Film Coefficients

4.6.3.1 Calculation of Convective Flux Uncertainty

The convective heat flux from the active walls is one of the main results for heat transfer experiments. It is used to calculate the convection coefficient and Nusselt number. The convective heat flux will be calculated for the hot and cold walls separately.

The hot wall convective heat transfer is calculated by

$$Q_{h\text{-}conv} = Q_{pwr} + Q_{h\text{-}rad} + Q_{h\text{-}loss} \tag{4.24}$$

where:
$Q_{h\text{-}conv}$ = hot wall convective heat flux, W

Q_{pwr} = Input electrical power to the hot wall, W
$Q_{h\text{-}rad}$ = hot wall surface radiation, W
$Q_{h\text{-}loss}$ = heat losses from the back of the hot wall, W

The uncertainty of the hot wall heat flux is estimated by applying 4.1 to the linear relation in 4.24.

$$e_{Qh-conv} = \sqrt{\left(\frac{\partial Q_{h-conv}}{\partial Q_{pwr}} e_{Qpwr}\right)^2 + \left(\frac{\partial Q_{h-conv}}{\partial Q_{h-rad}} e_{Qh-rad}\right)^2 + \left(\frac{\partial Q_{h-conv}}{\partial Q_{h-loss}} e_{Qh-loss}\right)^2}$$

$$e_{Qh-conv} = \sqrt{\left(e_{Qpwr}\right)^2 + \left(e_{Qh-rad}\right)^2 + \left(e_{Qh-loss}\right)^2} \tag{4.25}$$

The cold wall heat transfer coefficient, on the other hand, is calculated by:

$$Q_{c\text{-}conv} = Q_{out} + Q_{c\text{-}rad} + Q_{c\text{-}loss} \tag{4.26}$$

where:
$Q_{c\text{-}conv}$ = cold wall convective heat transfer, W
Q_{pwr} = output power of the cold wall panel, W
$Q_{h\text{-}rad}$ = cold wall surface radiation, W
$Q_{h\text{-}loss}$ = heat losses from the back of the cold wall, W

The uncertainty of the cold wall heat flux is estimated in a way similar to the hot wall heat flux as:

$$e_{Qc-conv} = \sqrt{\left(\frac{\partial Q_{c-conv}}{\partial Q_{out}} e_{Qpwr}\right)^2 + \left(\frac{\partial Q_{c-conv}}{\partial Q_{c-rad}} e_{Qh-rad}\right)^2 + \left(\frac{\partial Q_{c-conv}}{\partial Q_{c-loss}} e_{Qh-loss}\right)^2}$$

$$e_{Qc-conv} = \sqrt{\left(e_{Qoutr}\right)^2 + \left(e_{Qc-rad}\right)^2 + \left(e_{Qc-loss}\right)^2} \tag{4.27}$$

4.6.3.2 Calculation of Heat Convection Coefficient Uncertainty

The convection heat transfer coefficient is the main result of the heat transfer experiments. The heat convection coefficient is the final parameter calculated, thus its uncertainty depends on the uncertainties of the previous measurements and calculations.

The heat convection coefficient is calculated only for the isothermal hot and cold walls. It depends mainly on the convection heat transfer from the wall, $Q_{w\text{-}conv}$. The heat convection coefficient of an isothermal wall is calculated as

$$h = \frac{Q_{w-conv}}{A_w (T_w - T_{ref})} = \frac{Q_{w-conv}}{A_w \Delta T_{w-ref}} \tag{4.26}$$

where:
h = heat transfer coefficient, $W/m^2.K$
$Q_{w\text{-}conv}$ = convection heat transfer, W
A_w = wall area, m^2 ($A_h = A_c = 0.41\ m^2$)
$\Delta T_{w\text{-}ref}$ = temperature difference between wall and a reference, ^oC
T_w = wall surface temperature, ^oC
T_{ref} = reference temperature, ^oC

The uncertainty associated with the convection coefficient is calculated using equation 4.1.

$$e_h = \sqrt{\left(\frac{\partial h}{\partial Q_{w-conv}} e_{Qw-conv}\right)^2 + \left(\frac{\partial h}{\partial \Delta T_{w-ref}} e_{\Delta Tw-ref}\right)^2}$$

$$e_h = \frac{1}{A_w \Delta T_{w-ref}^2} \sqrt{\left(\Delta T_{w-ref} e_{Qw-conv}\right)^2 + \left(Q_{w-conv} e_{\Delta Tw-ref}\right)^2} \tag{4.27}$$

4.7 Summary

The experimental facility design was detailed in this chapter. The facility construction material and instrumentation were also listed and discussed. The facility

design took into consideration the experiments that will be conducted on the facility, i.e. heat transfer and PIV experiments.

A scaling fluid suitable for natural convection experiments was discussed. The requirements of the successful scaling fluid were given. A scaling fluid was suggested after comparison among several scaling fluid candidates. The selection was based upon the ability of the fluid to match the full-scale enclosure's Rayleigh number. The cost and availability of the scaling fluid were also taken into consideration.

Finally, the uncertainty analysis of the measurements and calculated quantities of the heat transfer experiment was detailed. The uncertainty analysis was based on the method introduced by Kline and McClintock (1953). The Uncertainty of the heat transfer results will be calculated on a case-by-case basis as the experiments are conducted.

5. Natural Convection Experiments

Heat transfer experiments were conducted to validate facility design and performance. Steady state natural convection experiments were conducted in the facility with air as the working fluid. The performance of the facility will be examined by the uniformity of the isothermal wall temperatures, heat transfer results, and temperature profile inside the enclosure. Those parameters are the main parameters in natural convection experiments, so if these parameters are within acceptable limits, then the facility performance is considered satisfactory in this area.

Several tests were conducted over a limited range of Grashof number ($\sim 10^8$). The heat transfer results of those experiments were compared to the existing data in the literature in same Grashof number range.

Data was collected using the Fluke data loggers described in the previous chapter. The Fluke data loggers allow the user to specify the scanning interval only, i.e. one data point is retrieved every scanning interval. To overcome this back draw of the data logging systems, data was collected at a fast rate once steady state conditions were reached. The collected data was then averaged and the average value was used in the subsequent calculations. A minimum of 100 data points was collected for each steady state case at a scanning interval of 10 seconds. Arithmetic averaging of the collected data was used in the heat balance calculations, the temperature profile representation and the heat transfer coefficients calculation.

5.1 Calculations

The major outcomes of the natural convection test are the heat transfer coefficient and its dimensionless counterpart, the Nusselt number. The heat transfer coefficient and Nusselt number for the hot and cold walls are calculated using

$$\bar{h}_w = \frac{Q_{w-conv}}{A_w (T_w - T_{ref})} \tag{5.1}$$

$$\overline{Nu}_w = \frac{\bar{h}_w . H_w}{k_{air}} \tag{5.2}$$

where,
$\bar{h}_w$ = wall heat transfer coefficient, W/m^2.K
$Q_{w\text{-}conv}$ = wall convection heat transfer, W
A_w = wall area, m^2
T_w, T_{ref} = wall and reference temperatures, respectively, ^oC
$\overline{Nu}_w$ = wall Nusselt number
H_w = height of the wall, m
k_{air} = air thermal conductivity, W/m.K

For the hot wall, the convection heat transfer, $Q_{h\text{-}conv}$, is calculated as:

$$Q_{h\text{-}conv} = Q_{in} - Q_{loss} - Q_{rad} \tag{5.3}$$

while for the cold wall, $Q_{c\text{-}conv}$, is calculated using

$$Q_{c\text{-}conv} = Q_{out} + Q_{loss} + Q_{rad} \tag{5.4}$$

The heat imbalance of the facility is an important metric for assessing performance. It is calculated by adding the heating panel electrical power, the cooling panel heat transfer rate, and the estimated insulation heat loss from the enclosure sides.

$$Q_{imbal} = Q_{in} + Q_{out} + Q_{loss} \tag{5.5}$$

$$\% Q_{imbal} = 100*Q_{imbal} / Q_{in} \quad (5.6)$$

where,
Q_{imbal} = imbalance heat transfer of the facility, W
Q_{in} = electrical power to the hot wall, W
Q_{out} = heat transfer rate from the cold wall, W
Q_{loss} = heat loss rate from the insulation, W
$\%Q_{imbal}$ = heat imbalance ratio, %

As can be seen from equation 5.1, the heat transfer coefficient depends on the choice of the reference temperature. Two reference temperatures are reported in the literature for such experiments, the cold wall temperature and the air temperature. In this chapter, the Nusselt number (Nu), the heat transfer coefficient (h) and Grashof number (Gr) will be calculated using both reference temperatures. An asterisk '*' will be used when the mean air temperature ($T_m = 0.5*(T_h + T_c)$) is used. The uncertainty analysis will be conducted for the experimental results as shown in chapter 4.

5.2 Experimental Results and Discussion

Three steady state natural convection experiments were conducted to validate the facility performance. The facility was considered to be at steady state if the change in the isothermal wall temperature was less than 0.1 ^{o}C/hr. The facility was allowed to run for more time after this condition was met. The average time the experimental facility was run for each test was about 30 hrs. Figure 5.1 illustrates steady state operation of the facility.

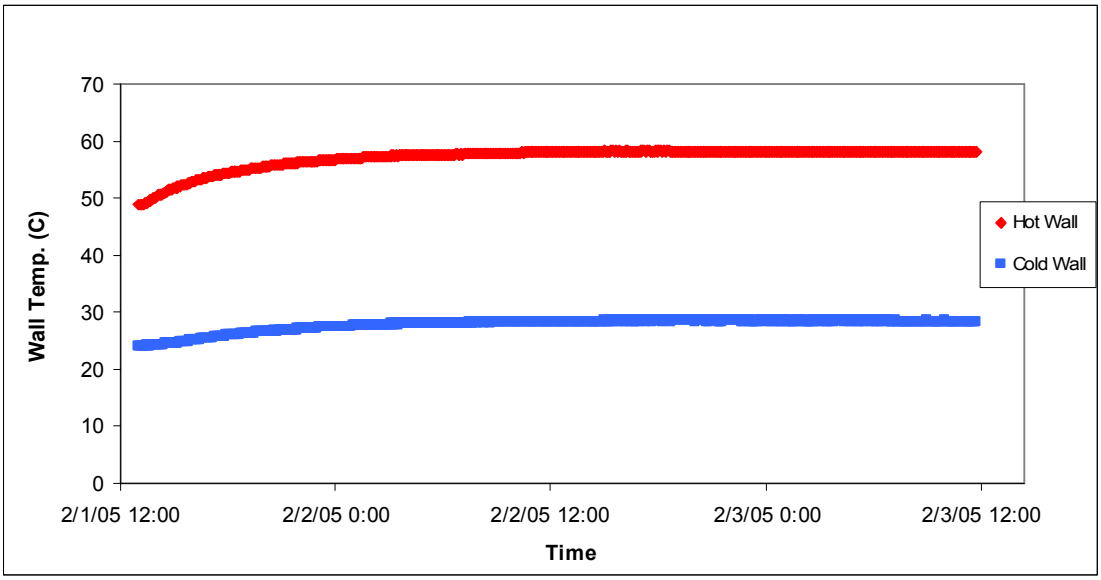

Figure 5.1: Hot and Cold Walls Temperatures, Gr* = 1.87 e +8

The isothermal walls temperatures were uniform to an acceptable degree. The hot wall thermocouple deviation from the average temperature was less than $\pm 1^{o}C$. The cold wall, on the other hand, was uniform to within $\pm 1.5^{o}C$ from the average temperature. The larger deviation of the cold wall is due to the limited number of ethylene glycol passes in the cooling panel attached to the wall. Figure 5.2 shows the temperature deviation in both walls. This non uniformity of the cold wall temperature shows the need for redesigning the cold wall panel to reduce this deviation. Adding more passes through the panel, and reducing the pipe diameter should improve its performance and reduce this deviation. Another way is by using a water-cooled jacket instead of the cold wall panel, this should give a better heat transfer rate, and more uniform wall temperature. The cold wall non uniformity can be improved by making he cooling panel an integral part of the enclosure.

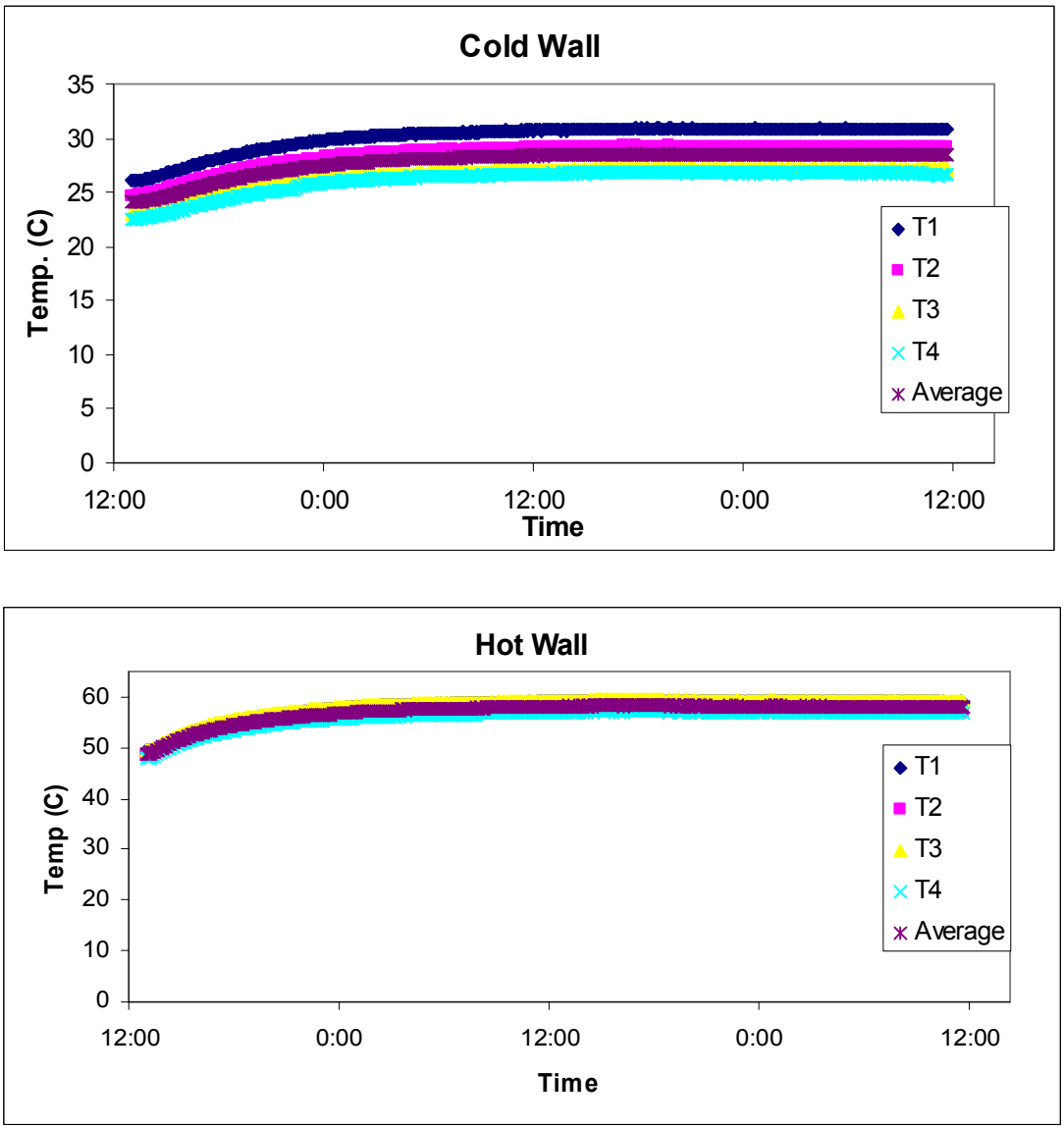

Figure 5.2: Cold and Hot Walls Temperature Variation, Gr* = 1.87 e +8

The input power to the hot wall heating panel was measured using the watt transducer described in chapter 4. A variac was used to control the input voltage to the heating panel and thus control the input power. Nevertheless, the input voltage to the heating panel was fluctuating and caused the input power to fluctuate within a limited range. Figure 5.3 shows a sample of this fluctuation for the case of $Gr^* = 1.87 \times 10^8$, note that for this the variation is within ± 1.5 W of the average. This fluctuation is small

relative to the input power average, less than 1.5% for this case. Thus, the input power is considered constant throughout the experiment. In order to eliminate the effect of those fluctuations the input power value used for heat transfer calculations was the average of at least 100 readings recorded at a scanning interval of 10 seconds. Since an average value was used in the calculations, the input power fluctuations were not considered the uncertainty analysis. A clean power source should be used for future experiments to reduce input power fluctuations.

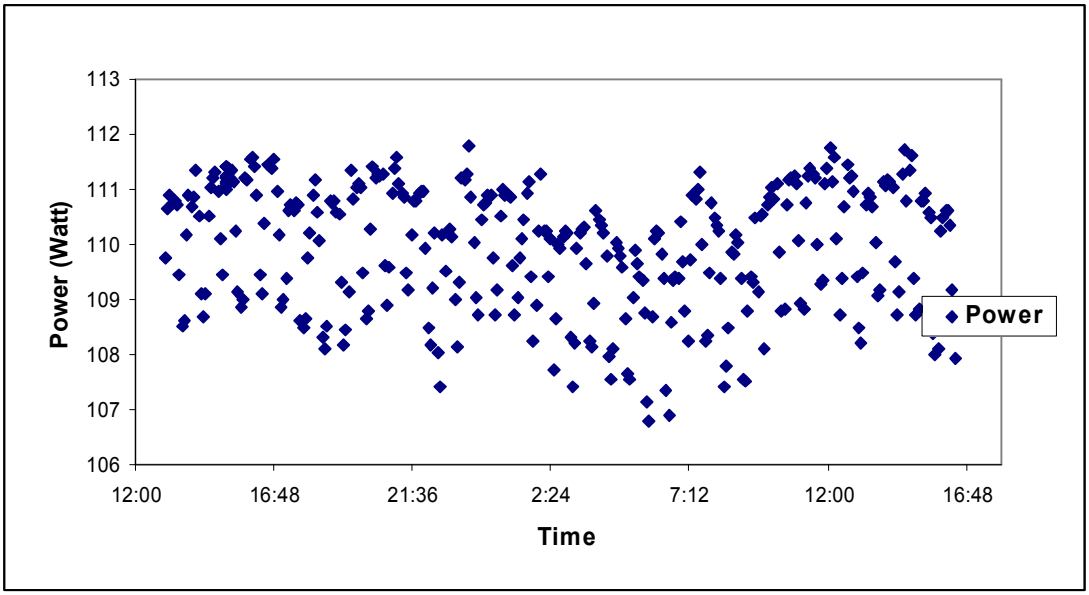

Figure 5.3: Input Power Fluctuations, Gr* = 1.87 e +8

Table 5.1 shows the heat balance results obtained for the three steady state natural convection experiments conducted on the experimental facility. The table shows the values of Gr*, Input power (Q_{in}), chiller output power (Q_{out}), Heat loss through the insulation (Q_{loss}), heat balance error (Q_{imbal}), heat error ratio ($\%Q_{imbal}$) and the heat balance uncertainty.

Table 5.1: Heat Balance Results for Natural Convection Experiments

Gr*	T_h-T_c	Q_{in}	Q_{out}	Q_{loss}	Q_{imbal}	$\%Q_{imbal}/Q_{in}$	$\%e_{Qimbal}$
	C	W	W	W	W		
1.87E+08	29.82	110.10	86.41	13.62	10.07	9.12	12.36
1.57E+08	24.92	82.76	67.78	9.20	5.78	6.97	16.45
1.24E+08	19.76	57.57	46.25	4.28	7.04	12.20	23.65

The range of Gr* (= $g\beta(T_h - T_m)\ H^3/\nu^2$) presented in table 5.1 is limited as stated earlier. Although the temperature difference between the hot and cold walls ranged from 16.7 to 29.8 ^oC, the Gr* was limited to the 10^8 range. This is due to the linear effect of the temperature difference on the value of Gr* (= $g\ \beta\ \Delta T\ H^3/\nu^2$). The temperature difference has a limited effect of temperature Gr*. To significantly change the value of Gr* the best parameter to change would be the height of the enclosure, H.

The heat imbalance of the zone stayed within 15% as shown in table 5.1. This value is within the uncertainty limit of the heat balance calculations. The high uncertainty in the lower Gr* cases is due to the small temperature difference across the cold wall panel. This uncertainty in the temperature difference across the cold panel is the dominating uncertainty in the experiments. The maximum temperature difference obtained was of order 1 ^oC and the measurement uncertainty is 0.22 ^oC as estimated in the previous chapter.

Table 5.2 shows the calculated parameters for the hot wall steady state convection experiments. Note how the choice of the reference temperature affects the Nusselt number and the convection coefficients. The value of the Nusselt number and the heat transfer coefficient were almost doubled by changing the reference temperature. The

estimated uncertainty was small in both cases and this is mainly due to the uncertainties associated with the input power and surface and air temperatures measurements.

Table 5.2: Hot Wall Heat Convection Results

Gr	h_hot	Nu_hot	$\%e_h$	Gr*	h*_hot	Nu*_hot	$\%e_{h^*}$
	W/m2.K				W/m2.K		
2.48E+08	3.42	65.80	3.99	1.87E+08	8.94	167.61	4.68
2.10E+08	3.54	68.18	4.28	1.57E+08	7.94	152.88	4.64
3.13E+08	3.97	76.44	2.80	1.24E+08	6.84	131.59	3.05

The heat transfer results associated with the cold wall are shown in table 5.3. The value of the heat transfer coefficient and Nusselt number are less than those for the hot wall, this because the convection heat transfer of the cold wall is less than that of the hot wall. Theoretically, if there are no heat losses from the experimental facility and no experimental errors in the measurements, the input convection heat transfer into and out of the experimental facility at steady state conditions, should be the same, which means equal Nusselt and heat convection coefficients. But in real experiments heat losses and measurements uncertainty always exist. The uncertainty associated with the cold wall is much larger than that of the hot wall. This is mainly due to the uncertainty of the Ethylene Glycol temperature difference measurement. The non uniformity in the cold wall temperature did not play a role in the calculations since the average wall temperature was used in the heat transfer calculations. The Ethylene Glycol temperature difference measurement is an important factor in determining the convection heat transfer from the cold wall required for the calculation of the heat convection coefficient, as explained in the previous chapter. The uncertainty of the temperature measurement difference was 0.22 ^{o}C, while the maximum temperature difference across the cooling panel was of order 1 ^{o}C. Thus, the uncertainty of the temperature difference measurement was about 22%,

which became the dominating factor in the cold wall heat transfer uncertainty calculations.

Table 5.3: Cold Wall Heat Convection Results

Gr	h-cold	Nu-cold	$\%e_h$	Gr*	h*-cold	Nu*-cold	$\%e_{h^*}$
	W/m2.K				W/m2.K		
3.75E+08	3.79	70.97	29.26	1.87E+08	7.57	141.95	29.27
3.13E+08	3.41	65.66	38.82	1.57E+08	6.82	131.32	38.84
2.48E+08	2.53	48.67	58.08	1.24E+08	5.06	97.35	58.09

Figure 5.4 shows a plot of Nu* vs. Gr* of the experimental results obtained. Note the difference of the uncertainty associated with the cold and hot walls. Also note the trend of increasing Nu* value as Gr* increases, although a clear trend is not available due to the limited number of points.

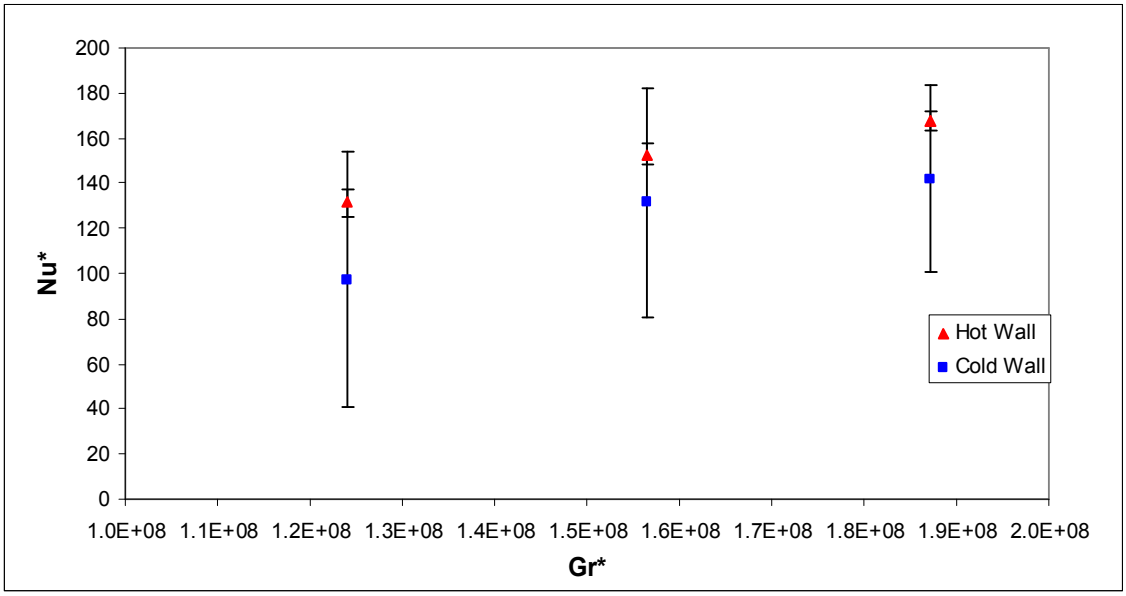

Figure 5.4: Hot and Cold Wall Heat Transfer, Nu* vs. Gr*.

The results obtained in this experiment were compared to the published data for natural convection. Figure 5.5 shows Nu* obtained for the hot and cold walls of this experiment (Elyyan_hot and Elyyan_cold) and the other data from the literature. The data obtained from the literature are local Nusselt and Grashof numbers. The data from the

literature was collected, arranged and presented by Weixiu Kong, a PhD student at Oklahoma State University.

The results obtained in this experiment are higher than that reported in the literature for the same range of Gr*. This difference is a result of the difference of the operating conditions of the data collected from the literature for comparison. For example, the data from Cheeswright and Zial (1986) is for tall enclosures (H/L >1). Also, Chen and Eichhorn (1976) data is for natural convection of a vertical plate in a stratified medium. Bohn and Anderson (1986) used water as the working fluid. These parameters participated in this difference seen in figure 5.5 between the data collected here and the literature data. In addition, the data obtained from the literature are local Grashof and Nusselt number. The local Grashof and Nusselt numbers are defined as;

$$Gr_x = \frac{g\beta(T_x - T_a)x^3}{\upsilon^2} \tag{5.7a}$$

$$Nu_x = \frac{\left(q''_x/(T_x - T_a)\right)x}{k} \tag{5.7b}$$

where; x: is the distance along the wall

While the average Nusselt number was defined in 5.2. The relation between the average and local Nusselt numbers is given as;

$$\overline{Nu} = \frac{1}{H}\int_0^H Nu_x\, dx \tag{5.8}$$

The average Nusselt number includes the effect of the temperature difference along the wall, while for local it is the difference at a single point.

Incropera and Dewitt (1996) in their analysis of laminar free convection on a vertical surface show that the value of the average Nusselt number is higher than that of the local Nusselt number ($\overline{Nu}_L = \frac{4}{3} Nu_x$). Extrapolating this to our case of internal turbulent natural convection flow within enclosures, we can see that our results compare are acceptable in comparison to the published data.

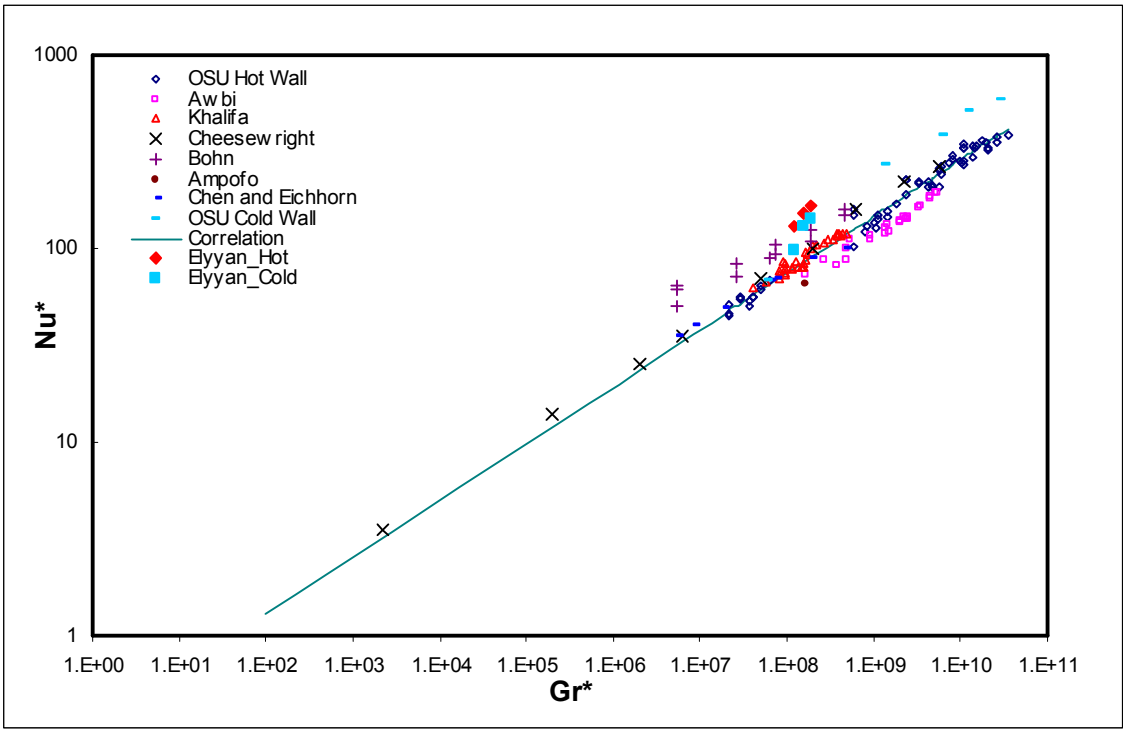

Figure 5.5: Natural Convection Results Comparison with the Literature

5.3 Temperature Profile

The thermocouple grid described in chapter 4 was used to measure the air temperature inside the enclosure. Temperature measurements were conducted at three different planes of the enclosure by moving the thermocouple grid inside the enclosure. After the enclosure reached steady state, at least 100 readings were recorded for each

measurement plane at a scanning interval of 10 seconds. When the thermocouple grid was moved to a new plane, the flow field was left for about 15 minutes to allow it to return to steady state.

Temperature measurements were conducted at three different planes; Z/W = 0.25, 0.5 and 0.75 (where Z is the longitudinal position of the thermocouple grid and W is the width of the enclosure = 0.813 m). The temperature profile at those different planes will be used to check the temperature pattern inside the flow field.

Figures 5.6 – 5.8 show the vertical temperature profile of selected columns of the thermocouple grid at different locations inside the enclosure. The dimensionless height Y/H of the thermocouple wire is plotted against the dimensionless temperature θ ($\theta = (T-T_c)/(T_h-Tc)$). The thermal boundary layer of the flow is not shown in the figures, this is because near wall the thermocouples were outside the thermal boundary layer.

The vertical temperatur profiles shown in figures 5.6 – 5.8 show the temperature distribution at the core of the enclosure and close to the boundaries at Z/W = 0.25, 0.5 and 0.75, respectively. Obvious similarity of the temperature profiles at the different planes for the same X/L exists. Strong similarity occurs between the Z/W = 0.25 and Z/W = 0.5 planes, and there is a little difference between the temperature profiles for Z/W = 0.75. The largest difference occurs at X/L = 0.5 mainly at the boundaries near the top and floor. This might be due to some fluctuations in the flow field caused by the thermocouple grid that did not damp down after the waiting period. Nevertheless, the temperature profile at X/L = 0.04 and 0.96 is very similar to the other planes.

The apparent similarity of the vertical temperature profiles at the different planes leads us to conclude that the temperature field inside the enclosure is two dimensional.

This conclusion agrees with the findings of previous researchers, Olson et al. (1990) and Hsieh and Wang (1994) for low aspect ratio enclosures and verifies the two dimensional basis of the natural convection scale analysis.

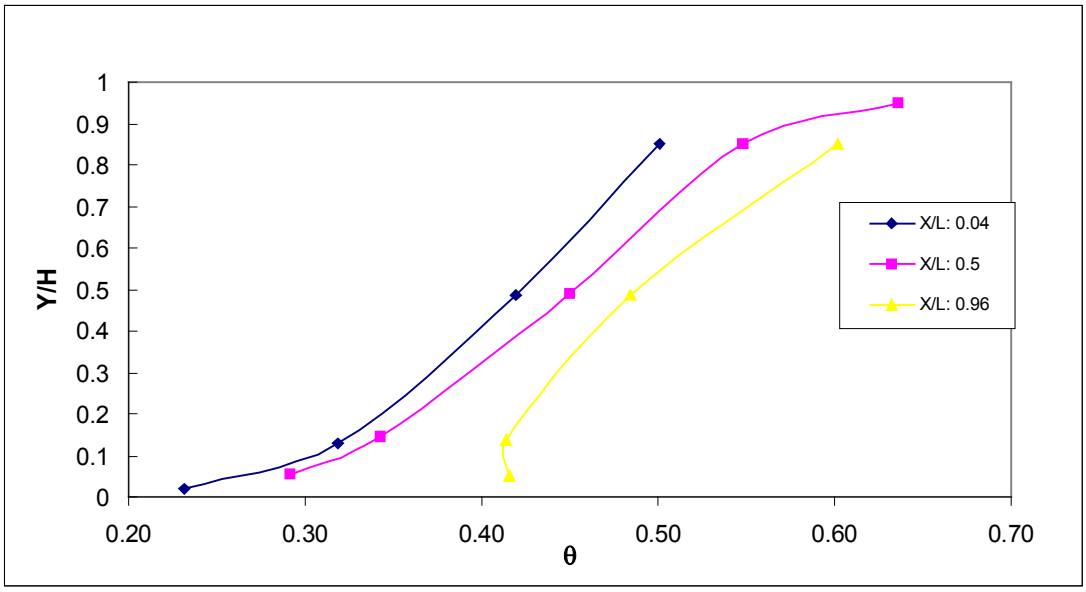

Figure 5.6: Vertical Temperature Profiles, Z/W = 0.25, Gr* =1. 57 e+8 at X/L = 0.04 (near Cold Wall), at X/L = 0.5, and at X/L = 0.96

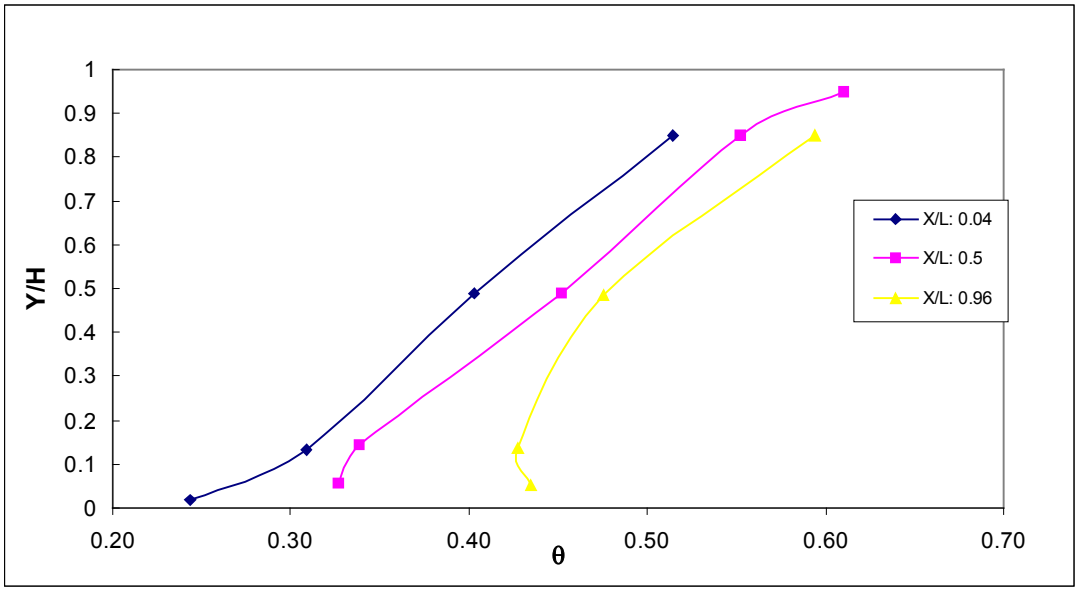

Figure 5.7: Vertical Temperature Profiles, Z/W = 0.5 Gr* =1.57 e+8.

at X/L = 0.04 (near Cold Wall), at X/L = 0.5, and at X/L = 0.96

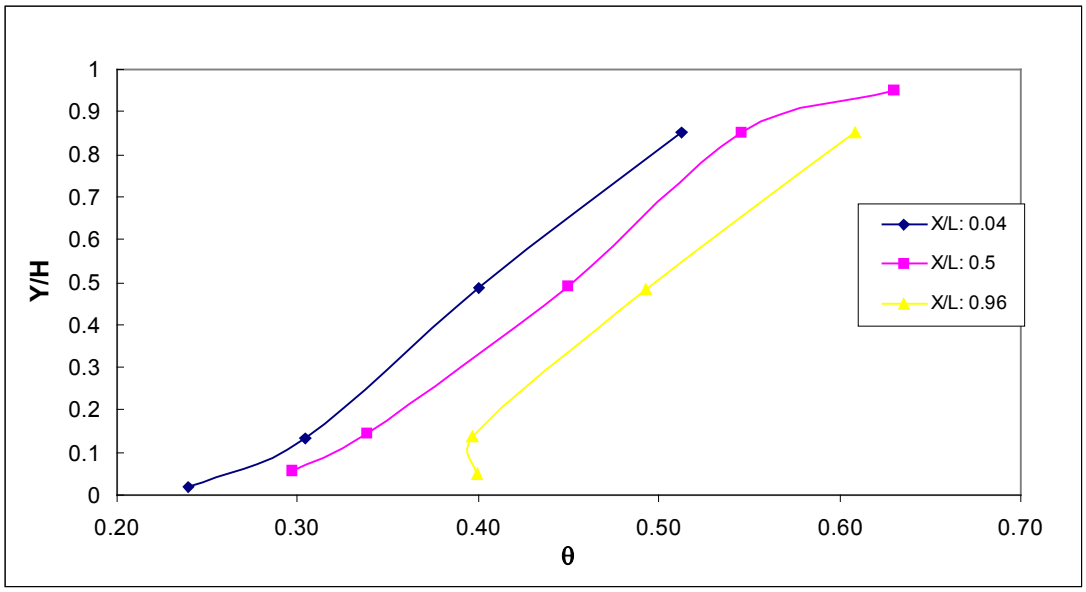

Figure 5.8: Vertical Temperature Profiles, Z/W = 0.75 Gr* =1.75 e+8.

at X/L = 0.04 (near Cold Wall), at X/L = 0.5, and at X/L = 0.96

Also, it can be seen from figures 5.6 – 5.8 that the temperature inside the core is linearly stratified, the only exception are the points close the walls, which means close to the boundary layer. This result again agrees with the previous findings of Olson et al. (1990) and Hsieh and Wang (1994) for low aspect ratio enclosures.

5.4 Conclusions

Natural convection experiments were successfully conducted with the experimental facility. The results compared well with the heat transfer data available in the literature, although the uncertainty in the cooling panel heat transfer rate was unacceptably high.

The temperature measurement of the air inside the enclosure showed that the temperature profile inside the enclosure was two dimensional. Also, temperature measurement showed that the core of the enclosure is linearly stratified.

6. Flow Visualization

The need of an accurate flow visualization technique has been highlighted earlier in this thesis. Most of the flow visualization techniques reported in the literature are smoke visualization methods, which have high uncertainties associated with them and do not quantitatively analyze the flow field inside the enclosure. Accurate measurement of the velocity flow field inside the enclosure is required. In this chapter the flow visualization of the flow field inside the enclosure will be conducted. Two techniques will be used to visualize the flow, the regular smoke visualization and the PIV technique. The PIV usage is the most significant part in this chapter, its components and settings will be discussed in detail here.

The PIV technique discussed here will serve as a reference for future work, since no PIV work has been done before on this type of flow, to the best knowledge of this author. Most of flow visualization conducted, even those who used laser and digital cameras, did not give accurate quantitative analysis of the flow velocity. We will try here to show the capability of the PIV technique of analyzing the current flow field accurately.

Smoke visualization is the most widely used method for natural convection flow visualization. Smoke visualization has been normally used to qualitatively assess the flow field inside an enclosure. Velocity measurement using this technique is difficult and has a high experimental uncertainty. Particle Image Velocimetry (PIV), on the other hand, is a relatively accurate technique for flow field velocity measurement and gives a very

detailed description of the flow field. But this technique requires specialized skill in its application.

Although this chapter will discuss both visualization techniques, smoke visualization will be described briefly since it has been done before. The PIV technique on the other hand will be described in more detail since this is a new application for PIV measurements.

6.1 Smoke Visualization

Smoke visualization is used to qualitatively evaluate the flow field inside the enclosure. In this section a brief description of the technique and the results will be given, since it is only intended to give a qualitative description of the flow field and confirm the two dimensional nature of the flow shown in the temperature measurements.

6.2.1 Experimental Setup and Procedure

Burning incense sticks were hung from the top of the enclosure near the cold wall to generate the smoke required for this flow visualization technique. A five mega-pixel digital camera was used to take pictures of the flow field visualized by the smoke.

A strong diffuse light was found to be the most appropriate light source for visualizing the flow inside the enclosure. A diffuse light source was required to avoid light reflections from the enclosure's walls. The enclosure was illuminated from the top, with the light diffusively reflected into the enclosure.

The top and front walls insulations were of necessity removed for the whole experimental procedure and setup. Thus, the heat balance was lost for this part of the experiment. Nevertheless, the hot and cold walls temperatures did not change drastically;

the temperature change was about 2 degrees. Actually, the temperature difference between the walls was $\Delta T = 19.36\ ^{o}C$ ($T_h = 40.96\ ^{o}C$, $T_c = 21.6\ ^{o}C$). This means that the Grashof number ($Gr^* = 2.71x10^8$, $Ra^* = 3.27x10^8$) was the same order of magnitude as the Gr* for the heat transfer experiments.

6.1.2 Experimental Results and Discussion

The pictures taken for the flow field inside the enclosure show a distinct two dimensional flow with thin boundary layers next to the isothermal walls and a stratified core. Figure 6.1 shows the flow field inside the empty enclosure as shown using smoke visualization.

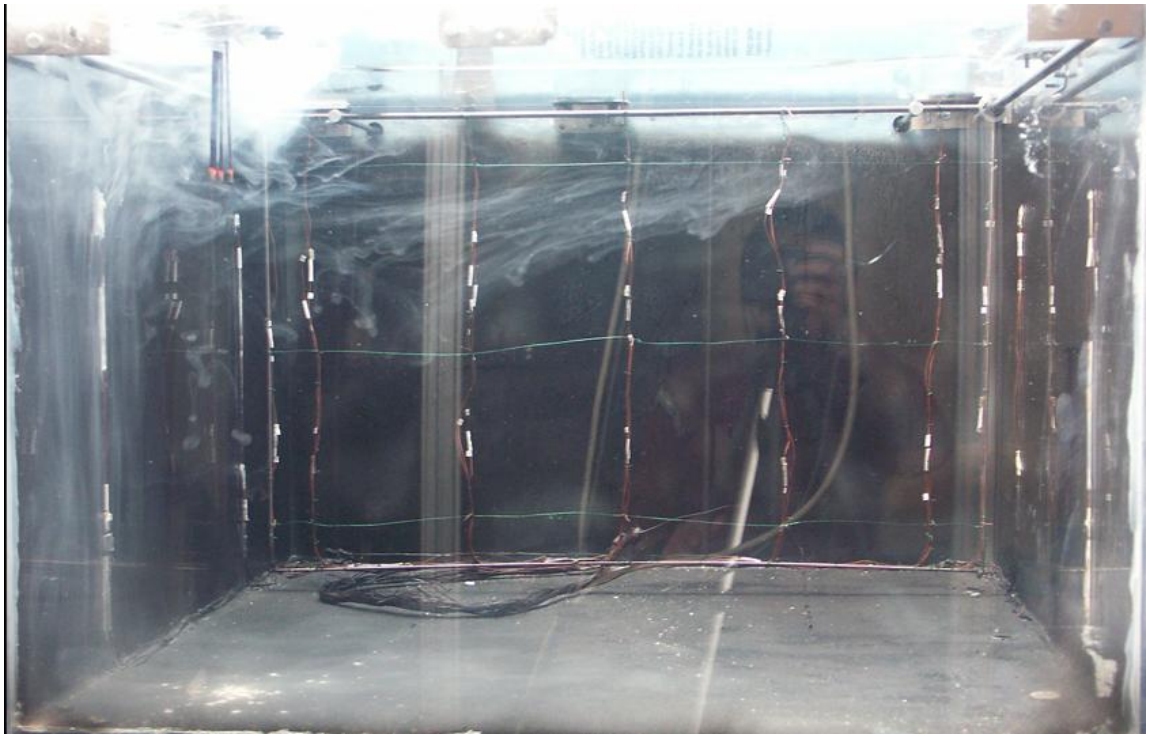

Figure 6.1: Flow Pattern Using Smoke Visualization for Empty Enclosure, $Gr^* = 2.71x10^8$

In order to analyze the flow field, a video camera was used to record the flow pattern inside the enclosure. The recorded images show the smoke descending along the cold

wall in a thin wall jets with some turbulent eddies at its edge, turning along the bottom and rising along the hot wall. As the flow turned from the hot and cold walls to the top and bottom wall jets became thicker. No smoke motion was detected in the core.

This flow pattern agrees with the results obtained in the literature, Olson et al. (1990) and Hsieh and Wang (1994). It also is consistent with the results obtained from the heat transfer experiments of the enclosure. The stationary core agrees with the conclusion of the existence of a thermally stratified enclosure. Significantly, the eversing loops along the top or bottom of the enclosure reported by Olson et al. (1990) could not be detected by the smoke visualization technique.

6.2 PIV Visualization

Particle Image Velocimetry (PIV) is a velocity measuring technique that measures the motion of small, seeded (or marked) regions of a fluid by recording and analyzing images of the marker at two or more times (Adrian, 1991). PIV is a very efficient way to instantaneously measure the flow field inside the enclosure. The PIV system consists of a laser light source, seeding particles, one or two digital cameras and a processor to analyze the recorded images. The cameras are usually positioned in a plane perpendicular to the laser light sheet.

Two dimensional PIV measurements were conducted for the flow field inside the enclosure. The following sections discuss the experimental setup and parameters for the PIV system.

6.2.1 Seeding Material

PIV resolves velocity is by measuring the displacement of small seeding particles that follow the flow field. The choice of the seeding particles for flow visualization is one of the main challenges in PIV and can be case specific, i.e. it depends on the specific flow parameters and experimental setup used. Melling (1997) conducted a thorough study of seeding particles for PIV measurements. He discussed the light scattering characteristics and the aerodynamic tracking capability of typical seeding particles. The tracking capabilities of the seeding particles are influenced by the particle shape, particle diameter d_p, particle density ρ_p, fluid density ρ_f and fluid dynamic viscosity μ_f (Melling, 1997). Small, naturally buoyant seeding particles are the most suitable tracking materials.

Seeding liquid flows is much easier than gas flows due to the wide range of seeding materials that have comparable densities and the availability of larger particles, Melling (1997) says "The generation of scattering particles for liquid flows is almost trivial, since it is seldom necessary to do more than mix particles in powder form or as a suspension into the flow". On the other hand, seeding gas flows is not a trivial task. Liquid droplets or solid particles can be used to seed gas flows. The number of particles per interrogation area should be about 15 particles in order to achieve an accurate velocity measurement (Keane and Adrian 1990b). Melling (1997) recommends a seeding particle diameter of ~ 1 μm to achieve the best flow field tracking, especially for turbulent flows.

Different seeding materials have been used for gas flows including TiO_2 with particle size, d_p, < 1 μm, Al_2O_3 with $d_p = 0.7 - 1$ μm, Polycrystalline with $d_p = 30$ μm and olive oil with $d_p = 1.06$ μm. Most of the particles used have sizes on the order of 1 μm, this is the most suitable size for turbulent flow tracking (Melling, 1997).

Olive oil was selected for this application based on its cost, availability, and the availability of a droplets generator. Although the density ratio of olive oil to that of air is not the perfect density ratio recommended by Melling (density ratio = 808 ≠ 1) it is lighter than other seeding particles, e.g. TiO_2 (3500 kg/m^3). In addition, olive oil has an acceptable refractive index (= 1.46). Also, the olive oil droplets will be generated at a size of 1 – 3 μm, which is perfect for following the flow field inside the enclosure.

A six nozzle atomizer manufactured by TSI Inc. was used for oil droplet generation. The atomizer produces oil droplets with a nominal size of 1-3 μm, which is suitable for PIV applications.

6.2.2 PIV Experimental Setup

The PIV system used in this experiment is a TSI Inc. system. The light source consists of two Nd:Yag lasers packaged together as the model Gemini 200 mini dual Nd:Yag from New Wave Research. Each laser produces a maximum power of 200 mJ at a wavelength of 532 nm with a pulse width of 3 – 5 ns.

Images are recorded using PowerView CCD (Coupled Charged Devices) camera model number 630150. The CCD camera used has a resolution of 4 MP (2Kx2K) and a pixel size of 7.4x7.4 μm, with an output of 8 bits at maximum rate of 17 frames/sec. The lens accompanying the camera is a 50mm, 1:1.40 Nikon AF Nikkor lens.

The laser source and the CCD camera are synchronized using the Laser Pulse Synchronizer model 610034 manufactured by TSI Inc. The synchronizer function is to control the firing of the laser source and camera frame capturing.

A highly flexible laser light arm is used to position the laser beam as required by the user. The laser light arm has the ability to rotate 360^{o} at each knuckle and can be extended to a height of 1.8 m. The light arm is a TSI Inc. product, model no. 1098915.

Optical lenses at the exit of the laser light arm are used to form the laser sheet from the laser beam. The laser sheet illuminates the required area of the flow field. The correct combination of cylindrical and spherical lenses needs to be used in order to produce the appropriate light sheet with the correct height and thickness at the imaging area. Cylindrical lenses are used to convert the beam into a laser sheet, while a spherical lens is used to control its waist. The smaller the laser sheet waist, the more intense it is, which in turn helps producing a higher signal to noise ratio. On the other hand, a thin laser sheet may cause measurement problems due to out of plane motion of the seeding particles. Thus, the out of plane motion of the seeding particles is an important parameter that needs to be taken into consideration when determining the different parameters of the PIV system. Wide laser sheets are desirable, but care must be taken to achieve uniform light intensity over the covered area. For our experiments the combination of a cylindrical lens with a focal length of –15 mm and a spherical lens with a focal length of 1000 mm were used. This produced a laser sheet 1.5 mm thick and 75 cm wide.

The laser source and the light arm base were placed on a rigid base that was fixed to a movable table. The movable table was equipped with air cushions to reduce base vibration that might disturb the system. This table provided the system with extra flexibility and enabled measurements at different elevations.

A traversing mechanism was constructed to move the camera and the laser arm head in the vertical direction. In order to fix the horizontal distance between the CCD camera

and the laser sheet source they were moved as a single unit. This made the PIV system operation much easier since the cameras, where it was calibrated only once at the beginning of the test. The experimental setup is shown in figure 6.2.

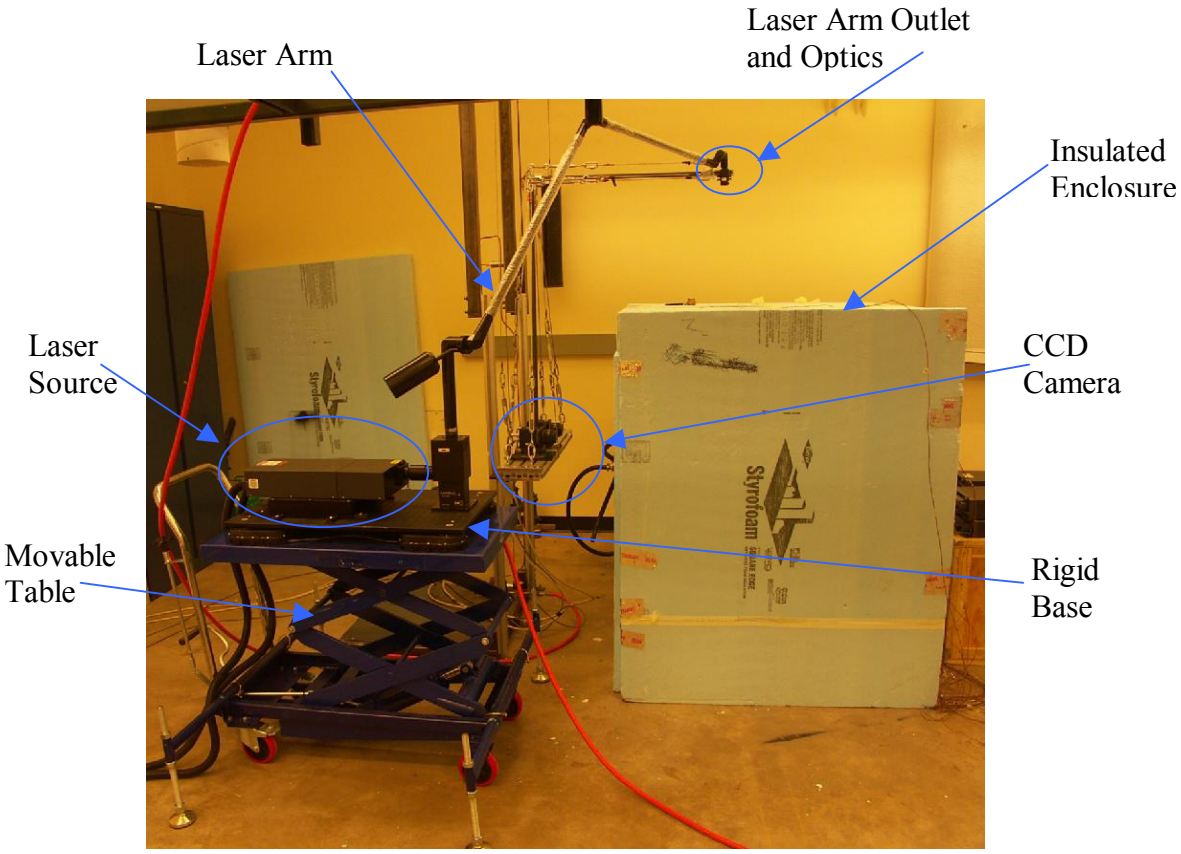

Figure 6.2: PIV Experimental Setup

The oil atomizer used in this experiment uses pressurized air to atomize the oil. This means that the atomized oil droplets will be at high velocity and pressure leaving the atomizer. Since introducing the atomized oil droplets into the enclosure will significantly disturb the flow field the oil droplet delivering system was modified to minimize this effect.

The atomizer outlet diameter was reduced in order to add some pressure drop to the system, and thus reduce the flow rate of the air/oil stream. The stream was then expanded to reduce the velocity of the particles entering the enclosure. The flow was seeded by a short puff of air/oil mixture followed by a period of 30 – 45 minutes, during which time no additional particles were introduced and the flow field was allowed to reconstruct.

6.2.3 PIV Calibration

PIV calibration is not a trivial task; it requires patience and caution since it can be dangerous. As mentioned earlier, the PIV system consists of several component; the laser source, the laser arm, the optical lenses and the CCD camera. Those components need to be well calibrated with respect to each other. Recalibration is required any time the laser is moved or one of the critical dimensions are disturbed

PIV Calibration starts at the laser source. The laser source of our system is a mini dual laser. Those two lasers need to be well aligned, i.e. the output beam of both lasers should follow the same path. Once the laser source is internally aligned, the laser arm base needs to be aligned with the laser source. Using the fine adjustment of the internal mirrors at the base of the laser arm the laser sheet output of the laser arm is adjusted to the correct shape. Laser calibration and alignment is the first, most important and dangerous step in the whole calibration process.

The second step after aligning the laser components is calibrating the CCD camera with the laser sheet. The camera is placed in a plane perpendicular to the laser sheet plane. In summary, the CCD camera is calibrated for 2-D measurements by focusing the camera on a target placed in the plane of the laser sheet. Precision machinists' metal ruler was used to calibrate the camera. Calibration images are then captured using the Insight 6

software and calibration parameters are calculated and saved by the program. The saved calibration images and parameters are used for image processing.

6.2.4 PIV Parameters

The performance of PIV depends upon the mean concentration of seeding particles, the velocity variations within the measurement volume, the thickness of the light sheet, the laser pulse separation time, and the size and shape of the interrogation spot (Keane and Adrian, 1990a). Those parameters depend in turn on the lens magnification, M, the camera lens f-number, and the laser wavelength, λ.

The lens magnification of the system is defined as

$$M = \frac{d_i}{d_o} \tag{6.1}$$

where:
d_i = the distance from the image plane to the lens, m
d_o = the distance from light sheet to the lens, m

The distance between the camera lens and the laser sheet was set to 71.12 cm; this distance was chosen to make it possible to visualize most of the flow inside the enclosure (W = 0.813 cm). The CCD camera has a length of 7 cm, width 7 cm, and a height of 7.62 cm. The front of the camera was 2.86 cm from the lens. The Nikon lens optical lens is 3.81 cm length. Assuming that the CCD array is placed at the middle of the CCD camera, the distance from the image plane to the lens is ~ 7.1 cm. The calculated magnification of the PIV system is then 0.1.

The f-number, $f^{\#}$, of the lens determines the depth of field where the camera is focused. The f-number can be calculated by equation 6.2 (Adrian, 1991)

$$f^{\#} = 0.25 \frac{(\delta z/\lambda)^{1/2}}{1 + M^{-1}} \tag{6.2}$$

where:
δz = the laser sheet thickness, μm
λ = the wavelength of the light, μm

The wavelength of the Nd:Yag laser is 532 nm, while the thickness of the laser sheet after calibration was about 1.5 mm. Using those quantities and the previous magnification we find that an $f^{\#} = 1.2$ is optimal.. $f^{\#}$ selection also depends on the experimental conditions such as wall reflections and seeding. Thus it is sometimes changed to get the best images of the flow field. For this experiment the $f^{\#}$ used was 4, this $f^{\#}$ was found to give the clearest images of the flow field.

6.2.5 Image Capturing and Processing

Images were captured using the frame straddle technique. In this technique two images are captured. The first laser is pulsed towards the end of the first frame, and the second laser is pulsed towards the beginning of the second frame of the camera. Figure 6.3 shows the frame straddling mode-timing diagram. Note that the first laser pulse needs to be delayed due to delays in the system, and to make sure the first pulse occurs towards the end of frame 1. The pulse delay and pulse separation time can be adjusted using Insight 6.

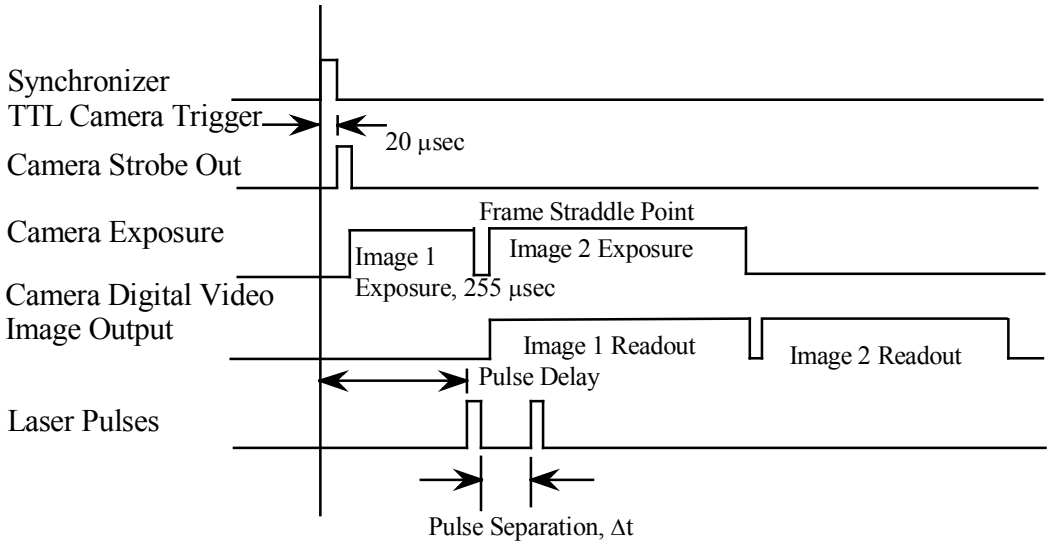

Figure 6.3: Frame Straddling Mode Timing Diagram (PIV Operation Manual, 2004)

Pulse separation time is an important parameter in PIV measurements, since it is used in the calculation of the fluid velocity, as shown in equation 6.3

$$U_x = \Delta x/\Delta t \text{ and } U_y = \Delta y/\Delta t \quad (\text{as } \Delta t \longrightarrow 0) \tag{6.3}$$

where;
U_x U_y = seeding particle velocity components, m/s
Δx = seeding particles displacement, m
Δt = pulse time separation, sec

The pulse separation time, Δt, is the single most important adjustable variable in a PIV system, as it determines the maximum and minimum velocities that can be measured (Adrian, 1991). Kean and Adrian (1990b) recommend that the in plane particle displacement should be less than 0.25 of the interrogation spot size and that the out of plane displacement should not be more than 0.25 of the light sheet thickness. Higher values of the in and out of plane particle displacement will cause errors in the velocity vector calculation due to the loss of the seeding particles in the second frame.

Some prior knowledge of the flow field will help determining the most suitable grid size, pulse delay, and pulse separation. The most appropriate pulse time separation can be estimated using the guidelines given above as

$$M|u_{max}|\ \Delta t/d_I \leq 0.25 \text{ and } w\ \Delta t/\Delta z \leq 0.25 \quad (6.4)$$

where;
M = lens magnification
u_{max} = maximum velocity of the fluid
Δt = pulse separation
d_I = Interrogation spot diameter
w = out of plane fluid velocity
Δz = laser sheet thickness

After the images are captured and digitized we can process these to obtain the required flow field. Insight 6 was used to process the captured images of the flow. Image processing consists of several steps: grid generation, spot masking, correlation and peak location and validation. Those steps will be explained in the following sections

6.2.5.1 Grid Generation

Grid generation is the first step in image processing. A Grid Engine is used to break the image into small areas, called interrogation spots. The interrogation spots are rectangular spots whose size is a variable that depends on the flow field characteristics. The interrogation spot size must be selected in compliance with the recommendations stated by Keane and Adrian (1990b) for the in and out of plane particle displacement. Also, Keane and Adrian (1990b) recommend that the number of seeding particles should be > 10 - 20 in each interrogation spot to ensure excellent detection probability.

Obviously, large interrogation areas would satisfy those conditions. But with larger spot sizes we will get less resolution of the vector field. Also, larger spot size makes it

harder for the correlation engine to find the correct displacement the particles between the two images. Thus, the interrogation spot size will be a compromise between the required resolution and the number of seeding particles in the spot.

The loss of particles due to in plane motion can be avoided or reduced by interrogation window offset (Gui et al, 2001). This offset has the advantage of increasing the number of paired particle images while decreasing the number of unpaired particle images. This minimization of the in plane loss of pair increases the signal to noise ratio, and hence improves detection (Raffel et al., 1998). Another way to eliminate the effect of loss of pairs due to in plane motion is by performing cross correlation between the images in a small interrogation spot first, and then refining a second interrogation spot (Adrian, 1991). Thus, the choice of the grid technique will depend mainly on the velocity gradient across the interrogation window and the number of seeding particles.

Insight 6 offers several Grid Engines options: the Nyquist grid, Recursive Nyquist grid, and Rectangular grid. The Nyquist grid gives 50% spot overlap between spot A and spot B. In Nyquist grid the image is processed once, and no window offset is allowed.

The Recursive Nyquist, on the other hand, processes the images in more than one pass. In the first pass a 50% overlap similar to the Nyquist grid is used. The results from this pass are used to determine the optimal window offset for the next pass. The Recursive Nyquist grid allows specifying smaller window dimensions for the second image pass, which will result in higher resolution of the vector field. The Recursive Nyquist might result in more accurate results, but it is more computationally expensive than the Nyquist grid.

The Rectangular grid provides more user grid parameters than the Recursive Nyquist or the Nyquist. It has the same processing principle as the Recursive Nyquist, but in this method the user can specify the overlap percentage used in the first pass and the grid size reduction used in the second pass. The Nyquist grid engine was used to generate the shown in the chapter.

6.2.5.2 Interrogation Window Masking

Window masking is used to increase the signal to noise ratio, and thus reduce the evaluation biases of the correlation engines (Gui et al, 2001). Insight offers three options for window masking, No Mask, ZeroPad Mask and Gaussian Mask. The No Mask option does not change anything in the interrogation spot. The ZeroPad Mask limits displacements larger than 0.5 of the spot size, but such displacements will not yield additional advantage if maximum displacement of 0.25 of the spot size is used. Gaussian Mask option modifies the interrogation spot by making the central pixels brighter and the edge pixels darker. The Gaussian window mask reduces the large gradient of the evaluation bias near zero displacement (Gui et al., 2001). The No Mask technique was used for this experiment. A maximum displacement value of 0.125 of the spot size was selected to accommodate the low velocities in the enclosure.

6.2.5.3 Correlation Engine

The Correlation Engines computes the correlation function of the masked spot A and spot B returning the result as a correlation map. The correlation function is an algorithm that sums the particle image matches at all pixel displacements within the displacement range (Insight 6 Instruction Manual, 2004).

The correlation engine selects the highest matched pixel displacement as the peak and the rest as noise. Insight 6 gives the user the ability to specify the minimum signal to noise ratio. The minimum signal to noise ration specified for this experiment was 1.5.

Insight 6 provides three options for the correlation engine: the Hart correlator, the Fast Fourier Transform (FFT) correlator and the Direct correlator. Gui and Merzkirch (2000) reported that the FFT method is the most used method due to its speed. Thus, FFT was used in this experiment.

6.2.5.4 Peak Engine

The Peak Engine analyzes the correlation map created by the Correlation Engine and determines the location of the particle image displacement peak (Insight 6 User Manual, 2004). Two Peak Engines are available for use in Insight 6: the Gaussian Peak and the Bilinear Peak. The Gaussian Peak is the recommended Peak Engine for use with FFT method.

6.2.5.5 Insight Settings

Insight 6 processing settings are as follows; a grid size of 64x64 pixels was chosen with a maximum displacement limit of 8 pixels. This grid size proved to give good results with reasonable resolution compared to grid sizes of 32x32 and 128x128, as will be shown later. No masking was used in processing the results. This is due to the high computational time required when masking is used for processing. The FFT was the correlation engine used due to its speed. The Gaussian peak correlation is the default setting with FFT, and thus it was selected.

Insight 6 also allows the user to specify the minimum number of particles and the signal to noise ratio of the interrogation spot required for a velocity vector to pass. The defaults of 10 particles per interrogation spot, and a signal to noise ratio of 1.5 were chosen. The 10 particle images per interrogation window result in a high detection probability according to Keane and Adrian (1990a). Table 6.1 lists the settings used for PIV images processing using Insight.

Table 6.1: PIV Processing Settings

Grid Engine	Nyquist	**Grid Size (pixel)**	64x64
Mask Engine	No Mask	**SNR**	1.5
Correlation Engine	FFT	**max. Disp. (pixel)**	8
Peak Engine	Gaussian	**min. # of Particles**	10

6.2.6 PIV Results and Discussion

All the experiments were conducted at the same temperature difference between the hot and cold walls, $\Delta T = 19.36\ ^{o}C$ ($T_h = 40.96\ ^{o}C$, $T_c = 21.6\ ^{o}C$), with Grashof number, $Gr^* = 2.71 \times 10^8$ ($Ra^* = 3.27 \times 10^8$), which is the same as the smoke visualization technique. A Heat balance was not achieved during the PIV visualization, as was the case for smoke visualization. This is due to the losses from the top and front sides of the enclosure, where the insulation was removed to enable visualization. Although, heat balance was not achieved the Grashof number changed very little. As a result the flow pattern visualized here is a good representation of the flow field.

Seeding the flow field using atomized olive oil with the described technique as previously described proved successful. The flow field was seeded uniformly, and the settling time of the oil droplets (about 2 hours) was long enough to take good pictures of the flow field. To further prove that the olive oil droplets were a good choice for seeding the flow, we will check the settling velocity of the droplets. The range of the oil droplets

diameters is 1 – 3 μm, so we will find the settling velocity for both extremes. The settling velocity of the droplets, assuming spherical shapes, can be calculated as;

$$V_s = \left[\frac{8}{3} \frac{g}{C_D} \frac{\rho_{oil}}{\rho_{air}} r \right]^{1/2} \tag{6.5}$$

Where:
V_s = particle settling velocity, m/s
g = gravitational acceleration, m/s^2
C_D = drag coefficient
ρ_{oil} = oil density, kg/m^3
ρ_{air} = air density, kg/m^3
r = oil droplet radius, m

The settling velocities of the oil droplets is therefore of the range, 0.0019 – 0.003 m/s. This settling velocity range will be compared with the velocity range measured inside the enclosure to check the suitability of the olive oil droplets.

The importance and selection of the pulse time separation was stated earlier along with the recommendations of Keane and Adrian (1990b). Several trials showed that the best results were obtained at a pulse time separation of (Δt = 6000 μsec). The pulse delay did not affect the results, since its function was to delay laser 1 towards the end of the frame1 capture as shown in figure 6.2. A pulse delay of 0.2 - 0.3 msec was found to be sufficient for this experiment. The frequency of image recording was 7.5 Hz.

6.2.6.1 PIV Settings Verification

Before proceeding to the PIV results obtained using the settings listed earlier, a sensitivity test was conducted to verify that the PIV processing parameters chosen are optimum. Sensitivity testing will be conducted for the interrogation spot size, masking

technique and correlation engine. All the tests were conducted on the same sample image picked from the flow field.

Different interrogation spot sizes were tested to select the optimum spot size that will give us good flow field details at a reasonable computation time. Figure 6.4 shows the velocity vector field for four different interrogation spot sizes: 128x128, 64x64, 32x32, and 16x16 pixels. The image was process using the Nyquist grid engine, no mask, the FFT correlation engine and the Gaussian peak engine. From the figure the 128x128 spot size (figure 6.4: a) did not give enough flow details. The 64x64 spot size (figure 6.4: b) gave reasonable flow details, and did not require much more computation time than the 128x128 case. The 32x32 spot size (figure 6.4: c) improved the resolution over the 64x64 case but did not provide new information and required significant computation time. The 16x16 spot size failed to correctly resolve the flow field. Thus, from figure 6.4, the 64x64 spot size was selected for image processing from the flow details and computational time respects.

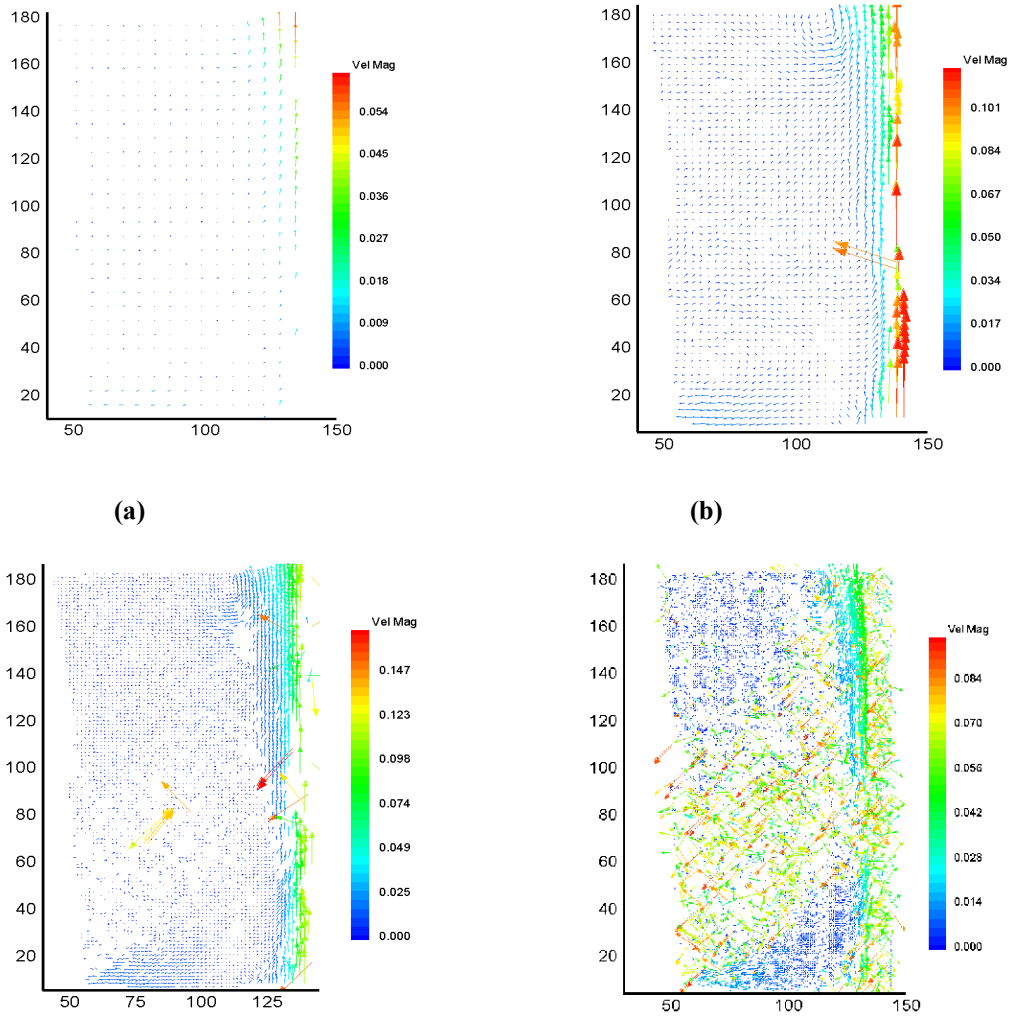

(a) **(b)**

(c) **(d)**

Figure 6.4: Interrogation Spot Size Dependency

(a) 128x128, (b) 64x64, (c) 32x32, (d) 16x16

The different correlation engines offered in Insight 6 were tested with an interrogation spot size of 64x64 with no mask engine used. The default peak engine offered for each correlation engine was selected. Figure 6.5 shows that the best flow field results were obtained with the Direct and the FFT correlation engines (figure 6.5: a and c). The flow fields resulting from both methods look similar, but the computation time

required for the Direct Correlator is much higher than for the FFT. Thus, the FFT correlation engine was selected for processing the PIV images in this experiment.

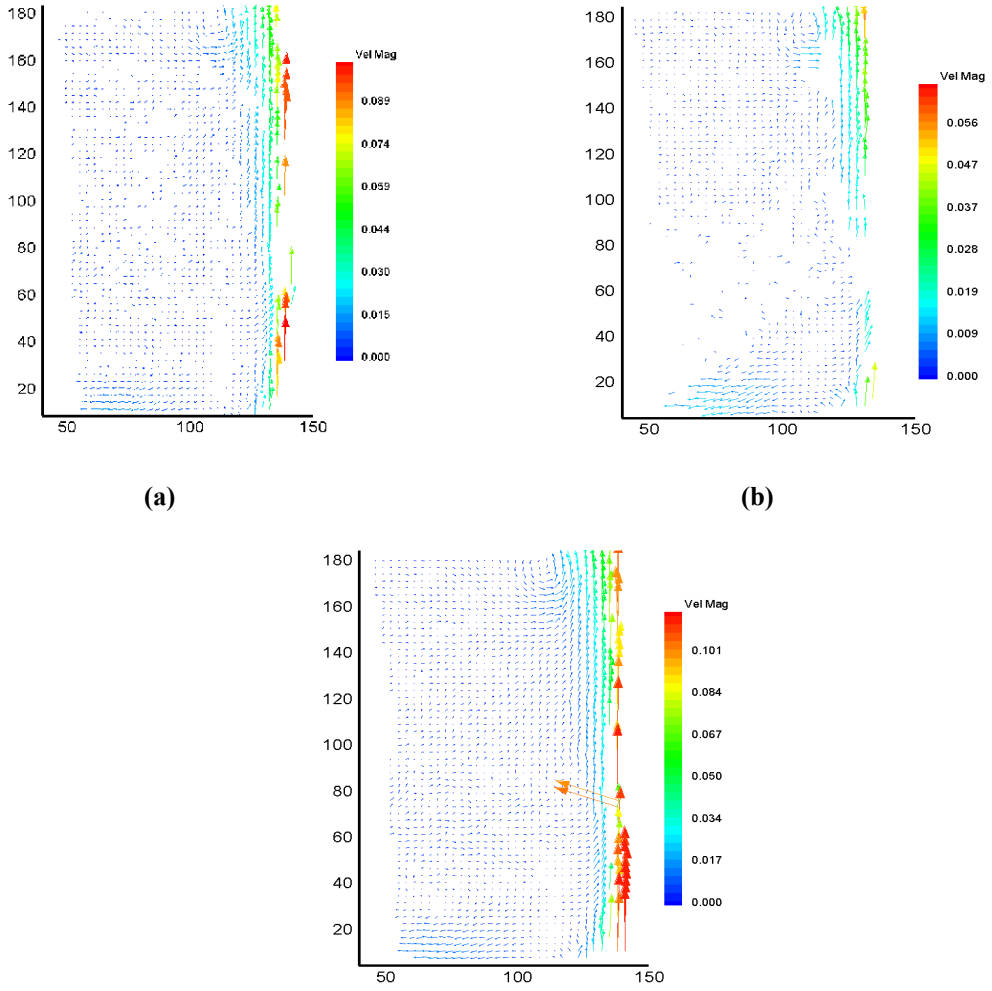

Figure 6.5: Correlation Engine Dependency

(a) Direct Correlator , (b) Hart Correlator, (c) FFT

Figure 6.6 shows the effect of the different masking engines on the flow field resolution. The grid size used was 64x64 with the FFT correlator and a Gaussian peak. The best results were obtained by using either the Gaussian mask engine or no mask (figure 6.6: a and c). Since the effect of applying the Gaussian mask increases the

computation time without significantly affecting the flow field images, no window mask will be applied.

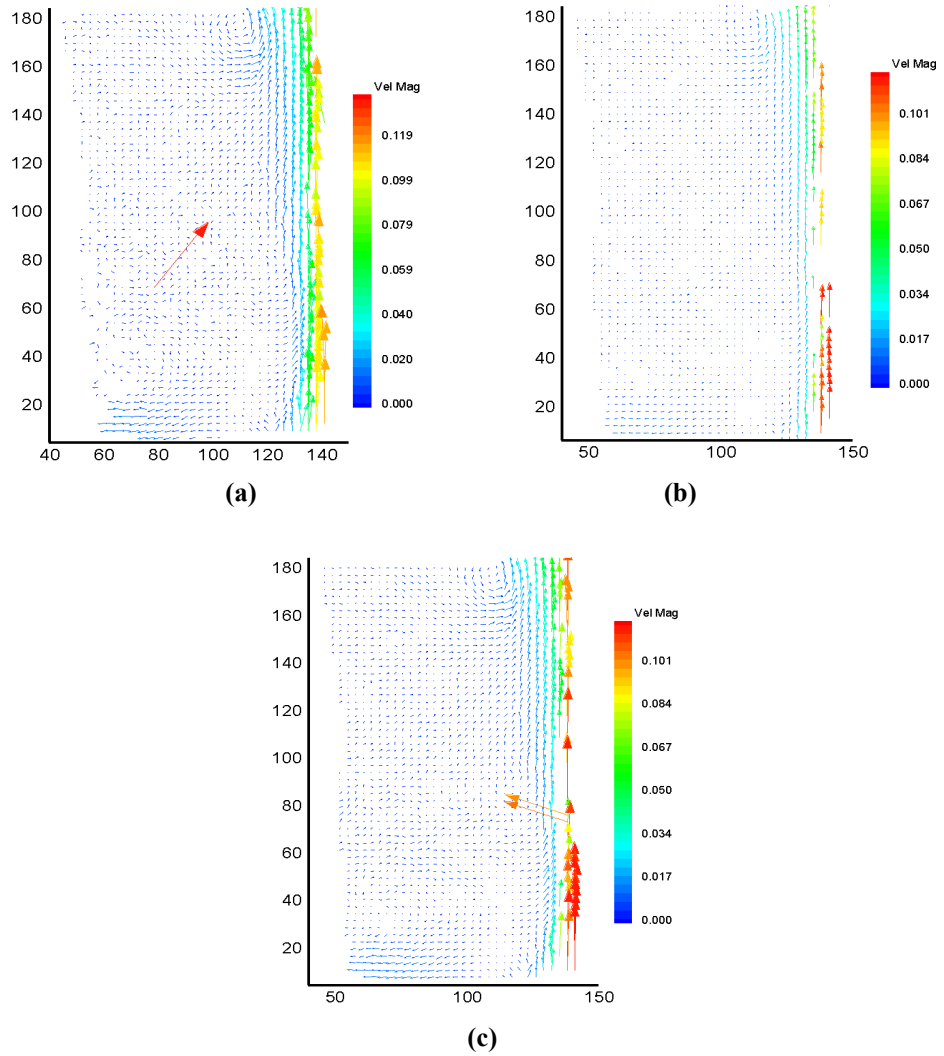

Figure 6.6: Mask Engine Dependency

(a) Gaussian Mask, (b) ZeroPad Mask, (c) No Mask

The error estimation of the PIV measurement is one of the challenges of its application (Huang et al, 1997). Huang et al. (1997) state that "error quantification is a function of the experimental conditions and the particle displacement detection algorithms used". The uncertainty of the PIV measurement cannot be estimated easily, it is a function of so many parameters that interact with each other. Adrian (1997) states

that “Typically, the velocity accuracy of PIV measurements is of order one percent, and the spatial resolution is of order one millimeter.” A detailed analysis of uncertainty is beyond the scope of this study. We will take the statement of Adrian (1997) as a witness on how accurate this technique is compared to smoke visualization, where the uncertainty can reach ~ 40% as was in the case of Olson et al. (1990).

6.2.6.2 Experimental Results and Discussion

The goal of the PIV visualization was to measure the velocity field, and get a clear view of the overall flow pattern inside the enclosure. Due to the limited view of the CCD camera view and the limitations imposed by the laser sheet power, the flow field was photographed piece by piece. PIV pictures were taken from the front of the enclosure, while the laser sheet was fired from the top. The measurement plane was divided into 15 sections, as shown in figure 6.7. The sections were overlapping at their edges.

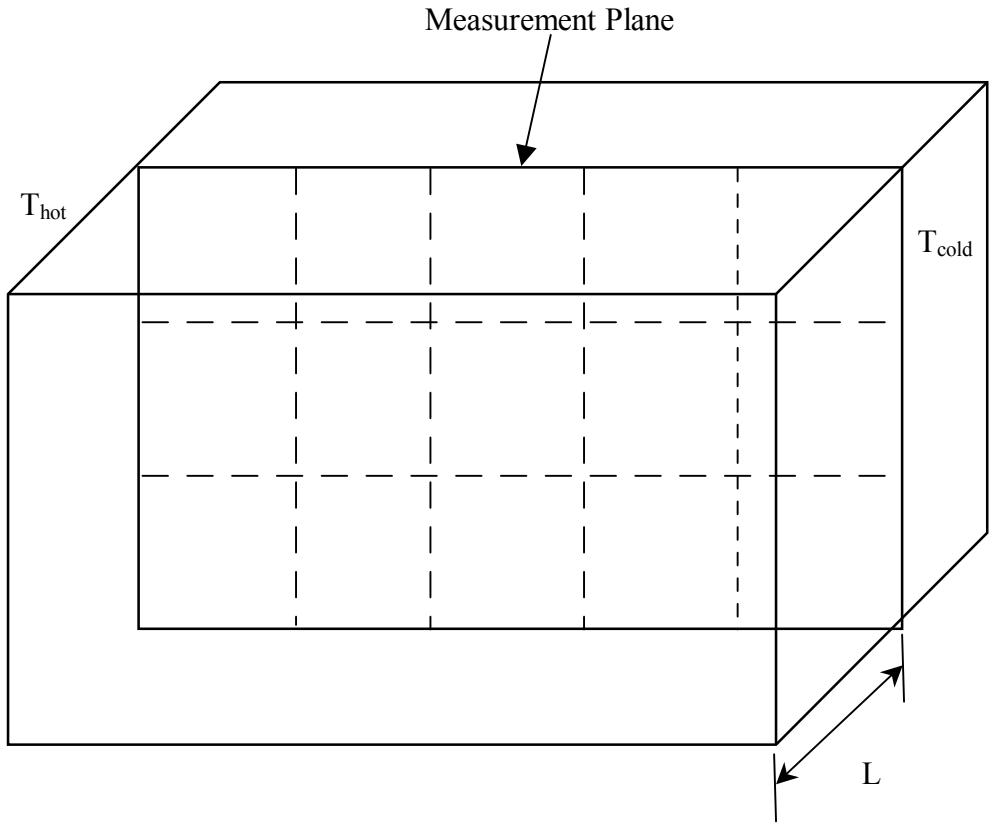

Figure 6.7: PIV Measurement Plane Sections

In order to get a representative flow field 100 images were taken for each section. These images were processed and validated using Insight 6, and then an average vector field was obtained using TecPlot 9.

The vector field produced from the image processing contains invalid velocity vectors referred to as outliers. The outliers result from three dimensional motion, large velocity gradients, improper seeding and so on (Huang et al, 1997). To eliminate the outliers, the vector field is validated. Insight 6 gives the user the ability to design his validation process. The validation process is intended to reject the velocity outliers and, if desired, fill in the regions in the flow field where the correlation engine was not able to resolve a valid velocity vector. Insight 6 fills these holes using the mean of the

surrounding vectors. The flow field can also be smoothed, but this will result in the loss of flow field details.

For this experiment, the raw velocity vectors initially found by processing the images are validated to reject any outliers. The criteria used for outlier rejection was the standard deviation, σ, of the measurements. A cutting edge of $\pm 3\sigma$ was used, this criterion was sufficient to reject the outliers and not delete valid vectors field.

The effect of filling the holes tended to produce unrealistic results as shown in figures 6.8 – 6.10. Figure 6.8 shows a raw velocity vector field resulting from Insight 6 before processing. The invalid velocity vectors are obvious. Figure 6.9 shows the same vector field after it has been validated to delete $\pm 3\sigma$ velocity vectors. Figure 6.10 shows how the holes that exist in the middle of the vector field would be filled using Insight 6. In some cases, the filled results are obviously erroneous, but in less obvious cases the filled results would still tend to create some doubt on the validity of the results. For this reason, validated, but unfilled results are presented with the filled results for the validation tests.

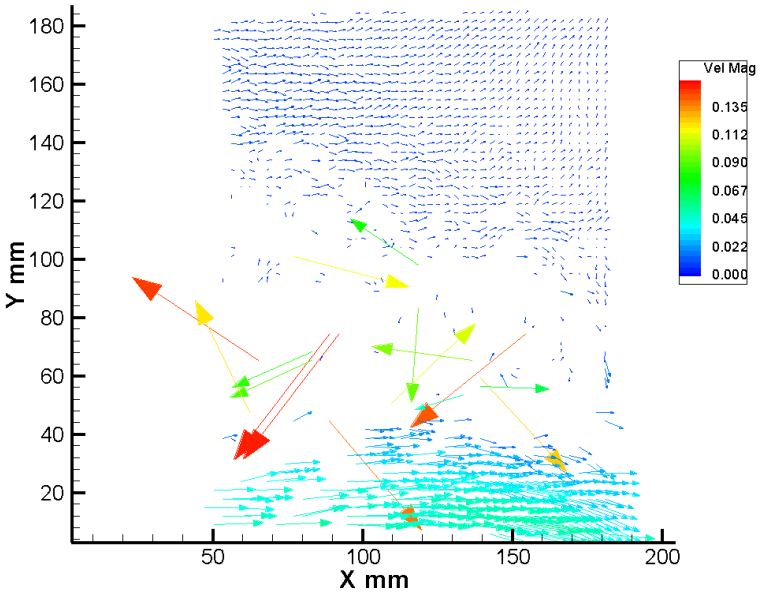

Figure 6.8: Pre Validation Velocity Vectors

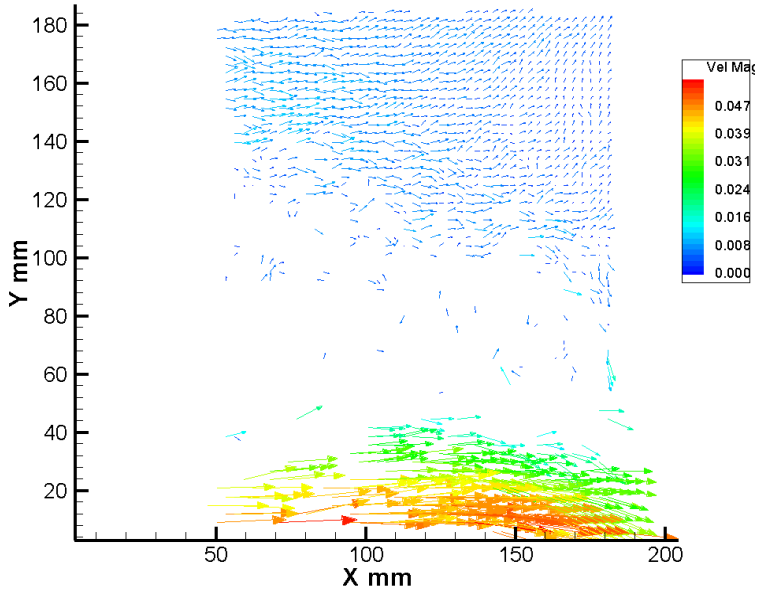

Figure 6.9: Validated Velocity Vectors with No Filling

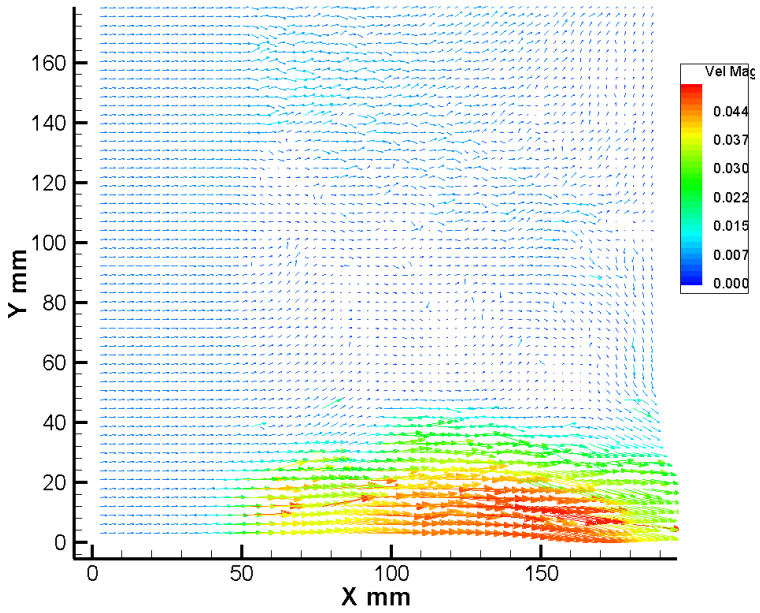

Figure 6.10: Validated and Filled Vector Field

Figure 6.11 shows the velocity vectors obtained at a plane 25.4 cm from the front panel of the enclosure. Insight was not used to fill the holes resulting from the processing. The flow pattern shown in figure 6.11 shows the air rising along the hot wall, flowing along the top, descending along the cold wall and flowing back to the hot wall along the bottom.

The areas with unresolved vectors occur mainly next to the walls, especially the hot and cold walls. This is due the reflection of the laser sheet from the wall, large velocity gradients and/or seeding problems at those spots. Also, note that along the top side there are three empty rectangles, at the hot and cold walls edges and in the middle of the top. In these locations, the aluminum corners used to assemble the enclosure obscured the view.

Figure 6.12 shows the filled velocity pattern for the same images. No major changes exist between the flow pattern in figure 6.11 and figure 6.12. The raw vector field

(validated to eliminate outliers only) shown in figure 6.11 will be referenced in the following sections.

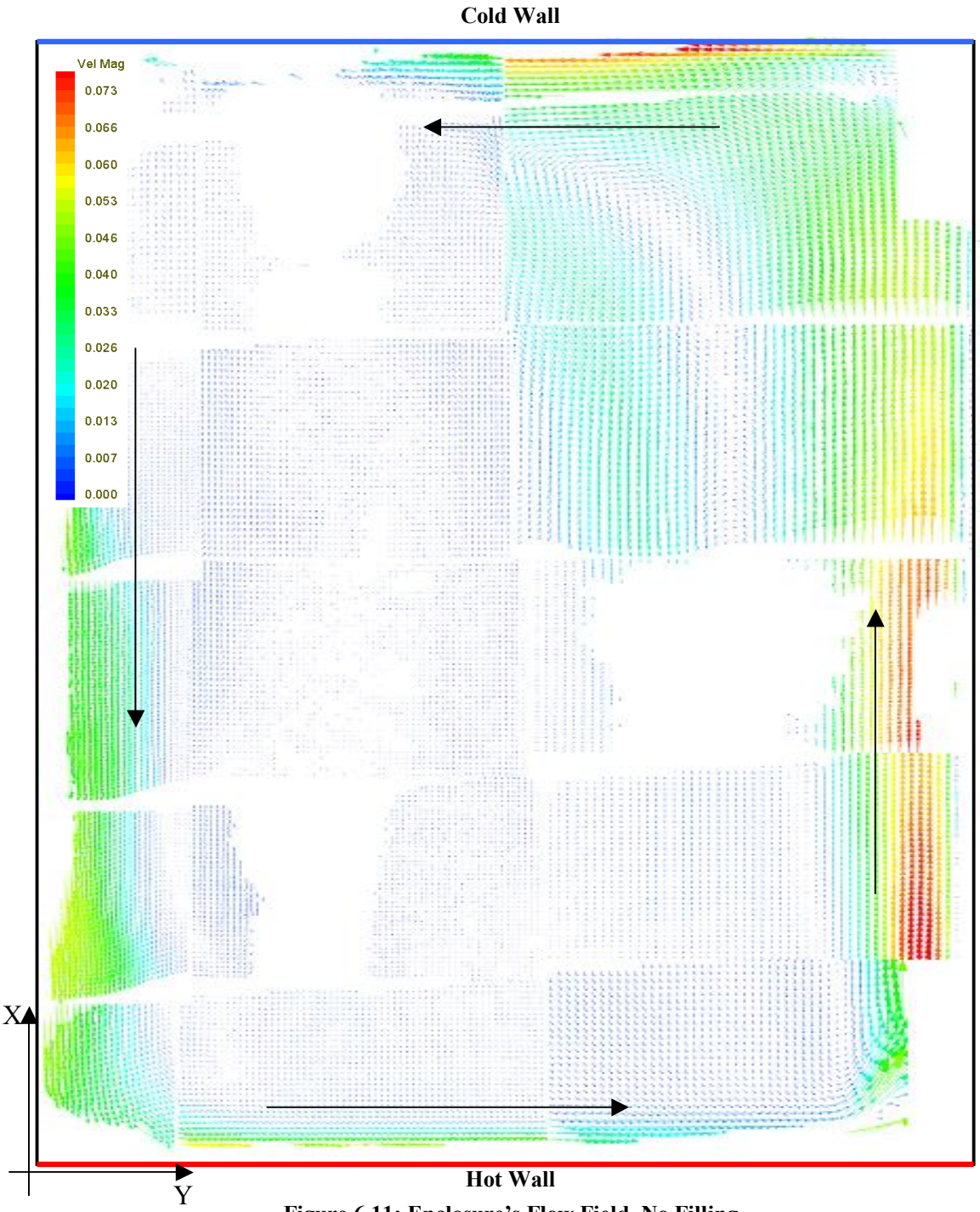

Figure 6.11: Enclosure's Flow Field, No Filling

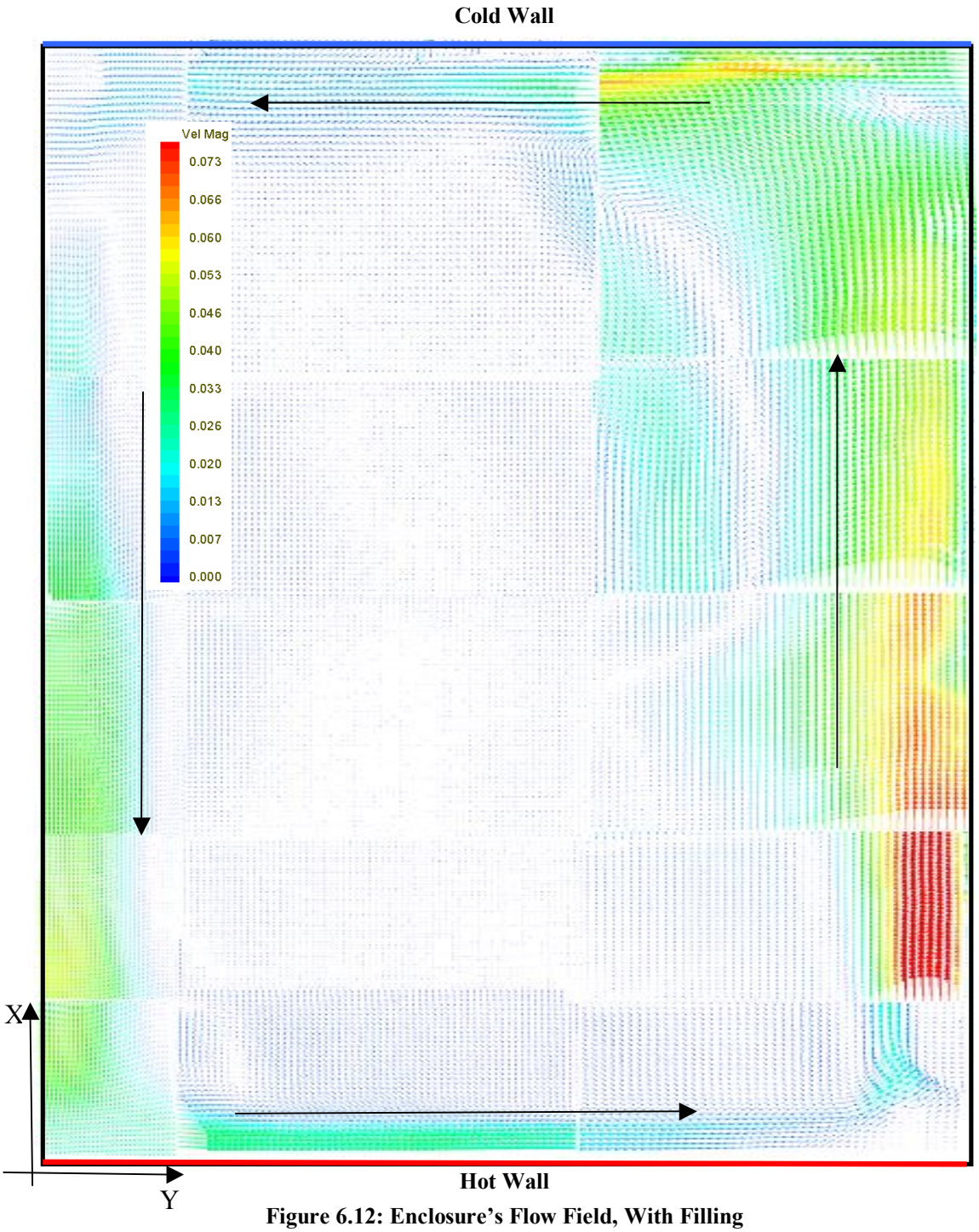

Figure 6.12: Enclosure's Flow Field, With Filling

The PIV results shown in figure 6.11 clearly show the main shape of the flow field inside the enclosure. The characteristics of the buoyant driven wall jets and the

recirculating regions at the top of the enclosure reported by Olson et al. (1990) are clearly defined.

Figure 6.13 shows the labeled velocity vectors of the flow near the corner at the top of the cold wall. Figure 6.13 shows how the flow turns from the top of the enclosure towards the cold wall. The air velocity next to the cold wall is larger than the velocity next to the top (0.075>0.045 m/s). The velocity also decreases along the top of the enclosure from hot wall to cold wall.

Figures 6.13 – 6.15 show details of the reversing loop at the top of the enclosure.

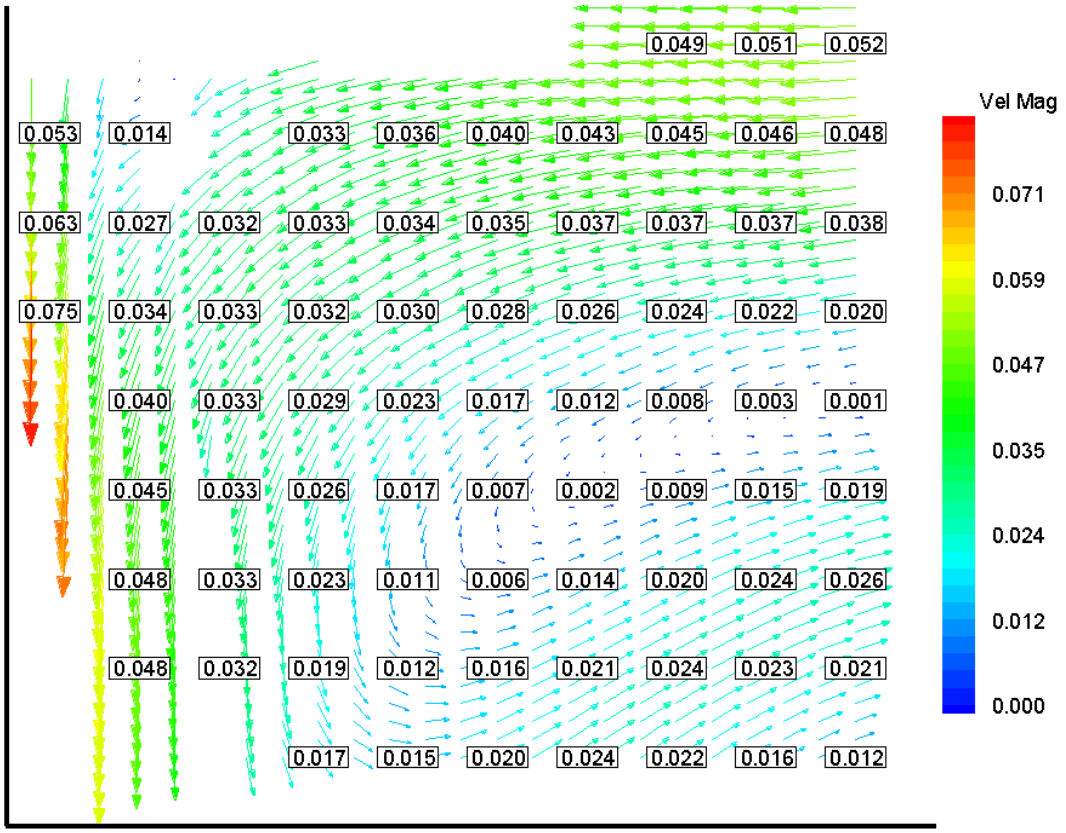

Figure 6.13: Cold-Top Corner Velocity Vectors, at 25.4 cm from Front

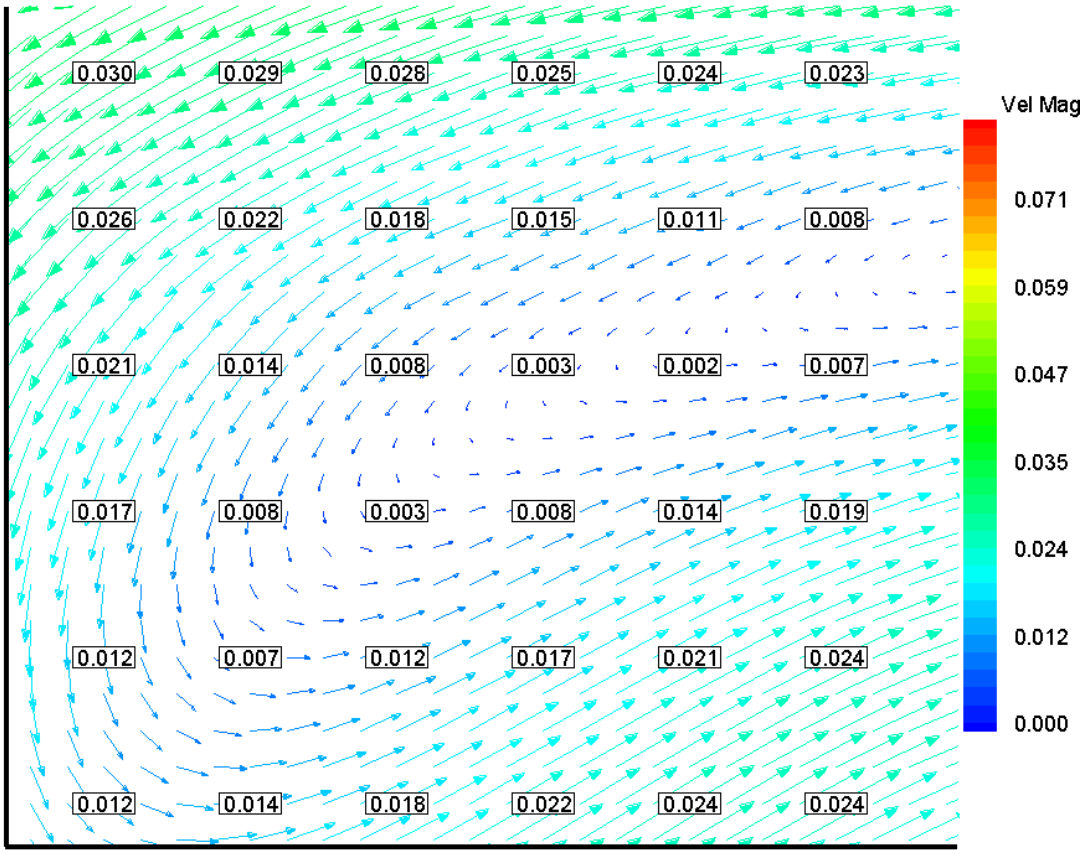

Figure 6.14: Reversing Flow Below Top Flow, at 25.4 cm from Front

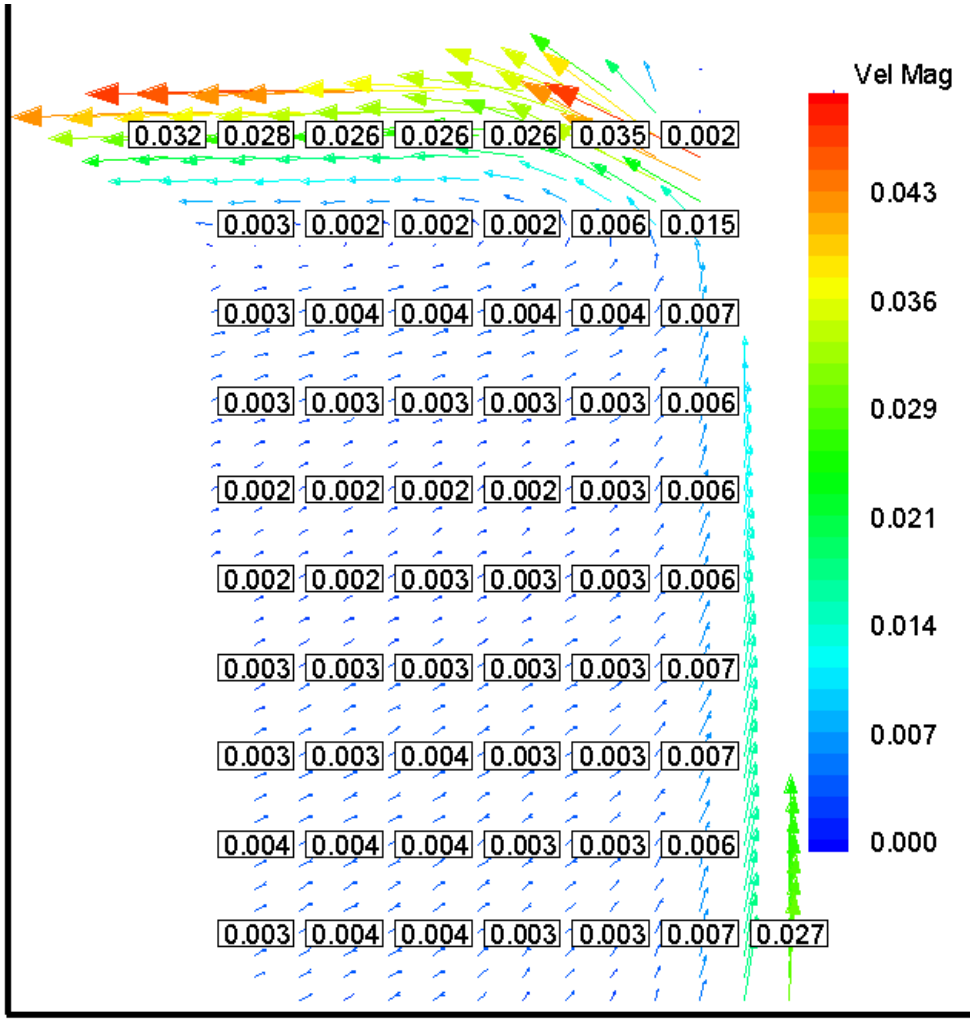

Figure 6.15: Velocity Vectors at Hot – Top Corner, at 25.4 cm from front

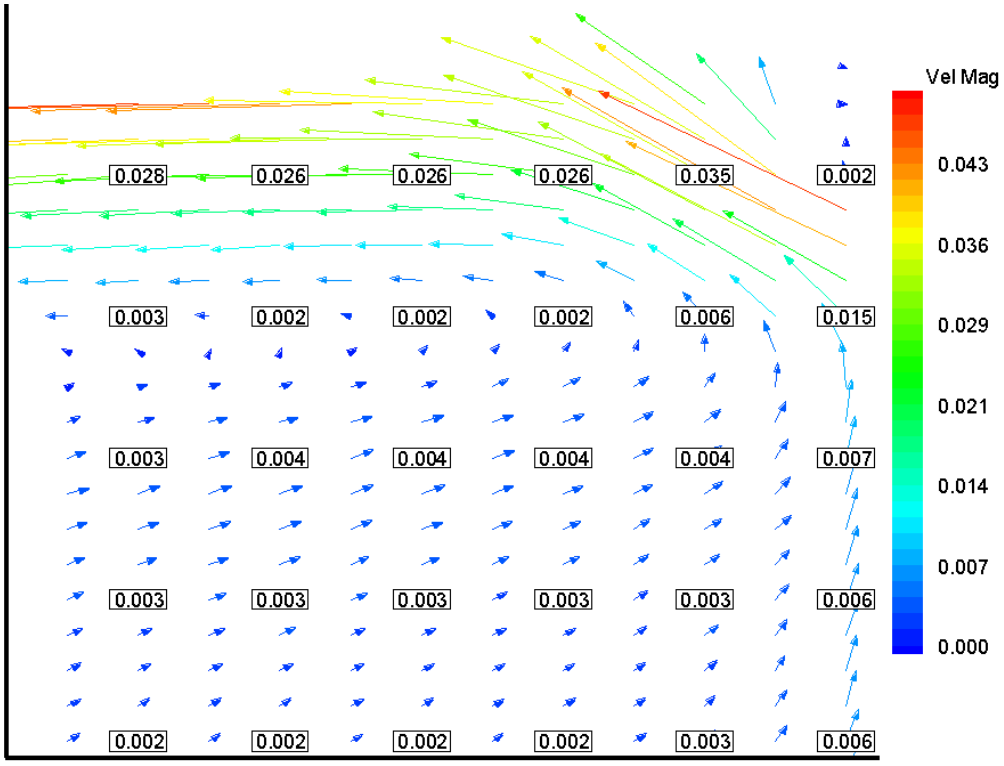

Figure 6.16: Reversing Flow at the Hot – Top Corner, at 25.4 cm from Front

The reversing loop visualized near the top agrees with the findings of Olson et al. (1990). But we were not able to visualize the other reversing loop next to the bottom; actually we were not able to resolve good velocity vectors at that region as can be seen from figure 6.11.

Nevertheless, Some of the flow PIV velocity vectors analyzed show a reversing flow near the bottom of the enclosure, but this trend is not really clear. Figure 6.17 shows the velocity vectors near the bottom, notice the velocity vectors directions and their very small magnitudes.

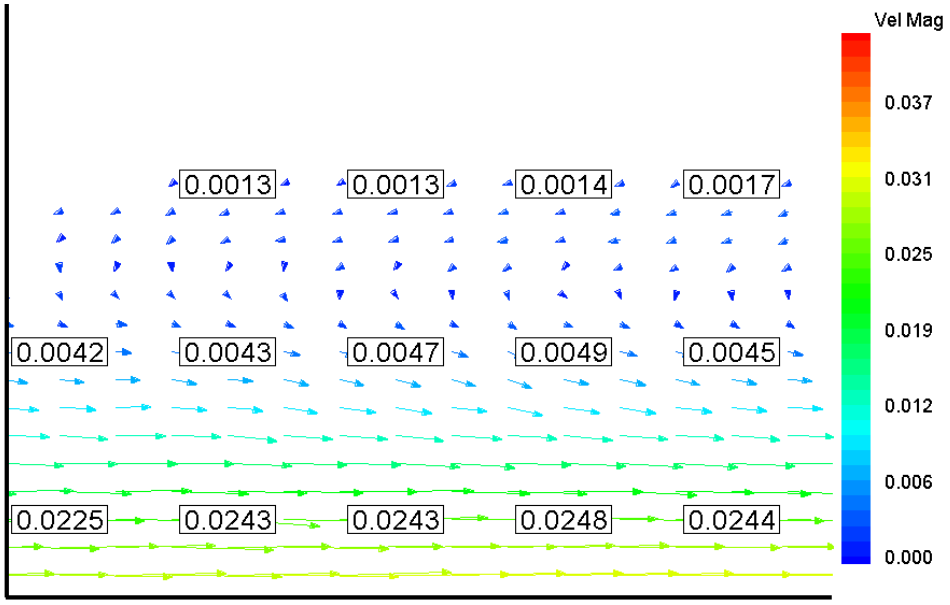

Figure 6.17: Velocity Vectors Near Enclosure Bottom, at 25.4 cm from Front

Before discussing further details of the flow field inside the enclosure, we would like to comment on the suitability of the olive oil particles as a seeding material for this flow field. The settling velocity range calculated was 0.0019 – 0.00314 m/s. The velocity range measured in this flow field is generally higher than the settling velocity of the olive oil droplets especially at the wall jets. This and the fact that the oil particles stayed in the flow field for more than 2 hrs, proves that the oil droplets are acceptable seeding particles for this flow field.

6.2.6.3 Two Dimensionality of The Flow

To further prove the two dimensionality of the flow field images were also taken at the 43.19 cm plane. The results showed excellent match with those reported for the plane at 25.4 cm from the front of the enclosure.

Figure 6.18 shows the velocity vectors of the sections 1 (at the top corner of the hot wall) shown in figure 6.7. The similarity between the shape of flow field shown in figure 6.18 and that shown in figure 6.14 is clear. Moreover, the velocity magnitudes between

the flow at both planes closely match. Also, The reversing flow beneath the primary flow is obvious in the flow shown in figure 6.18.

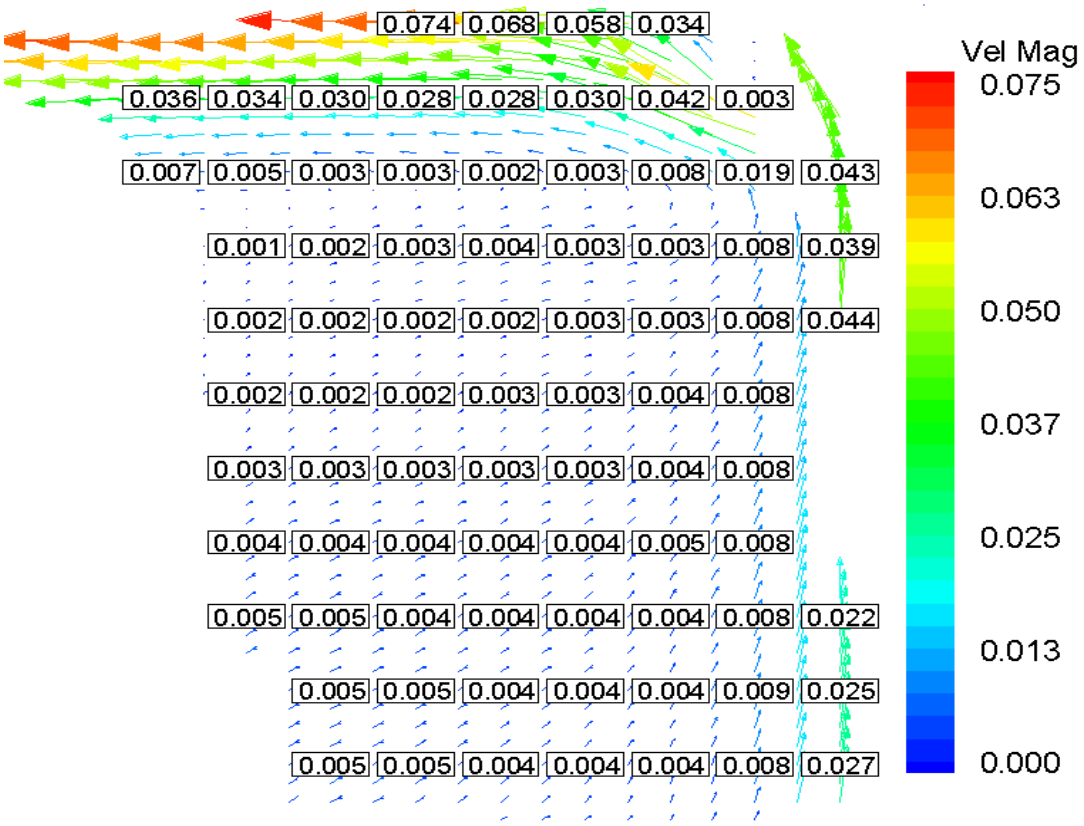

Figure 6.18: Velocity Vectors at the Hot – Top Corner, at 43.18 cm from Front

Figure 6.19 shows the labeled velocity vectors at the top corner of the cold wall 43.18 cm from the front, which is the same section as shown in figure 6.13 for the 25.4 cm plane. Excellent agreement with the results shown in figure 6.13 is seen in figure 6.19. The agreement of the general shape of the flow pattern is clear, especially the reversing loop flow. The velocity magnitudes also agree well with the results shown in figure 6.13. Thus, the PIV results confirm that the flow inside the enclosure is two dimensional.

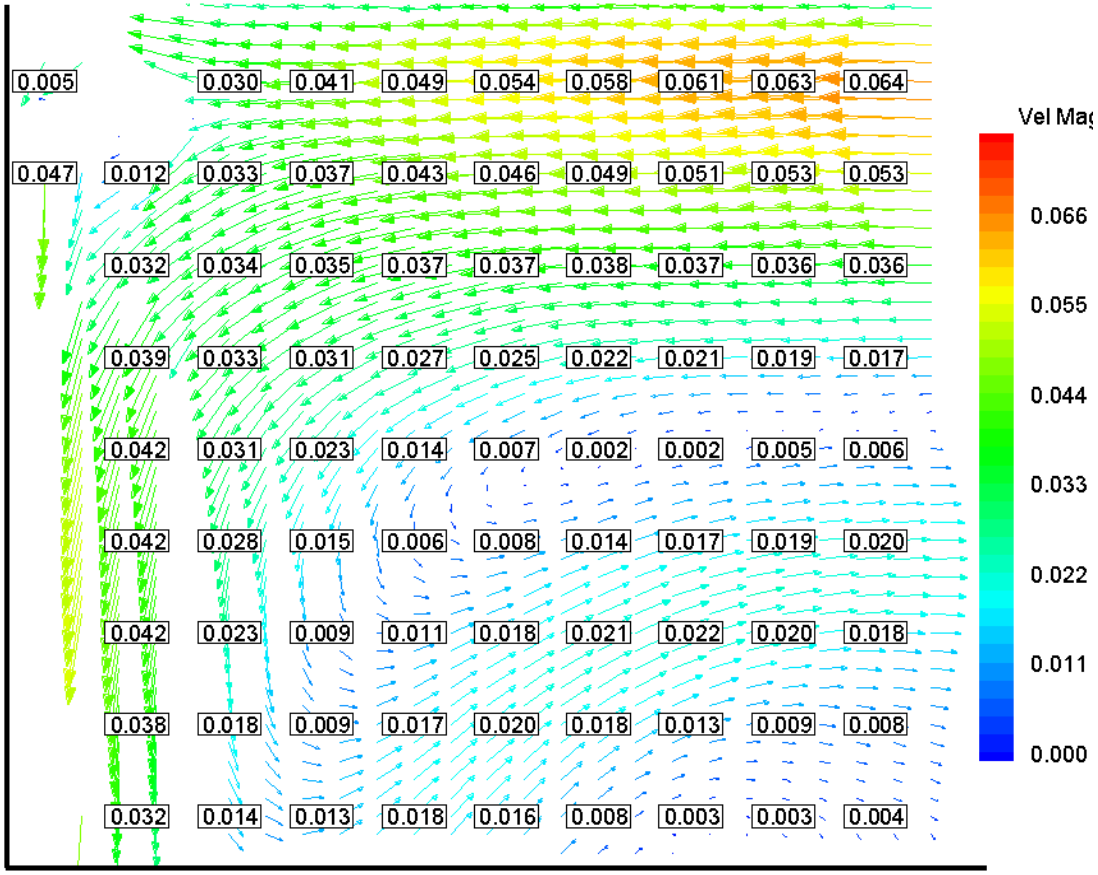

Figure 6.19: Velocity Vectors at the Cold – Top Corner, at 43.18 cm from Front

The PIV measurements conducted at the 43.18 cm plane showed a slightly more pronounced recirculating flow at the bottom flow than that at 25.4 cm. Figure 6.20 shows the reversing flow next to the bottom surface of the enclosure. The velocity of the reversing flow is very small (~0.0038 m/s).

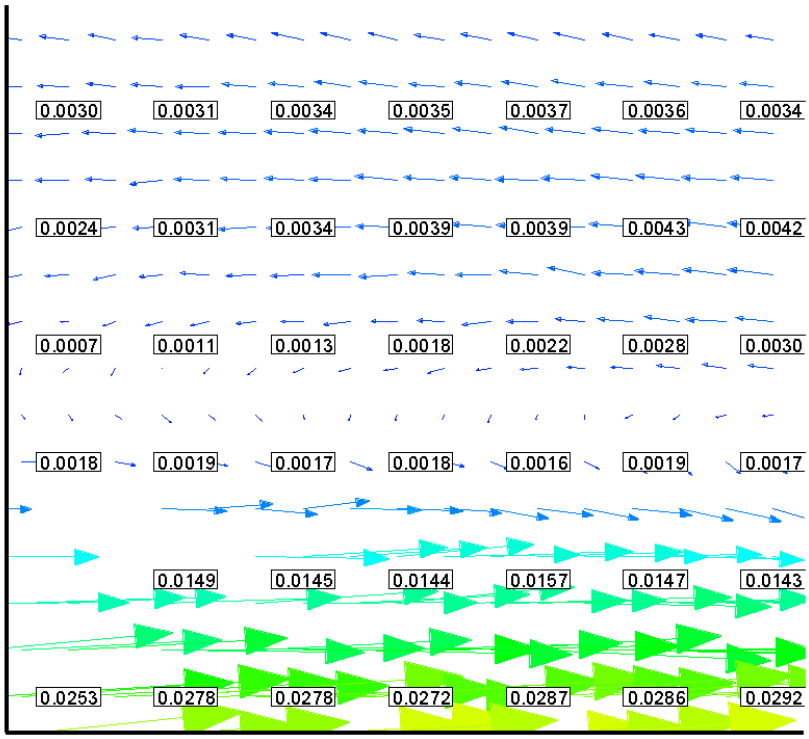

Figure 6.20: Reversing Flow Next to Bottom, at 43.18 cm from Front

6.2.6.4 Reversing Flow Structure

The two distinct flow structures (the recirculating region at the top of the enclosure and the buoyantly driven wall jets), shown in figures 6.13, 6.16 and 620, are the combined result of corner effect and buoyancy force. The corner effect was reported by Dol and Hanjalic (2001) in their numerical study. They reported that due to the temperature difference of the impinging boundary jets along the hot and cold walls notable reverse flow loops and subsequent oscillatory recovery occurred at the corners. Extending this argument to our case, and focusing on the top of the enclosure shows a warm jet that flows along the top wall. When this jet reaches the cold wall at the corner and the jet turns downward. The outer part of the jet, which did not interact with the cold wall, is still warm. This will result in buoyancy forces prevailing over viscous forces that

try to pull it down with the cold wall, and the jet will turn upward in a recirculating pattern.

Figures 6.13 and 6.14 show this action clearly. Note how the flow initially turns downward with the cold wall jet, but it then turn back towards the hot wall. Also note, how the speed of this reversing flow keeps decreasing as it flows toward the hot wall. This is caused by its interaction with the core and the top jet, see figures 6.15 and 6.16 and note the velocity difference with figures 6.13 and 6.14.

The bottom reversing loop, on the other hand, is not so clear as reported by Olson et al. (1990). This is due to the fact that we were running at a different Ra ($\sim 10^8$) than what they reported ($\sim 10^{10}$). Also, the heat losses to the atmosphere could have played a role in damping the reversing loop next to the bottom, since heat is lost from the core, which made it at a temperature closer to the bottom jet and thus reduced the buoyancy forces required to develop such a reversing loop.

Thus, the top reversing loop might have been strengthened by the enclosure losses, which increase the effect of the buoyancy forces that create it. It would be interesting to check the shape of the flow with the walls insulation in place. This might be possible with a guard space on a slot in the insulation for the laser sheet.

6.2.7 Conclusions

In this section successful PIV measurements were conducted for the flow field inside the experimental facility. Olive oil droplets of size 1 – 3 μm, generated by a six nozzle atomizer, were a suitable seeding material for the flow. The seeding particles had a long settling time (~ 2 – 3 hrs), which was enough for taking good pictures of the flow field. Images were recorded, processed, validated and averaged for each section in the flow.

The flow field recorded for the enclosure showed the major flow structure including circulating flow, a stagnant core, a strong reversing loop along the top wall and a weak reversing loop along the bottom wall.

The flow field inside the experimental facility was two dimensional, which agrees with the results obtained from the temperature profile of the enclosure and smoke visualization.

7. Summary of Results and Future Work

7.1 Summary of Results

In this project an experimental facility was built, and instrumented to measure the building heat transfer and airflow. Heat transfer and flow visualization were conducted using the experimental facility with air as the working fluid. The results agreed well with previously reported results.

Heat transfer experiments were conducted under steady state conditions with air as the working fluid. The range of Grashof number tested was ($Gr^* = 1.24x10^8 – 1.87x10^8$). The results obtained from the experimental facility were compared with the literature and showed acceptable agreement. The temperature profile inside the experimental facility was two dimensional with a linearly stratified core.

Smoke visualization of the flow field inside the enclosure was conducted at Grashof number ($Gr^* = 2.71x10^8$). The flow field observed was two dimensional with a stationary core. The boundary layer of the flow next to the isothermal walls appeared to be turbulent.

PIV measurements of the flow field inside the experimental facility were conducted at $Gr^*=2.71x10^8$. Olive oil droplets (~ 1 – 3 μm) were successfully used as the seeding particles. Detailed and precise measurements of the flow field inside the enclosure were obtained. PIV results further proved the two dimensionality of the flow field. Velocity measurements were obtained using PIV. Thin buoyantly driven jet was observed next to

the isothermal walls of the facility, while a recirculating region was observed next to the top and bottom.

The success of the PIV technique presented here demonstrates the feasibility of the technique for natural convection velocity field measurements. Although, the heat balance was not maintained during flow visualization using this technique, the surface temperature dropped on both sides by 2 ^{o}C, and thus the Grashof number stayed at the same order. This indicates a similar flow pattern inside the enclosure before and after the insulation was removed.

The seeding particles used for this experiment were acceptable for PIV measurements. The olive oil droplets closely followed the flow pattern inside the enclosure, and stayed suspended in the enclosure for over two hours--long enough for the flow field to reconstruct and allow PIV measurements. The settling velocity of the particles was calculated as 0.0019 – 0.003 m/s.

7.2 Recommendations and Future Work

This work can be further improved to gain more accurate results and cover a wider range of flow patterns. The author suggests the following to improve the performance of the facility:

- Higher density gases should be used to get a wider range of Grashof number and still show the effect of the internal radiation exchange. A suggested scaling fluid was R124.
- The seeding technique could be further improved by modifying the system to deliver the olive oil mist at lower pressures. A mixing tank and pressure

regulator between the atomizer and the enclosure could be used to achieve low pressure delivery of the seeding particles.

- Different seeding material should be explored for PIV measurements. Although olive oil droplets proved to be a good seeding material, an atomizer is required to produce the oil droplets. Solid particles such as wheat flour or talcum powder might be feasible and could be introduced with little disturbance to the flow field.
- The cooling panel should be redesigned to increase the heat transfer rate and reduce the surface temperature non-uniformity. The temperature difference across the cooling panel should be increased, by adding more passes for example. Then, the temperature difference can be measured using a differential thermocouple, which will reduce the experimental uncertainty of the measurement.
- Improve the spatial precision of the air temperature measurement and automate control of the traversing mechanism.
- Redesign the hot and cold walls as an integral part of the enclosure; this will reduce the time required for reaching steady state conditions.
- Redesign the enclosure insulation so that a minimum amount of insulation is removed whenever PIV measurement is required.

References

Adrain, R. J. (1997). "Dynamic Ranges of Velocity and Spatial Resolution of Particle Image Velocimetry." Measurement Science Technology **8**: 1393-1398.

Adrian, R. J. (1991). " Particle Imaging Techniques for Experimental Fluid Mechanics." Annual Review Fluid Mechanics **23**: 261-304.

Ampofo, F., and Karayiannis, T. G. (2003) "Experimentald benchmark data for turbulent natural convection in an air filled square cavity." International Journal of Heat and Mass Transfer **46** (19): 3551-3572.

Awbi, H. B., and Hatton, A. (1999). "Natural Convection from Heated Room Surfaces." Energy and Buildings **30** (3): 233-244.

Bejan, A. (1995). "Convection Heat Transfer." NY, USA, John Wiley & Sons, Inc.

Bejan, A., Al-Humoud, A., and Imberger, J. (1981). "Experimental Study of High Rayleigh Number Convection in a Horizontal Cavity with Different end Temperatures." Journal of Fluid Mechanics **109**: 283-299.

Bohn, M. S., and Anderson, R. (1986). "Temperature and Heat Flux Distribution in a Natural Convection Enclosure Flow. " Journal of Heat Transfer, Transactions ASME 108 (2):471-475.

Cheesewright, R., and Zial, S. (1986). "Distributions of Temperature and Local Heat Transfer Rate in Turbulent Natural Convection in a Large Rectangular Cavity. " The 8th International Heat Transfer Conference.

Chen, C. C., and Eichhorn, R. (1976). "Natural Convection From a Vertical Surface to a Thermally Stratified Fluid." Journal of Heat Transfer, Transactions ASME **98, Ser. C**: 446-451.

Dol, H. S., and Hanjalic, K. (2001). "Computational study of turbulent natural convection in a side-heated near-cubic enclosure at a high Rayleigh number." International Journal of Heat and Mass Transfer **44** (12): 2323-2344.

Gui, L., and Merzkirch, W. (2000). "A Comparative Study of The MQD Method and Several Correlation Based PIV Evaluation Algorithms." Experiments in Fluids **28**: 26-44.

Gui, L., Longo, J., and Stern, F. (2001). " Biases of PIV Measurement of Trubulent Flow and The Masker Correlation Based Interrogation Algorithm." Experiments in Fluids **30**: 27-35.

Ferm, H. M. (1985). "Measurements and Analysis of Natural Convection in Building Enclosures. " Mechanical Engineering, Massachusetts Institute of Technology. S. M. Thesis.

Hsieh, S. S., and Wang, C. Y. (1994). " Experimental Study of Three Dimensional Natural Convection in Enclosures with Different Working Fluids." International Journal of Heat Transfer **37**(17): 2687-2698.

Huang, H., Daribi, D., and Gharib M. (1997). "On Errors of Digital Particle Image Velocimetry." Measurement Science and Technology **8**: 1427-1440.

TSI Inc. (**2003**). Particle Image Velocimetry System: Installation Manual.

TSI Inc. (**2003**). "Particle Image Velocimetry System: Operations Manual."

Incropera, F. P., and DeWitt, D. P. (1996). "Fundamentals of Heat and Mass Transfer." NY, USA, John Wiley & Sons, Inc.

Keane, R. D., and Adrian, R. J. (1990a). "Optimization of Particle Image Velocimeters." Proceedings of SPIE-the International Society for Optical Engineering.

Keane, R. D., and. Adrian, R. J. (1990b). "Optimization of Particle Image Velocimeters. Part I: Double Pulsed Systems." Measurements Science Technology **1**: 1202-1215.

Keane, R. D., and. Adrian, R. J. (1991). "Optimization of Particle Image Velocimeters. Part II: Multiple Pulsed Systems." Measurements Science Technology **2**: 963-974.

Khalifa, A. J. N., and Marshal, R. H. (1990). "Validation of Heat Transfer Coefficients on Interior Building Surfaces Using a Real Sized Indoor Test Cell." International Journal of Heat Transfer **33**: 2219-2236.

Kim, K. S. (1996). "Numerical Analysis of Turbulent Natural Convection Coupled with Radiation." ASME, Fluid Engineeign Division (Publications) **237**: 705-717.

Kline, S. J., and Mclintock, F.A. (1953). "Describing Uncertainties in Single-Sample Experiments." Mechanical Engineering **57** (1): 62-6.

Meares, A. J., Holdϕ, A. E., and Wakes, S. J. (1997). "A Novel Seeding Technique for The Flow Visualization of Pressurized Air Flows." Measurement Science and Technology **8**: 1183-1186.

Melling, A. (1997). "Tracer Particles and Seeding for Particle Image Velocimetry." Measurement Science and Technology **8**: 1406-1416.

Olson, D. A. (1986). "Scale Model Studies of Natural Convection in Enclosures at High Rayleigh Number. " Mechanical Engineering, Massachusetts Institute of Technology. PhD Thesis.

Olson, D. A., Glicksman, L. R., and Ferm, H. M. (1990). "Steady-State Natural Convection in Empty and Partitioned Enclosures at High Rayleigh Numbers." Journal of Heat Transfer, Transactions ASME **112**: 640-647.

Raffel, M., Willert, C., and Komenhans, J. (1998). "Particle Image Velocimetry: a Practical Guide." Berlin, Germany. Springer-Velarg.

Said, A. A. M., Habilb, M. A., and Khan, M. A. R. (1997). "Turbulent Convection Flow in Partitioned Enclosure. " Computers and Fluids **26** (6): 547-563.

Velusamy, K., Sundararajan, T., and Seetharamu, K. N. (2001). "Interaction Effects Between Surface Radiation and Turbulent Natural Convection in Square and Rectangular Enclosures." Journal of Heat Transfer, Transactions ASME **123**: 1062-1070.

Weber, D. D., and Kearney, R. J. (1980). "Natural Convective Heat Transfer Through an Aperture in Passive Solar Heated Buildings." Proceedings of the 5th National Passive Solar Conference. **2**: 1037-1041. Amherst, Mass.

Westerweel, J. (1997). "Fundamental of Digital Particle Image Velocimetry." Measurement Science and Technology **8**: 1379-1392.

Appendix: Equipments and Components

Figure A.1: Ohio Semitronics Inc. Watt Transducer: model AWG001

Figure A.2: Data Logging System: Fluke-NetDaq

Figure A.3: Data Logging System: Fluke-Hydra Data Logging System

Figure A.4: PIV Laser Arm: TSI Inc. model 610015

Figure A.5: PIV Laser Source: New Wave model Gemini 200

Vita

Mohammad Elyyan

Candidate for the Degree of

Master of Science

Thesis: DESIGN OF AN EXPERIMENTAL FACILITY FOR BUILDING AIRFLOW AND HEAT TRANSFER MEASUREMETNS

Major Field: Mechanical Engineering

Biographical:

Personal Data: Born in Amman, Jordan on January 1, 1979, the son of Ahmad and Fatima Elyyan.

Education: Graduated from Al - Hussein College High School, Amman, Jordan in June 1996. Received a Bachelor of Science degree in Mechanical Engineering from Jordan University of Science and Technology, Irbid, Jordan in February 2001. Completed the requirements for the Master of Science degree with a major in Mechanical Engineering at Oklahoma State University in May 2005.

Experience: Employed by JUST, Department of Mechanical Engineering, as a lab supervisor from August 2000 to January 2001. Employed by Jordan Engineering Society (JES) from April 2001 to June 2002. Employed by Oklahoma State University, Department of Mechanical and Aerospace Engineering as a Teaching Assistant and Research Engineering from August 2002 to present.

Professional Memberships: Jordan Engineers Association, Phi Kappa Phi Honor Society, and American Society of Heating, Refrigeration and Air-Conditioning Engineers.

Name: Mohammad Ahmad Elyyan Date of Degree: May, 2005

Institution: Oklahoma State University Location: Stillwater, Oklahoma

Title of Study: DESIGN OF AN EXPERIMENTAL FACILITY FOR BUILDING AIRFLOW AND HEAT TRANSFER MEASUREMENTS

Pages in Study: 122 Candidate for the Degree of Master of Science

Major Field: Mechanical Engineering

Scope and Method of Study: An experimental facility was constructed and instrumented to conduct heat transfer experiments and flow visualization. The experimental facility is a 1/5-scale model of a full-scale two story building with aspect ratio (H/L) of 0.625. Natural convection experiments were conducted with hot and cold end walls with the rest of the enclosure insulated. Air was the working medium inside the experimental facility. The Grashof number of the flow was ~ 10^8. Smoke flow visualization and PIV were conducted for the flow field inside the experimental facility.

Findings and Conclusions: The heat transfer results obtained agreed fine with the results reported in the literature. The smoke visualization and PIV techniques showed the existence of thin boundary layer next to the isothermal walls and stationary core inside the enclosure. The seeding particles used for PIV were olive oil droplets. The flow was two dimensional as proved by the temperature measurement; smoke visualization, and PIV results. PIV showed the existence of reversing loops next to the top and bottom of the enclosure. The PIV technique worked well with natural convection flow. Olive oil droplets of 1 – 3 μm successfully seeded the flow field, and had a sufficiently long settling time to allow reconstruction of the buoyantly driven flow field prior to image capturing.

ADVISOR'S APPROVAL: **Dr. Daniel Fisher**